ESA STUDY CONTRACT REPORT

No ESA Study Contract Report will be accepted unless this sheet is inserted at the beginning of each volume of the Report.

ESA CONTRACT NO: 9063/90/HGE-I	SUBJECT: PREPARATION FOR THE USE OF DÖPPLER WIND LIDAR INFORMATION IN METEOROLOGICAL DATA ASSIMILATION SYSTEMS	NAME OF CONTRACTOR UK METEOROLOGICAL OFFICE

* ESA CR( ) No:	* STAR CODE	No. of Volumes 1 This is Volume No: 1	CONTRACTOR'S REFERENCE:

ABSTRACT:

The use of data from future Döppler wind lidar (DWL) instruments is addressed under three main headings; assimilation and quality control; data representativeness errors; case studies of data utility. Recommendations on the production of simulated DWL observations for further studies are given.

It is shown that data assimilation systems can use single-component winds derived from a single lidar shot. Consequently, shot-pair processing to obtain wind vectors is unnecessary for purposes of model assimilation.

Methods for extracting information from data with a high probability of gross error (expected when the signal-to-noise ratio is low) are described and tested. Consensus averaging is shown to be an effective method of quality control for small groups of data with similar line-of-sight. Data which are distributed in space may be treated using nonlinear variational analysis, and results from a two-dimensional scheme are presented. The scheme may be used either to detect observations with gross errors, prior to a conventional (linear) analysis step, or to produce the analysis directly. The latter, direct, method was shown to be more accurate.

The average error implicit in taking single-shot data (which sample a small volume of space) as representative of conditions over a 100km grid box is estimated (using spectral analysis of wind data) to be 2-3ms^{-1}. Local enhancements to this background value are considered for a variety of meteorological phenomena.

Simulation studies aimed at evaluating different scanning and instrumental configurations are presented. For data assimilation, a scanning instrument is to be preferred to a 4-fixed-beam instrument, if other instrument characteristics are equal.

Case studies addressing the effect of cloud obscuration on utility for numerical weather prediction and climate studies suggest that; a) the impact of DWL winds in improving forecasts of cyclogenesis may not be seriously hampered by cloud obscuration; b) cloud obscuration will bias the distribution of lidar data towards regions of equatorward moisture flux, especially in mid-latitudes by obscuring intense fluxes in frontal "warm conveyor belts". Consequently, it will be better to use assimilated analyses for climatological studies of moisture fluxes, rather than using the DWL data directly.

Names of authors:

A.C.Lorenc, R.J.Graham, I.Dharssi, B.Macpherson, N.B.Ingleby, R.W.Lunnon

** NAME OF ESA STUDY MANAGER E. ORIOL-PIBERNAT DIV: OEE DIRECTORATE OEE	** ESA BUDGET HEADING 60.512	

* Sections to be completed by ESA

** Information to be provided by ESA Study Manager

FINAL REPORT ON ESA STUDY CONTRACT 9063/90/HGE-I:

"PREPARATION FOR THE USE OF DOPPLER WIND LIDAR INFORMATION IN METEOROLOGICAL ASSIMILATION SYSTEMS"

A.C.Lorenc, R.J.Graham, I.Dharssi, B.Macpherson,
N.B.Ingleby, R.W.Lunnon

Short-range Forecasting Research
Meteorological Office
Bracknell
U.K.

February 1992

ESA Technical management: E.Oriol-Pibernat

ESA contract No. 9063/90/HGE-I
S-Div. Sci. Paper No. 2

Abstract

The use of data from future Döppler wind lidar (DWL) instruments is addressed under three main headings; assimilation and quality control; data representativeness errors; case studies of data utility. Recommendations on the production of simulated DWL observations for further studies are given.

It is shown that data assimilation systems can use single-component winds derived from a single lidar shot. Consequently, shot-pair processing to obtain wind vectors is unnecessary for purposes of model assimilation.

Methods for extracting information from data with a high probability of gross error (expected when the signal-to-noise ratio is low) are described and tested. Consensus averaging is shown to be an effective method of quality control for small groups of data with similar line-of-sight. Data which are distributed in space may be treated using nonlinear variational analysis, and results from a two-dimensional scheme are presented. The scheme may be used either to detect observations with gross errors, prior to a conventional (linear) analysis step, or to produce the analysis directly. The latter, direct, method was shown to be more accurate.

The average error implicit in taking single-shot data (which sample a small volume of space) as representative of conditions over a 100km grid box is estimated (using spectral analysis of wind data) to be 2-3ms^{-1}. Local enhancements to this background value are considered for a variety of meteorological phenomena.

Simulation studies aimed at evaluating different scanning and instrumental configurations are presented. For data assimilation, a scanning instrument is to be preferred to a 4-fixed-beam instrument, if other instrument characteristics are equal.

Case studies addressing the effect of cloud obscuration on utility for numerical weather prediction and climate studies suggest that; a) the impact of DWL winds in improving forecasts of cyclogenesis may not be seriously hampered by cloud obscuration; b) cloud obscuration will bias the distribution of lidar data towards regions of equatorward moisture flux, especially in mid-latitudes by obscuring intense fluxes in frontal "warm conveyor belts". Consequently, it will be better to use assimilated analyses for climatological studies of moisture fluxes, rather than using the DWL data directly.

Contents

1 Introduction

The deployment of a satellite borne Döppler wind lidar instrument could provide observations of the 3-D wind field at high resolution on the global scale. Such observations would represent a valuable data base for improving our understanding of atmospheric processes - leading to better models for weather and climate prediction. Global wind data coverage could also bring improvements in initial conditions for numerical weather prediction (NWP) models. The indirect relationships between remotely sensed data and the model variables which are to be determined often give rise to errors and limitations which make the data less useful than first expected. Döppler wind lidar observations suffer less than some others in this way, however they have several potentially limiting features: only a single component of the vector wind is observed, poor signal-to-noise ratio in clean air may lead to a significant proportion of bad data, and the measured velocity is the line-of-sight velocity of a small volume of air rather than the horizontal velocity average for a grid box. The purpose of this study is to investigate the feasibility, given the above errors and limitations, of using Döppler lidar data in NWP analysis and to examine the best techniques for assimilating the data. In addition, some of the characteristic errors are evaluated and presented in a form suitable for simulating lidar wind data in future observation system simulation experiments (OSSEs). The relative benefits of different scanning and instrumental options and general questions of the utility of the lidar data for NWP and climate studies are also addressed.

Sections 2 3 and 4 are concerned with techniques for assimilating the data into NWP models, and it is shown that the errors and limitations referred to above are not serious problems. In section 2 we show that single-component winds can be used directly in current and future analysis systems; there is no need to arrange for coincident shots or observation preprocessing to give vector winds. In section 3 we show that theoretically well-founded techniques exist to cope with a large proportion of erroneous data, either in a preprocessing "quality control" step, or in a nonlinear variational analysis that combines quality control with a direct analysis of single component winds. By using all available information, the nonlinear scheme gives better results than schemes which do a preliminary quality control on limited information. In section 4 we study the errors of representativeness associated with the poor sampling; they turn out to be not very different from those associated with current radiosonde observations.

The utility of the lidar data for different purposes will depend to some extent on the chosen scanning and instrumental configuration. In section 5 we show that for NWP purposes a scanning configuration will be preferable to a fixed beam configuration. The impact of cloud obscuration on the benefits of lidar data for NWP purposes and for climate studies is investigated using case study examples in section 6. A summary of results and recommendations for future OSSEs is given in section 7.

This work, and a parallel study by Courtier *et.al.* (ESA contract study 8850/90/HGE-I, 1992) are within the framework of studies A1, A3 and A4 recommended by the ALADIN report (ESA SP-1112, 1989). The two studies have been performed in close cooperation and are designed to be complementary.

2 Feasibility of Assimilating Single Component Winds

Most existing operational meteorological analysis schemes expect wind data to be presented as vectors, or as u and v components in some predefined coordinates. Thus in some studies of the instrument it was assumed this was a requirement. Such a requirement is a severe constraint on the design of the instrument or preprocessing system. The lidar provides only a line-of-sight component, and the provision of coincident shots from different directions requires careful alignment of observations forwards and backwards as the satellite moves along its orbit. If this alignment is not achieved, then the required interpolation of non-coincident single component winds would introduce an averaging, which would cut the potential resolution of the data, and cause erroneous data to corrupt several derived vectors. So in this section we provide a clear demonstration that the single component winds can be used directly in practical assimilation systems. Only horizontal winds are considered here; the effect of the vertical components is considered in section 4. Below we give examples using Optimal Interpolation (OI), the most commonly used analysis method, and another full operational scheme. At the end of section 3 we give an example using a variational scheme; such schemes are the subject of much current research.

2.1 Optimal Interpolation

OI forms the basis of the assimilation schemes at most major operational numerical prediction centres in the world. It combines information from a background field with the observations so as to minimize the expected analysis error variance. We use as an example a two-dimensional OI scheme derived from Lorenc (1981). The analysis with the minimum expected error variance is found from a system of linear equations, involving error covariances between the observed parameters, and between the observed and analysis parameters. Observational errors are assumed to be independent, so that covariances between different observations are zero. Background error covariances are modelled by a continuous function. Making the assumption that the background wind errors are non-divergent and isotropic, all the required covariances can be derived from that for streamfunction ψ. For the u and v components usually used to represent wind we have

$$\langle \varepsilon_i^u \varepsilon_j^u \rangle = \frac{\partial^2 \langle \varepsilon_i^\psi \varepsilon_j^\psi \rangle}{\partial y_i \partial y_j} \qquad \langle \varepsilon_i^v \varepsilon_j^u \rangle = - \frac{\partial^2 \langle \varepsilon_i^\psi \varepsilon_j^\psi \rangle}{\partial x_i \partial y_j}$$

$$\langle \varepsilon_i^u \varepsilon_j^v \rangle = - \frac{\partial^2 \langle \varepsilon_i^\psi \varepsilon_j^\psi \rangle}{\partial y_i \partial x_j} \qquad \langle \varepsilon_i^v \varepsilon_j^v \rangle = \frac{\partial^2 \langle \varepsilon_i^\psi \varepsilon_j^\psi \rangle}{\partial x_i \partial x_j} \tag{2.1}$$

Here <·> represents an expected value over many realizations, and ε is the difference between the background value of a parameter (indicated by the superscript) and a perfect "true" value. We assume that the background is unbiased, so these terms are covariances. Introducing vector notation $\mathbf{V}_i$ for $(u_i, v_i)^T$, the four term in (2.1) make up the covariance tensor $\langle \mathbf{V}_i \mathbf{V}_j^T \rangle$. Now a wind component $w_i(\vartheta_i)$ in any arbitrary direction ϑ_i at point i is given by the scalar product $\mathbf{n}_i^T \mathbf{V}_i$, where $\mathbf{n}_i$ is the unit vector $(\cos\vartheta_i, \sin\vartheta_i)^T$. To use the OI equations directly on single-component winds we need covariances between these arbitrarily directioned components:

$$\langle w_i(\vartheta_i)\, w_j(\vartheta_j) \rangle = \langle (\mathbf{n}_i^T \mathbf{V}_i)\, (\mathbf{n}_j^T \mathbf{V}_j)^T \rangle$$

$$= \mathbf{n}_i^T \langle \mathbf{V}_i\ \mathbf{V}_j^T \rangle\, \mathbf{n}_j . \tag{2.2}$$

$$= (\cos\vartheta_i, \sin\vartheta_i) \begin{pmatrix} \dfrac{\partial^2 \langle \varepsilon_i^\psi \varepsilon_j^\psi \rangle}{\partial y_i \partial y_j} & - \dfrac{\partial^2 \langle \varepsilon_i^\psi \varepsilon_j^\psi \rangle}{\partial x_i \partial y_j} \\ - \dfrac{\partial^2 \langle \varepsilon_i^\psi \varepsilon_j^\psi \rangle}{\partial y_i \partial x_j} & \dfrac{\partial^2 \langle \varepsilon_i^\psi \varepsilon_j^\psi \rangle}{\partial x_i \partial x_j} \end{pmatrix} \begin{pmatrix} \cos\vartheta_j \\ \sin\vartheta_j \end{pmatrix}$$

Lorenc (1981) shows how this covariance model can be extended to a sphere, and to geostrophically consistent covariances with the mass field. It can also be extended to divergent winds by using also a covariance function for the velocity potential.

Traditionally in OI the discrete representation of the background field (e.g. at a grid of points) is not explicitly expressed in the equations; background values at the observation positions and covariances of their errors are represented by a vector **b** and matrix **B**. The elements of **B** are evaluated using (2.2). Covariances are also needed between observation and grid point positions, and background and analysis values are needed in the grid-point representation. We use the same symbols for these; to avoid confusion we put suffices i and j for observations and k and l for grid-points. Observational and representativeness errors are assumed to be uncorrelated, and are represented by diagonal matrices $\mathbf{O}_{ij}$ and $\mathbf{F}_{ij}$. The OI analysis equation is:

$$\mathbf{u}_k = \mathbf{b}_k + \mathbf{B}^T_{ik} \, (\mathbf{B}+\mathbf{O}+\mathbf{F})^{-1}_{ij} \, (\mathbf{o}_i - \mathbf{b}_i), \tag{2.3}$$

where $\mathbf{u}_k$ is the vector of analysis values, and $\mathbf{o}_i$ is the vector of observed values.

An advantage of the OI analysis method is that the expected error variance of the analysis can be calculated; use is made of this in section 5. The full analysis error covariance is given by

$$\mathbf{A}_{kl} = \mathbf{B}_{kl} - \mathbf{B}^T_{ik} \, (\mathbf{B}+\mathbf{O}+\mathbf{F})^{-1}_{ij} \, \mathbf{B}_{jl}, \tag{2.4}$$

only the diagonal of this need be calculated to provide estimated error variances.

Two examples using this system are given here; further examples can be seen in section 5, where it is used to evaluate instrument scan scenarios.

Example 1

Observations were generated in a pattern simulating a lidar scan, in circles of radius 1000km, with centres every 100km. Lidar winds were obtained by interpolating the appropriate component of an assumed "true wind field", adding Gaussian errors with a standard deviation of $2.5\mathrm{ms}^{-1}$. We put 40 observations per scan, making the average separation between adjacent observations of the single component of the wind about 70km. 452 single-component observations were used, in a single matrix calculation, to evaluate the analysis at all grid points within a box using (2.3).

The streamfunction covariance is assumed to be isotropic and homogeneous, and the traditional assumption is that it has a Gaussian shape, i.e.

$$\langle \varepsilon^{\psi}_i \varepsilon^{\psi}_j \rangle = E^2_{\psi} \exp(-r_{ij}^{\;2}/2L^2) \tag{2.5}$$

where

$$r_{ij}^{\;2} = (x_j - x_i)^2 + (y_j - y_i)^2. \tag{2.6}$$

We put L=500km and chose E_{ψ} such that E_v, the standard deviation of the background wind velocity components, was $5\mathrm{ms}^{-1}$. A background field was generated by adding errors with this covariance structure to the "true wind field". OI was then used to generate an analysed field, which when compared with the "truth" had root mean square (r.m.s) error of $0.6\mathrm{ms}^{-1}$ in each component.

Example 2

The Gaussian shaped correlation function gives rather large values at short distances, underestimating errors at shorter wavelengths. Functions used operationally are more realistic. For instance Mitchell *et al.* (1990) suggest the "double-Toar":

$$\langle \varepsilon^{\psi}_{i} \varepsilon^{\psi}_{j} \rangle = E^{2}_{\psi} (1+\zeta)^{-1} \{ f(c,r_{ij}) + \zeta f(c/N,r_{ij}) \}$$

$$f(c,r_{ij}) = (1 + c r_{ij} + \tfrac{1}{3}c^{2}r^{2}_{ij}) \exp(-c r_{ij}). \tag{2.7}$$

With parameters again chosen such that E_v=5ms^{-1}, the r.m.s. error in the analyzed u and v components was 1.2ms^{-1}.

2.2 Analysis Correction Scheme

As well as these idealized simulations, we wished also to demonstrate that single-component winds could be used in a full-scale operational system.

The Met Office uses the Analysis Correction method (Lorenc *et al.* 1991) to produce global and regional analyses for operational NWP. The method performs a repeated insertion of observational data into a forward running assimilation model, with each insertion being similar to one iteration of a successive correction method. If **x** is the model wind field, and **y** is the observed vector, then the correction equation is

$$\mathbf{x}_{u+1} = \mathbf{x}_{u} + \mathbf{W}\,\mathbf{Q}\,(\mathbf{y}-K(\mathbf{x}_{u})). \tag{2.8}$$

W is a weight matrix proportional to the background error covariances. **Q** is a normalization factor, depending on the data density. For optimal convergence of the iteration it should be given by

$$\mathbf{Q} = (\mathbf{I} + \mathbf{KW})^{-1}. \tag{2.9}$$

In practice a diagonal approximation to this is used.

If only one component of the wind is observed, then only that component of the covariance tensor should be used. Rather than performing the coordinate transformations required for this, we instead created a vector increment with zero component in the unobserved direction, and used the **W** appropriate for a full vector. This has identical effect, except in the calculation of **Q** (which is already an approximation).

It was not our intention at this stage to simulate a full global distribution of windlidar observations; full Observing System Simulation Experiments are planned for later. We therefore obtained single-component winds by taking only one component from conventional wind observations; in one experiment radiosondes, in another, single level tropical winds (SATOBs and AIREPs). Four days of operational data from December 1987, and the operational assimilation system were used. In the tropical wind experiment, four parallel data assimilations were run: controls using all, and none of the single level data, and two simulations of windlidar winds. Of the two using simulated lidar winds, the first used a single component of each wind, the second simulated an instrument designed precisely to align the same number of shots in pairs, giving vector observations at half the positions. Figure 2.1 shows the fit of the 6-hour forecasts (produced in the assimilation to aid quality control of observations) to wind data. It can be seen that the two windlidar simulations have the same accuracy; there is no advantage, therefore, in aligning the shots to make vectors.

The tropical wind observations used to simulate the windlidar had a suitably extensive horizontal coverage, but were only at a few levels. In the experiment using radiosondes the vertical coverage was better, but horizontally the data were sparser than a windlidar's would be. Yet the main conclusion was the same: the impact of the observations was as expected from the number of data values; there was no detrimental effect from having single component winds.

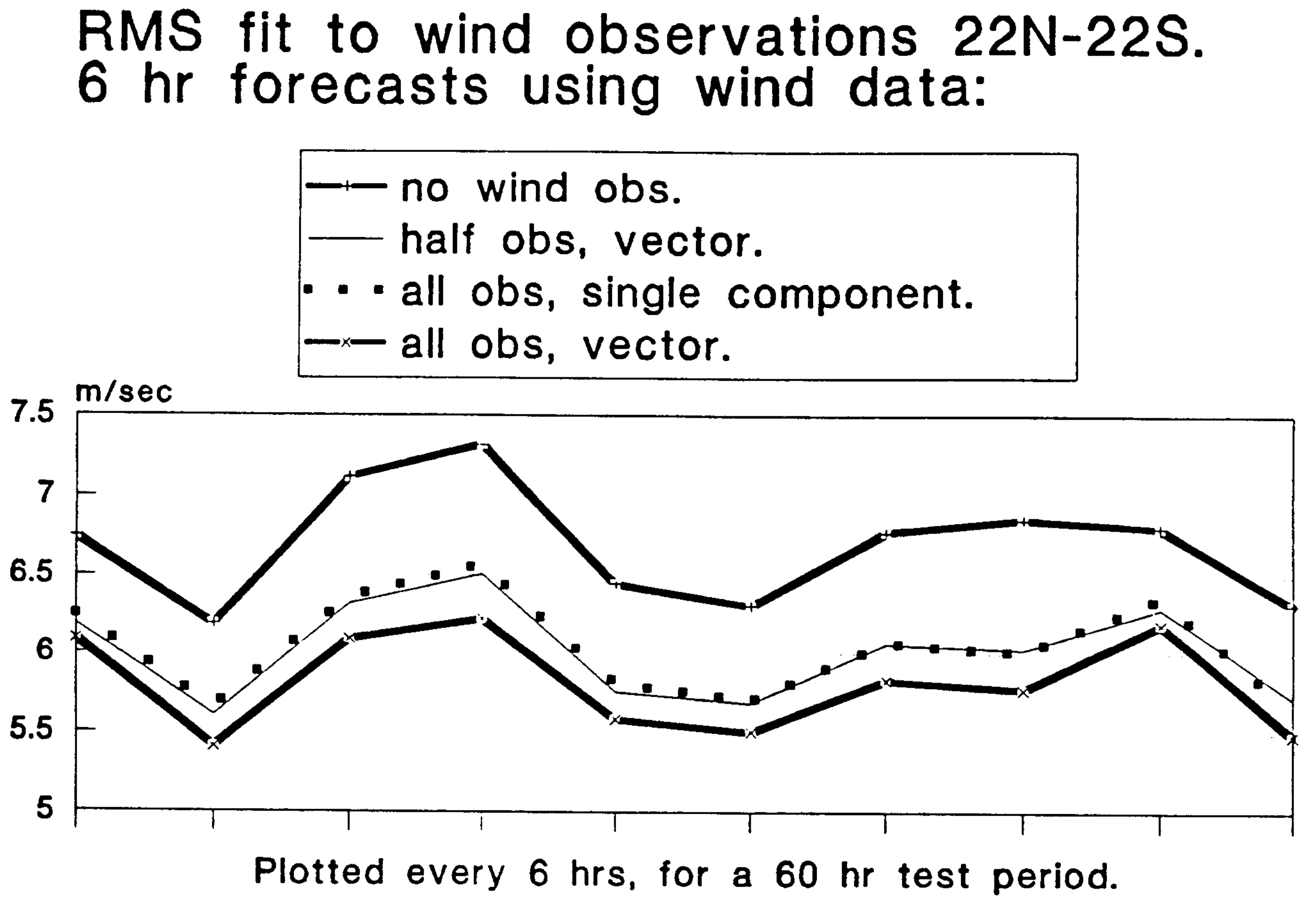

Figure 2.1. RMS fit of 6-hour forecasts to wind observations in the tropics. Thick lines show results from control assimilations, using none and all of the single level wind observations. Dots show results using a single component from each wind. The thin line shows results using the same number of data as the dots, but arranged to coincide to give vector winds.

3 Treatment of Gross Errors

Döppler windlidar requires the detection of a return signal from the target volume, and the measurement of its frequency shift. An idealized coherent signal processing system is to mix the return signal with a reference signal, detect, digitize, and Fourier analyse[1]. The peak frequency in the power spectrum is detected, and its frequency calculated. It is assumed that this is the beat frequency between the Döppler shifted return signal and the reference; hence the target velocity is calculated. In this section we are concerned with cases where this assumption is incorrect, and the wind returned contains no useful information about the real wind. Unless such occurrences are very infrequent, the error distribution of the observations will be significantly non-Gaussian. Most operational analysis methods, which are linear in the observed values, have an implicit assumption that the distribution is Gaussian (Lorenc 1988). For such methods, a preliminary quality control step, passing data with an approximately Gaussian error distribution, is necessary.

3.1 Error model

In practice it is necessary to limit the sampling of the signal in such a way that the fourier analysis returns only a limited range of frequencies; higher frequency signals alias onto this range. Noise from the instrument and signal processing appears over the whole of the range; the signal has to be detected as standing out above the noise. Where there is a strong reflector in the atmosphere, this should be the case; a clear peak will be identifiable. But clean air is likely to give a weak return signal, which rather often might be only just detectable. In striving to detect these weak signals a significant number of gross errors might be made by falsely identifying a random peak in the background noise as the signal.

This physical description of the error mechanism leads to a simple model of the errors of the derived winds: either a wind is from a correct spectral peak, in which case it will have errors which can be represented by a Gaussian distribution, or it is from a false peak, in which case any value from the processing output range is equally likely. The probability of the latter, gross error, occurring is P_g. We assume that the output processing range is centred on $\hat{o}$ (a prior estimate of the wind) and extends to $\pm a$. We neglect the

---

[1] We note that real processing algorithms (e.g. pulse pair, covariance based methods) may not use Fourier transforms, but the structure of their errors is likely to be similar.

aliasing of good data with large Döppler shifts onto lower frequencies, and the truncation of the Gaussian distribution. The probability of getting an observed value between o and o+do, if the true value is u, is p(o|u)do, where:

$$p(o|u) = \begin{cases} \dfrac{(1-P_g)}{\sigma\sqrt{2\pi}} \exp\left(-\dfrac{(o-u)^2}{2\sigma^2}\right) + \dfrac{P_g}{2a}, & \hat{o}-a< o <\hat{o}+a \\ 0, & \text{otherwise} \end{cases} \qquad (3.1)$$

This type of error model is used for operational quality control at the Met Office (Lorenc and Hammon, 1988). The example used for tests is shown in figure 3.1.

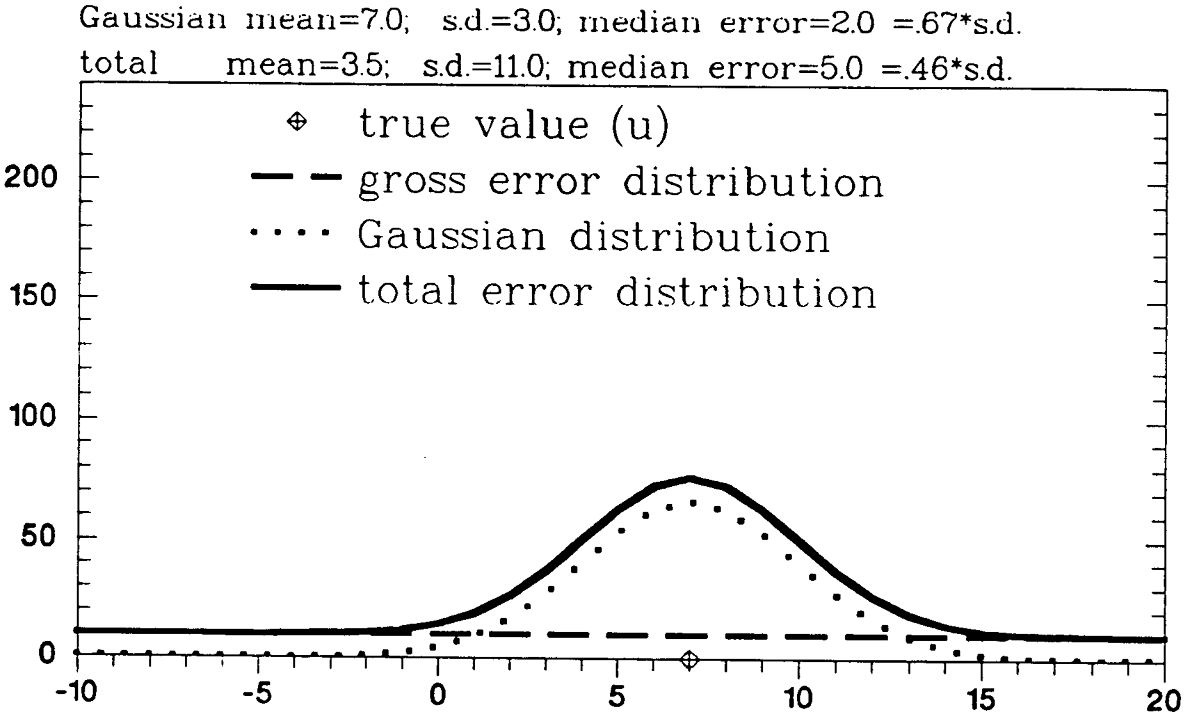

Figure 3.1 Assumed distribution of errors for Döppler velocities from weak signals. Parameters in (3.1) are: $P_g=0.5$,
for good data a Gaussian with $u=7$ ms^{-1}, $\sigma=3$ (dotted),
for gross errors a constant density with $\hat{o}=0$ ms^{-1}, $a=25$ ms^{-1} (dashed).
The scaling is such that the total distribution (solid) can be compared with with histograms of 1000 trials shown in later figures. Note that only a portion of the range from -a to +a is shown.

Again ignoring the truncation of the Gaussian, the mean and variance of p(o|u) are:

$$\bar{o} = (1-P_g)\ u + P_g\ \hat{o} \qquad (3.2)$$

$$V = (1-P_g)\ (\sigma^2+(u-\bar{o})^2) + P_g\ (a^2/3+(\hat{o}-\bar{o})^2) \qquad (3.3)$$

Note that for large P_g and a, the second term (corresponding to the long tails of the distribution) will dominate in (3.3). The variance (or its square root, the standard deviation) is not a good measure of the information content of such a distribution. A simple measure which is less sensitive to the tails is the median absolute error. For a Gaussian this equals 0.67σ, for a long tailed distribution the ratio is less. These distribution parameters are shown on figure 3.1 and subsequent similar figures.

It should be noted that while the median error better characterizes the width of the peak of good data, it is the standard deviation which determines the variance reduction in a linear analysis of the data.

3.2 Averaging techniques

In this section we study techniques for coping with gross errors if there are several independent observations of the same parameter. That is, we assume that data from the windlidar are close enough that differences in the real wind due to separation in space are small compared to the observation error. We study ways of combining several data to give a value which has an error distribution more suitable for most analysis methods.

3.2.1 Simple average

The simplest way of combining the data is to take their mean. If we have m data, then the variance will be V/m. Although the error distribution of these meaned data will be more nearly Gaussian than (3.1), it will be biased in accordance with (3.2), and have rather large variance. Figure 3.2 illustrates this.

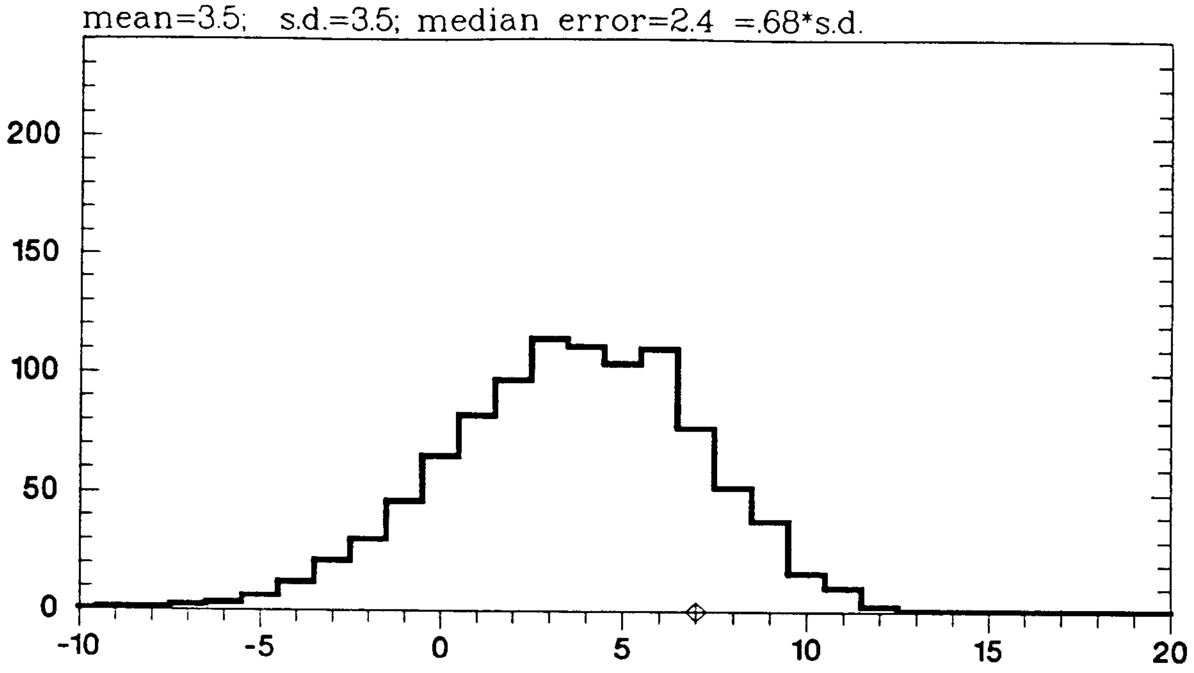

Figure 3.2. Histogram of means of 10 observations generated at random from the distribution shown in figure 3.1. Note that it is biased from the true value u.

3.2.2 **Angular average**

Because of the frequency aliasing of the Döppler processing, the derived velocity should be averaged like an angular variable. Defining complex numbers α_i whose direction on the complex plane is related to o_i, we can find the direction of their average, and convert back to an angular average wind:

$$\alpha_i = \exp\left(\frac{i\pi}{a} o_i \right)$$

$$\bar{\alpha} = \frac{1}{m} \sum_{i}^{m} \alpha_i \tag{3.4}$$

$$\bar{o}_{ang} = \frac{a}{i\pi} \ln(\bar{\alpha}/|\bar{\alpha}|)$$

Results using this method are shown in figure 3.3.

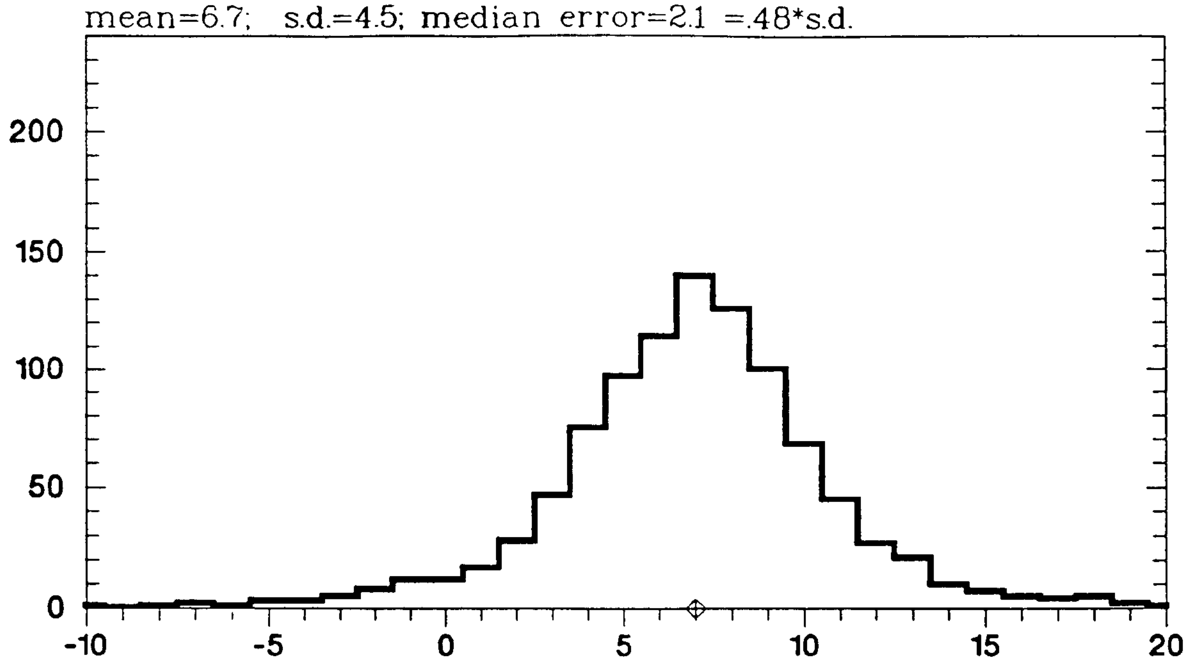

Figure 3.3. As figure 3.2 for angular means made using (3.4). Note that the bias is cured, but the standard deviation and median error are similar to those of figure 3.2.

3.2.3 Consensus average

Neither of the above averaging methods take account of the non-Gaussian nature of the observation errors. In our simple error model, gross errors contain no useful information. So a reasonable approach is to choose a subset of data which agree and hence are less likely to have gross errors, and only average those. This is called a consensus average. We find subsets containing observations all within X ms^{-1} of each other. The subset containing the most observations is used to calculate the consensus average, provided there are at least n_c points contained in that subset. X and n_c are parameters set by the user. If a subset which contains at least n_c points cannot be found then no value is returned. Strauch et al (1984) used this method to process the Döppler wind data from wind-profilers, with X=1-2 ms^{-1} and n_c=4 for sets containing 12 observations.

A simple Monte Carlo simulation can be performed to determine the effectiveness of the consensus average method. m random numbers are generated from the probability distribution given by (3.1) and these represent a set of observations of u. The consensus average is then determined as described above. The results from 1000 simulations using parameter values, $u=7ms^{-1}$, $\hat{o}=0ms^{-1}$, $\sigma=3ms^{-1}$, $a=25ms^{-1}$, $P_g=0.5$ and m=10 are summarized in tables 3.1 and 3.2.

nc	X (ms^{-1})							
	2.0	3.0	4.0	5.0	6.0	7.0	8.0	9.0
3	74%	91%	97%	100%	100%	100%	100%	100%
4	27%	52%	71%	83%	90%	95%	97%	99%
5	6%	19%	34%	51%	63%	72%	80%	85%
6	1%	5%	12%	23%	35%	44%	54%	61%

Table 3.1. Percentage of runs for which a value for the consensus average is returned.

nc	X (ms^{-1})							
	2.0	3.0	4.0	5.0	6.0	7.0	8.0	9.0
3	4.1	4.8	4.1	4.2	4.1	4.2	3.6	3.3
4	1.9	3.1	2.8	3.2	3.2	3.5	3.2	3.8
5	1.8	1.7	1.9	1.8	2.1	2.7	2.7	2.4
6	0.7	1.8	1.4	1.5	2.2	1.6	1.8	2.0

Table 3.2. The standard deviation of the returned consensus average values in units of ms^{-1}.

Table 3.1 shows the percentage of runs in which a value for the consensus average is returned for various values of X and nc. The more strict criteria for consensus, small X and large nc, are met less often. Table 3.2 shows the standard deviation of the consensus averages. The more strict criteria give more accurate results. As well as affecting the standard deviation, the criterion also affects the shape of the distribution. A typical histogram for the distribution of the consensus average values with $X=9ms^{-1}$ and nc=4 is shown in figure 3.4. This is still significantly non-Gaussian, with long tails. The shape of these histograms appear to be similar to figure 3.1. If we assume that the probability density distribution for the consensus average values is of the form given by (3.1) then a least squares fit can be used to determine σ_{ca} and Pg_{ca} where the subscript ca denotes that the parameters are for the distribution of the consensus average values. For $X=9ms^{-1}$ and nc=4, we find that $\sigma_{ca}=1.7ms^{-1}$ and $Pg_{ca}=0.12$. For $X=5ms^{-1}$ and nc=4 we find $\sigma_{ca}=1.8ms^{-1}$ and $Pg_{ca}=0.06$. We see from table 3.1 that this increase in reliability is bought at a cost of having no return from 17% of the samples of 10 data.

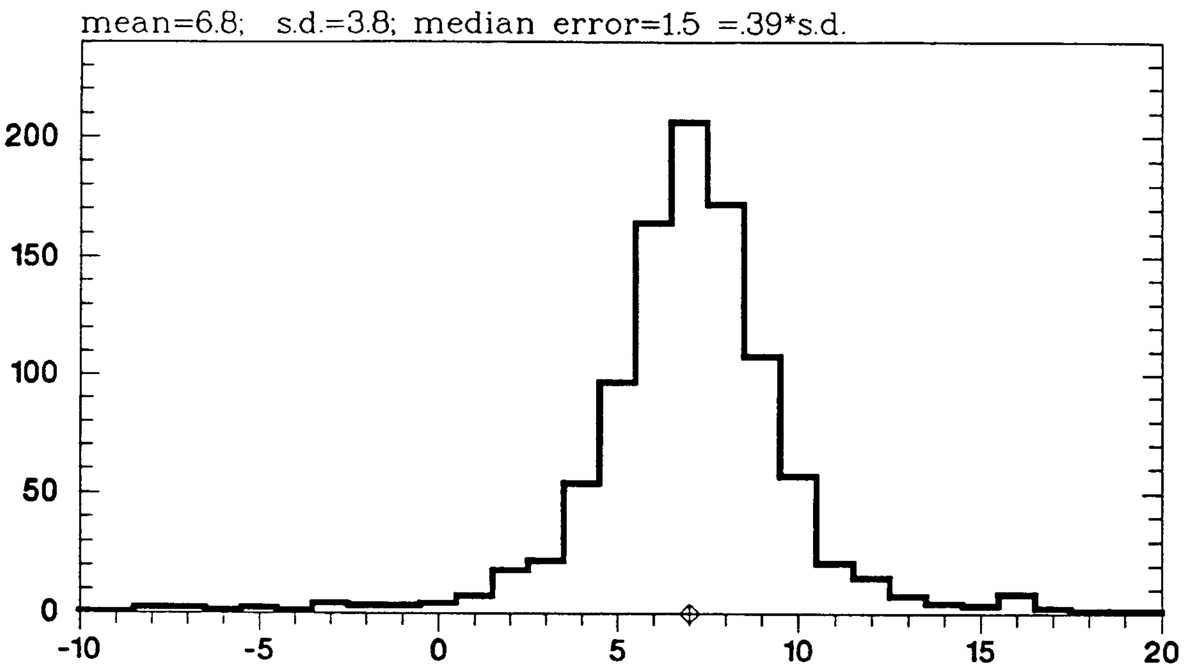

Figure 3.4. As figure 3.2 for consensus averages. Note that both the standard deviation and median error are smaller than those of figure 3.2 and figure 3.3.

3.2.4 Maximum Probability Method

We have m observations of the same wind velocity $o_1, o_2, \ldots o_m$, with known error distribution. We can hence calculate the probability that the true velocity is between u and u+du. Using Bayes theorem, the probability density function is given by

$$p(u|o_1,o_2,..o_m) = p(o_1,o_2,..o_m|u)p(u) \;/\; p(o_1,o_2,..o_m) \qquad (3.5)$$

Assuming that the errors in each datum are independent, we have

$$p(o_1,o_2,..o_m|u) = \prod^{m} p(o_i|u). \qquad (3.6)$$

The simplest maximum probability method only requires relative probabilities; the denominator of (3.5) is not needed:

$$p(u|o_1,o_2,..o_m) \propto \prod_{i=1}^{m} p(o_i|u)\; p(u). \qquad (3.7)$$

It can be found if needed for more sophisticated methods by integrating (3.7) over all u.

We assume no *a priori* knowledge of u and therefore p(u) is taken to be constant. Using the above equations and (3.1) it is relatively simple to calculate the probability density function $p(u|o_1,o_2,..o_m)$, provided that the values for σ and P_g are known. Examples of the form of the calculated probability density function $p(u|o_1,o_2,...o_m)$ are given in figure 3.5. Note that there are usually secondary maxima. If $P_g=0$ then the individual and combined functions would be Gaussian, and the maximum would be at the mean of the observed data. For $P_g>0$ the most likely value for u corresponds to the largest maximum.

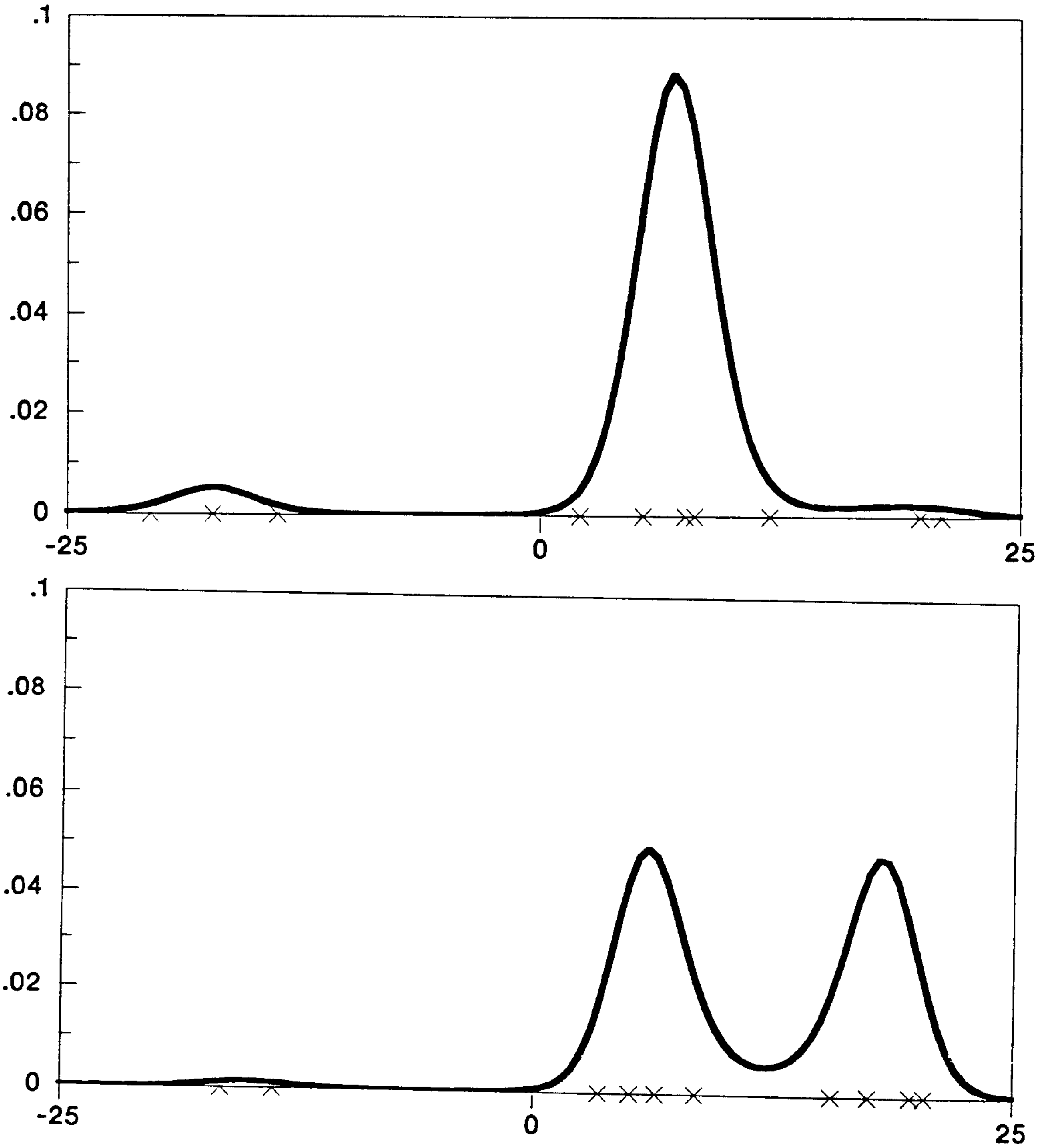

Figure 3.5. Typical probability density functions calculated using (3.6). The Xs on the bottom axis mark the values of the ten simulated data, generated randomly from the distribution shown in figure 3.1.

The method can be extended to more sophisticated definitions of the best value for u than this. For instance the integral over a limited range (related to σ) could be maximized. The value of this integral could be related to a probability of gross error in the returned estimate u. If this is too large, the estimate could be rejected. For instance we might well not want a value returned from the second example in figure 3.5, since the probability that the central peak is correct is only about 0.5. There are two sub-groups, each with 4 data which agree. Criteria to flag results from such cases as unreliable can be added to consensus average techniques also. Thus both methods can be tuned to give more reliable estimates at the cost of returning fewer results.

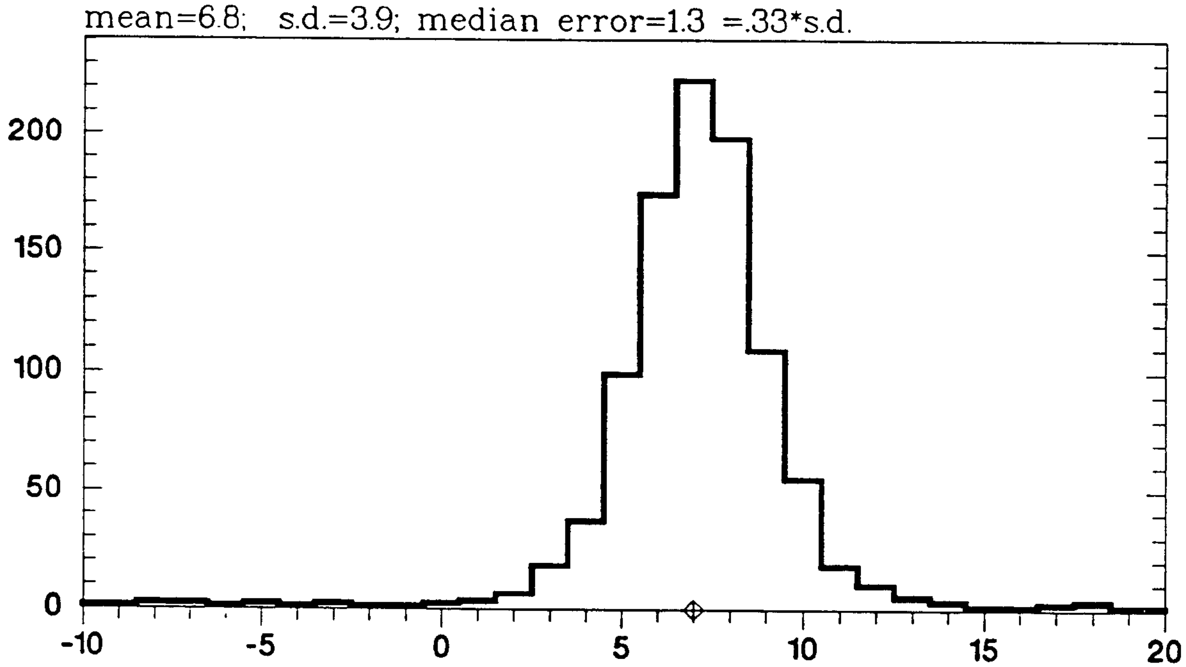

Figure 3.6. As figure 3.2 for maximum probability values. Note that both the standard deviation and median error are similar to those of figure 3.4.

Figure 3.6 shows the histogram resulting from a maximum probability method. Results are very similar to the best results obtained from the consensus average method. If we assume that there is some limit on the ability of any algorithm to separate 'good' observations from 'bad', then the similar performance of the consensus average and maximum probability methods suggest that both of these methods can perform at or near this limit. Therefore significant improvements cannot be expected by using more sophisticated algorithms, unless more information is included in the algorithm. An immediate advantage of the maximum probability method over the consensus average method is that any a priori knowledge of u (e.g. from short-range forecast) can easily be included by putting

$$p(u)=\frac{1}{\sigma_b\sqrt{2\pi}}\exp\left(-\frac{(u-b)^2}{2\sigma_b^2}\right), \qquad (3.8)$$

where b is an estimate of u from the short range forecast. Results from this, with σ_b=5ms^{-1}, are shown in figure 3.7. The additional information is particularly useful in reducing the number of returned values in the tails of the distribution.

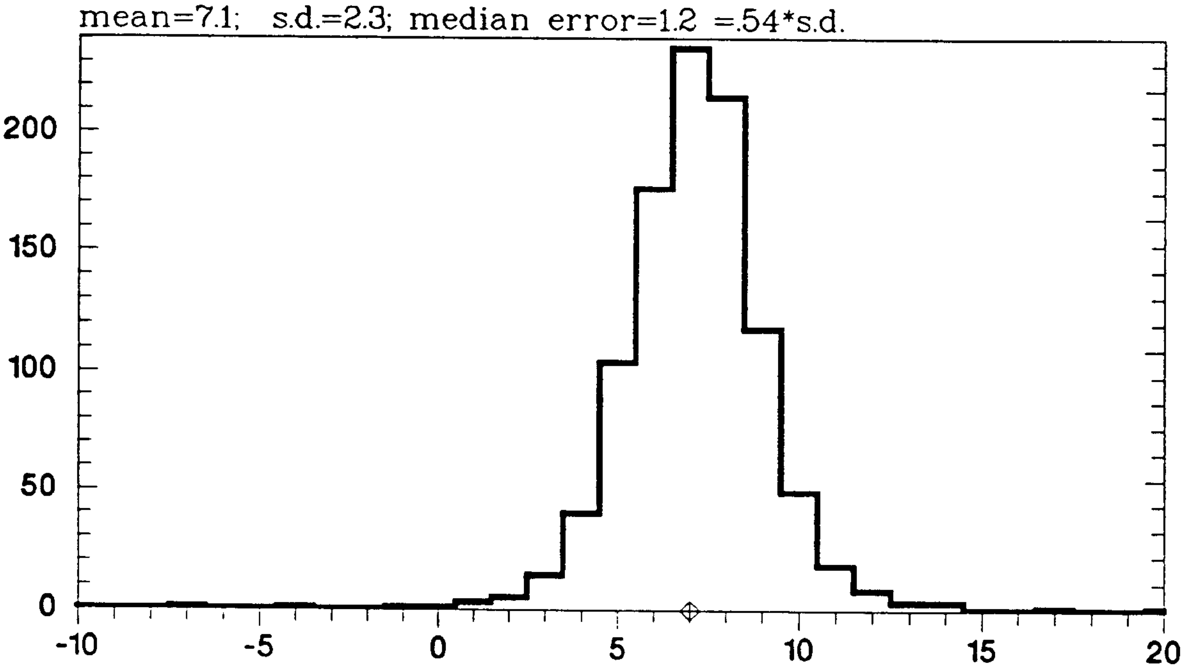

Figure 3.7. As figure 3.6, including information from an background estimate in the maximum probability calculation. Note that the standard deviation is significantly smaller than that of figure 3.6. This distribution is more nearly Gaussian.

This study shows that care must be taken when combining data from Döppler processing of weak signals. Minimum variance type methods are not sufficient; it is necessary to examine the value returned by each observation before deciding what weight to give it. Consensus averaging is a suitable practical method. With appropriate parameters it gives similar results to the more theoretically based maximum probability method.

Neither method gave results with an error distribution that was near Gaussian in our tests, unless parameters were chosen which resulted in losing many observations. This is in agreement with practical experience using wind-profiler data data formed as consensus averages of ten 6-minute values. These hourly average values are still in need of further quality control (Brewster and Schlatter 1988).

If prior information is incorporated into the process of combining the data, it can be very useful in avoiding gross errors. In our example it gave a distribution that was probably sufficiently near to Gaussian to allow the data to be used directly in a linear analysis method.

3.3 Nonlinear analysis

We saw in figure 3.7 that the inclusion of *a priori* information into the decision process significantly improved the decisions as to which data to believe. It follows that ideally such decisions should be postponed until as much independent outside information as possible has been collected. The process of data assimilation is designed to bring together, organize, and reconcile all available information; processing of non-Gaussian data should ideally be an integral part of the assimilation, rather than a preliminary step. Of course practical constraints on communications, computing, and complexity of algorithm may limit this ideal. Here we investigate the feasibility of extending the maximum probability method to observations distributed in two-dimensions, combining the decision process with objective analysis. Purser (1984) suggested how an analysis scheme could directly treat observations containing non-Gaussian errors; some work on this method has already been carried out by Lorenc (1988). We compare results from this nonlinear combined quality control and analysis with more conventional two-stage methods.

In the averaging example in 3.2.4, the best value of a single output parameter had to be estimated. It was feasible to search all possible values to find this. In the analysis problem, many parameters have to be estimated (e.g. the values at a grid of points); it is not feasible to do a comprehensive search of a multidimensional phase space. Instead we use an iterative algorithm. For simplicity we derive this first for the averaging problem. We start from (3.7), with p(u) given by (3.8), and define a penalty function J:

$$J(u) = -\ln\left\{\frac{1}{\sigma_b\sqrt{2\pi}}\exp\left(-\frac{(u-b)^2}{2\sigma_b^2}\right)\prod_i p(o_i|u)\right\} + \text{constant}. \qquad (3.9)$$

Minimizing J is equivalent to maximizing the probability. The logarithm converts the product into a summation, which is easier to handle:

$$J(u) = \frac{(u-b)^2}{2\sigma_b^2} - \sum_i \ln\left\{ \frac{(1-P_g)}{\sigma\sqrt{2\pi}} \exp\left(- \frac{(o_i-u)^2}{2\sigma^2} \right) + \frac{P_g}{2a} \right\}. \tag{3.10}$$

We have substituted (3.1) and omitted the constant. A Newton iteration to find the minimum of (3.10) is:

$$u_{t+1} = u_t - (J''(u_t))^{-1}\, J'(u_t), \tag{3.11}$$

where t is the iteration counter, and J' and J'' are the first and second derivatives of J with respect to u. Applying (3.11) to (3.10) we get

$$u_{t+1} = u_t + \frac{b-u_t + \sum_i \sigma_b^2\, \varepsilon(o_i,u_t)\, (o_i-u_t)}{1 + \sum_i \sigma_b^2\, \varepsilon(o_i,u_t)}, \tag{3.12}$$

where

$$\varepsilon(o_i,u_t) = \frac{1}{\sigma^2} \left\{ \frac{\dfrac{(1-P_g)}{\sigma\sqrt{2\pi}} \exp\left(- \dfrac{(o_i-u_t)^2}{2\sigma^2} \right)}{\dfrac{(1-P_g)}{\sigma\sqrt{2\pi}} \exp\left(- \dfrac{(o_i-u_t)^2}{2\sigma^2} \right) + \dfrac{P_g}{2a}} \right\}. \tag{3.13}$$

The term that multiplies $1/\sigma^2$ in (3.13), reducing the weight given to the observation, is the posterior probability that observation i does not have a gross error, given that u_t is correct (Lorenc and Hammon 1988). When this is small, the observation is effectively rejected:

$$P(\bar{g}|u_t) = \left\{ \frac{\dfrac{(1-P_g)}{\sigma\sqrt{2\pi}} \exp\left(- \dfrac{(o_i-u_t)^2}{2\sigma^2} \right)}{\dfrac{(1-P_g)}{\sigma\sqrt{2\pi}} \exp\left(- \dfrac{(o_i-u_t)^2}{2\sigma^2} \right) + \dfrac{P_g}{2a}} \right\}. \tag{3.14}$$

Note that the iteration (3.12) does not find the absolute minimum of J. If it is started from u_0=b, and b is reasonably accurate, then in most in cases the minimum found (typically in five iterations in our example) is acceptable. But without this background information, the iteration could converge to any of the secondary minima apparent in figure 3.5.

We can extend this to the analysis problem, with observations distributed in space, by considering the u_i and b_i at each observation position. As in section 2.1, we manipulate these in vectors **u** and **b**. (As we are for the moment dealing only with values at observation positions, we do not need to explicitly represent subscripts i and j, like we did in 2.1). We also use the background error covariance, defined in 2.1. (3.10) becomes

$$J(\mathbf{u}) = (\mathbf{u}-\mathbf{b})^T B^{-1}(\mathbf{u}-\mathbf{b}) - \sum_i \ln\left\{\frac{(1-P_g)}{\sigma\sqrt{2\pi}} \exp\left(-\frac{(o_i-u_i)^2}{2\sigma^2}\right) + \frac{P_g}{2a}\right\}. \qquad (3.15)$$

Substituting the derivatives of this in (3.11) we get the equivalent of (3.12)

$$\mathbf{u}_{t+1} = \mathbf{u}_t + \mathbf{Q}_t\ (\ \mathbf{b}-\mathbf{u}_t + \mathbf{B}\ \mathbf{E}_t^{-1}(\mathbf{o}-\mathbf{u}_t)) \qquad (3.16)$$

where

$$\mathbf{Q}_t = (\ \mathbf{I} + \mathbf{B}\ \mathbf{E}_t^{-1}\ )^{-1} \qquad (3.17)$$

and $\mathbf{E}_t^{-1}$ is the a diagonal matrix whose i th diagonal element is given by $\varepsilon(o_i,u_{i,t})$ as defined in (3.13). Iteration of (3.16) and (3.17) requires a matrix inverse each step to evaluate $\mathbf{Q}_t$. An approximation for $\mathbf{Q}_t$, similar to that used in the AC scheme, is possible. We take $\mathbf{Q}_t$ to be diagonal, with its i th element $q_{i,t}$ given by

$$q_{i,t} = (\ 1 + \sum_j |B_{ij}|\ \varepsilon(o_j,u_{j,t})\ )^{-1}. \qquad (3.18)$$

This reduces the computation, while still converging to the same minima. Once the best estimate analysis at the observation positions is found, the analysis values at grid points can be found from

$$u_k = B^T_{ik} B^{-1}_{ij}(u_i-b_i). \qquad (3.19)$$

Here we have used subscripts i and j to indicate values at observation positions, and k to indicate values at grid points, as in section 2.1.

To demonstrate this system, we repeated the examples of 2.1. With P_g set to zero, results were identical, as expected (Lorenc 1986). With P_g=0.5 then using (3.17) took about twenty iterations to converge. Using (3.18) took more iterations, but less computation. Table 3.3 shows the convergence for one simulation using (3.18).

Number of iterations, k=	0	1	10	20	50	100	200	300	500
RMS Error in components at observation positions(ms^{-1})	6.4	5.2	2.2	2.0	1.7	1.6	1.5	1.5	1.5

Table 3.3 RMS error of $\mathbf{u}_k$ for observations distributed as in example 2 of section 2.1, with P_g=0.5, σ=2.5ms^{-1}, σ_b=5ms^{-1}.

Nine simulations with different random errors were performed; for each the analysis was evaluated using (3.19) at an analysis grid like that used in the OI example in section 2.1. Values of the analysis errors are shown in column 1 of table 3.4. The average value of 1.8 ms^{-1} is of course larger than the 1.2 ms^{-1} obtained using OI in section 2.1 (and using P_g=0 in this scheme), because half of the data contained no useful information. It is only very slightly larger than the OI error obtained with half the data (1.7 ms^{-1}), indicating that uncertainty about which data were incorrect contributed little to the nonlinear analysis error. This analysis system is used to evaluate various scenarios in section 5, with P_g up to 0.75. Even in this case the nonlinear analysis performed well.

case	Nonlinear analysis	QC in 500×500km boxes then OI analysis	QC in 300×300km boxes then OI analysis
1	1.4	1.9	1.7
2	1.8	1.9	2.0
3	1.8	2.5	3.7
4	1.8	2.0	2.0
5	2.1	1.8	1.9
6	2.4	2.4	1.8
7	1.7	2.0	2.7
8	1.3	1.2	1.6
9	1.7	1.9	1.7
average	1.8	2.0	2.2

Table 3.4 RMS error in ms^{-1} for analysed wind components over a simulated swath of windlidar observations as in section 2.1 example 2. Results are shown for the nonlinear analysis of section 3.3, and for separate quality control and analysis steps as described in section 3.4.

3.4 Variational analysis used for quality control

Using all observations together, as in the ideal nonlinear variational analysis, is computationally expensive, and difficult to organize. Preprocessing of observations in small batches, using a background field but no other observations, is easier. In this section we set out to see how much is lost by this approach. The observations were divided into small batches, each of which was processed separately by the nonlinear variational scheme (using the same background information as before). For each observation, its posterior probability of a gross error, assuming the resulting mini-analysis to be correct ($P(\bar{g}|u_t)$), was calculated using (3.14). Only those observations with $P(\bar{g}_i|u_t)>0.5$ were passed to an OI analysis, which combined all the observations using (2.3). The last two columns of table 3.4 show the accuracy of analyses resulting from this scheme, for two sizes of preprocessing box. It is clear that reducing the amount of information used in the quality control stage significantly increases the analysis error. We conclude that in the circumstances of our simulation, with a background field available from a good short-period forecast, a nonlinear analysis accounting for non-Gaussian errors is better than a (simpler) prior quality control step and a linear analysis.

4 Estimation of errors of representativeness in single-shot single-component Döppler lidar winds.

4.1 Introduction

The procedure for simulating observations for use in an observation system simulation experiment (OSSE) may be considered to comprise three steps.

1) Interpolation of the NWP "nature" run to obtain the "observed" variable at the required observation time and location.

2) Adjustment of the interpolated value to take account of the small scale atmospheric variability which is not represented in the NWP "nature" run, but which will be sampled by the observation - i.e. consideration of the so-called representativeness errors.

3) Further adjustment to take account of the measurement error characteristic of the observing instrument and any errors incurred during data processing.

The purpose of this section is to specify the representativeness errors (step 2) appropriate for the simulation of single-shot single component Döppler lidar winds.

The magnitude of the representativeness errors will depend on the resolution of the NWP model used to generate the nature run, we shall assume that the model used has a grid resolution of 100km. In part of our analysis we shall refer to fields from the UK Cyber global model, which has a horizontal grid of resolution ~170km. We consider the representativeness error to comprise three parts;

a) Horizontal representativeness error: The lidar shots will have a horizontal scale of order ~10m and will sample motion on this scale. By comparison the shortest scales that can be resolved in the nature run are of order ~200km (twice the model grid length). It is clear that small scale structure in the wind field, which will be resolved by the lidar observations, will not be present in the nature run. This small scale "roughness" must therefore be quantified and modelled in order to produce a realistic simulation of the lidar data.

b) Vertical representativeness error: Errors of vertical representation are likely to be much smaller than those of horizontal representation - since the vertical resolution of the nature run and the vertical scale of the lidar shot are similar (~500m). However, errors of vertical representation will increase where aerosol stratification reduces the effective vertical resolution of the shot, and consideration of this effect will therefore be included in our analysis.

c) Vertical velocity "aliasing": The horizontal wind component will be readily obtained from the measured line of sight (LOS) wind if the component of vertical velocity along the LOS is neglected (alternatively the component of vertical velocity could be estimated from an NWP "first guess" field). Errors arising from the neglect of the vertical component are termed vertical velocity "aliasing" errors - and we shall include an assessment of their magnitude in our estimate of the representativeness error. Vertical wind speeds are typically small compared to horizontal wind speeds, and therefore the neglect of the vertical component will be justified in most cases. However, in local regions where the vertical velocity is large (order $1ms^{-1}$ or more), its neglect will result in significant error in the derived horizontal wind.

In section 4.2 spectral analysis of wind data and NWP model wind fields is used to estimate typical values of the three error components described above. The estimates are derived from averaged spectra, and will therefore represent an "average" or "background" contribution to the local representativeness error. The "background" value should be appropriate for most situations; however, in meteorological regimes characterised by above average "roughness" in the wind field the background value will be an underestimate. We therefore give special consideration, in section 4.3, to a number of regimes (e.g. boundary layer flows), for which wind variability is typically above average.

4.2 Use of spectral analysis to estimate "background" representativeness errors

4.2.1 Horizontal representativeness errors

To estimate the horizontal representativeness error we have analysed wind spectra from 3 sources, described below.

1) *Published spectra*: Lilly and Petersen (1983) have presented a number of wind spectra, obtained by various workers, in a common format. The individual spectra show similar characteristics, and suggest an overall average which we

shall use as a reference, and refer to as the LP spectrum.

2) *Spectra obtained from Meteorological Research Flight (MRF) wind measurements.* Wind spectra have been derived from measurements made by the MRF C130 over 35 flight segments of average length 490km, and at altitudes between 20,000 and 26,000ft. Of the 35 segments 32 were obtained during the Mesoscale Frontal Dynamics Project (MFDP), and therefore include flights in or near cold front jet streams. We use this dataset to provide information on the increase in representativeness error likely in jet flows.

The method of processing the MRF data was as follows. The raw data (recorded at 16Hz resolution) were extracted at 5sec resolution and smoothed over 5sec intervals. Spectral analysis of the wind speed was performed using a fixed baseline of 1024 grid points for each flight sector. The data were first de-meaned and tapered (25% at each end) using a split cosine bell function, and then either padded with zeros or wrapped around depending on whether the actual number of 5sec means was less than or greater than 1024. Using Taylor's "frozen" turbulence hypothesis, and assuming an aircraft speed of 150ms^{-1}, the frequency spectra were converted to wavenumber representation. Spectra from individual sectors were combined by weighting each according to the length of the sector. To investigate the dependence of wind variability on wind speed, each sector was classified according to the mean wind speed along the sector; four wind speed bands were considered - 0-30ms^{-1}, 30-40ms^{-1}, 40-50ms^{-1} and 50-60ms^{-1}. Combined spectra were then produced for each of these mean wind speed bands.

3) *Model wind spectra.* Wind spectra derived from NWP wind analyses have been used to estimate the wind variance, on scales longer than 2 grid lengths, that will not be resolved by the nature run. For this purpose wind spectra were derived from the UKMO Cyber NWP model fields by sampling the model winds at 400mb along longitude lines from 90N to 90S. Ten such samples were spectrally analysed and average spectral amplitudes found.

The method of estimating representativeness errors from wind spectra is best illustrated by reference to figure 4.1, which shows the range of spectra discussed by Lilly and Petersen (continuous lines), the MRF combined spectrum for all 35 sectors (+s) and the spectrum derived from the model fields (circles). A line representing the average amplitude of the spectra discussed by Lilly and Petersen is also shown, and will be referred to as the LP spectrum. Note first that the model spectrum is truncated at a wavelength of

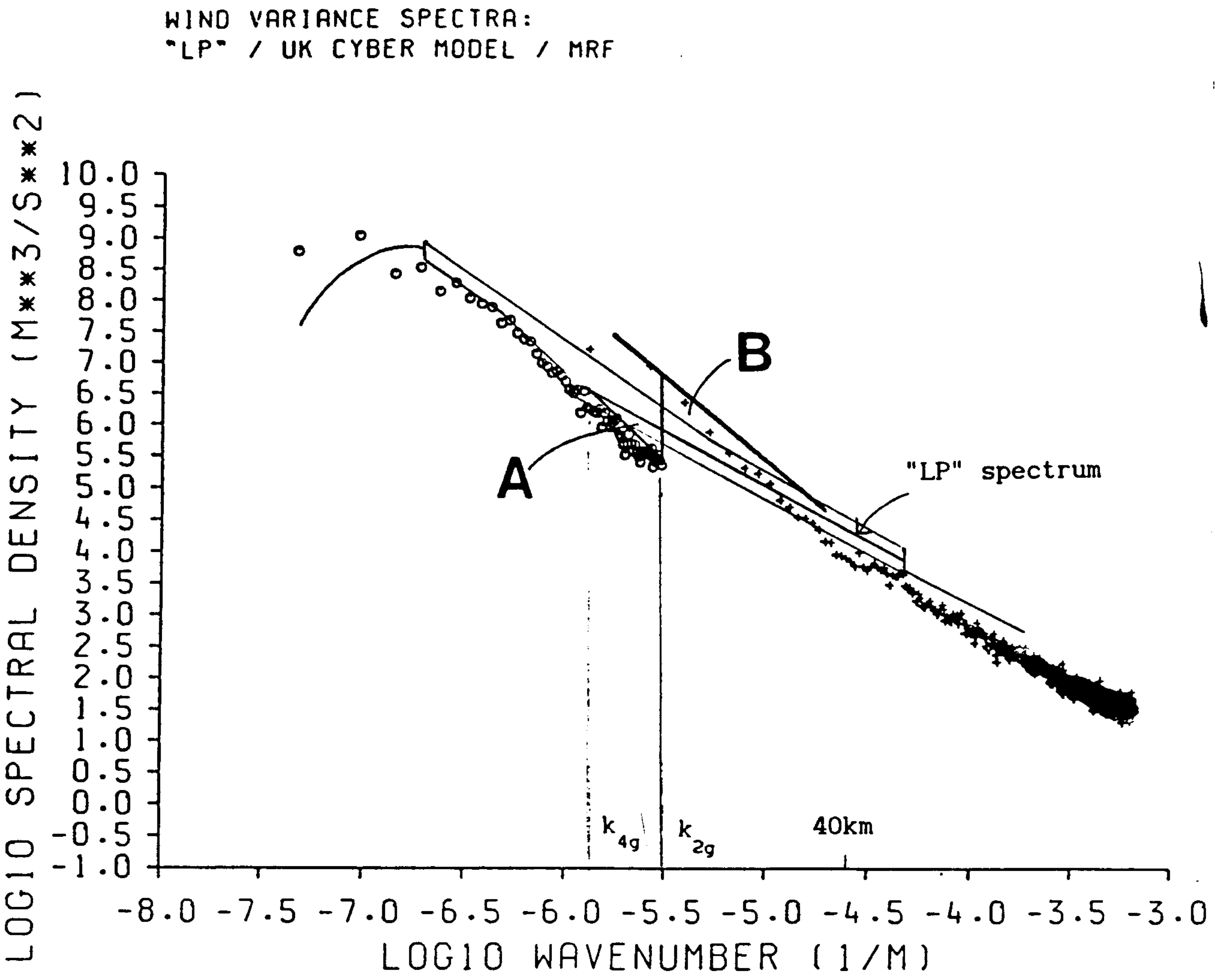

Figure 4.1: Wind variance power spectra generated from the MRF dataset (+s) and UK Cyber model winds (circles). The range of amplitudes in the spectra discussed by Lilly and Petersen (1983) is shown schematically, a line representing the average amplitude (over the range $10^{-5.9} > k > 10^{-4.3}$) is also shown, and is referred to in the text as the "LP" spectrum.

~340km, twice the model grid length (the corresponding wavenumber will be referred to as k_{2g}); variance contributed by motion on scales smaller than this cannot be resolved by the NWP model. Area under the spectral curves shown in figure 4.1 represents wind variance, and integration of the LP spectrum over all wavenumbers higher than k_{2g} gives an estimate for the magnitude of the variance unresolved by the Cyber NWP model. In the wavenumber interval $k_{2g} \rightarrow \infty$ the spectrum has a slope of -5/3, and the integration may therefore be written,

$$\sigma^2(\infty,k_{2g}) = \int_{k_{2g}}^{\infty} E(k)dk = \frac{3}{2}k_{2g}E(k_{2g}) \ . \qquad (4.1)$$

Taking values of k_{2g} and $E(k_{2g})$ from figure 4.1 gives $\sigma^2(\infty,k_{2g}) = 3.95m^2s^{-2}$. Integration of the LP spectrum therefore suggests that the loss of small scale detail in wind fields represented on a finite grid of grid length ~170km will result in an rms representativeness error in single wind components of $\sigma(\infty,k_{2g}) = 1.9ms^{-1}$.

Comparison of the model spectrum in figure 4.1 with the LP spectrum shows that energy in the model spectrum decreases more rapidly with increasing wavenumber. This implies that higher wavenumbers are not fully resolved in the model field. To estimate the unresolved variance at wavenumbers greater than k_{2g} we assume that 4 grid length waves (i.e. wavenumber $k=k_{4g}$) are fully resolved by the model and adjust the model spectrum (retaining the slope of the spectrum) to intersect the LP spectrum at $k=k_{4g}$. The triangular area marked **A** on figure 4.1 represents the unresolved variance over the wavenumber range $k_{4g} < k < k_{2g}$, and has been measured at $\sigma^2(k_{2g},k_{4g}) = 1.96m^2s^{-2}$. The overall unresolved variance may now be written

$$\sigma_h^2 = \sigma^2(\infty,k_{2g}) + \sigma^2(k_{2g},k_{4g}) = 3.95 + 1.96 = 5.91m^2s^{-2} \ ,$$

giving an overall horizontal representativeness error of $\sigma_h = 2.4ms^{-1}$.

The range of spectra discussed by Lilly and Petersen are strongly weighted to the level of the upper tropospheric wind maximum. As a result the estimate $\sigma_h = 2.4ms^{-1}$ is likely to be on the high side for low atmospheric levels and on the low side for the level of the jet stream itself. To assess the representativeness error appropriate for jet stream situations we discuss the results of spectral analysis of the MRF dataset which, as mentioned previously, contains a high percentage of measurements through jet streams.

Further reference to figure 4.1 shows that, at wavelengths shorter than 40km, the MRF spectrum and the LP spectrum have the same slope (-5/3). There is less energy in the MRF spectrum, however this is thought to be an artifact of the differences in initial smoothing and tapering of the data, and the amplitude of the MRF spectrum has been adjusted accordingly (continuous thick line in figure 4.1) so that the two spectra coincide at wavelengths below 40km. At wavelengths greater than 40km the energy in the adjusted MRF spectrum exceeds that of the LP spectrum - as a result of a more negative spectral slope in the former. The greater energy at these wavelengths is presumably a result of the greater sampling of jet stream activity in the MRF dataset in comparison to the datasets used in the Lilly and Petersen cases. The triangular area marked "B" in figure 4.1 represents a measure of the additional wind variance on scales $< k_{2g}$ that will be unresolved by the model in the vicinity of jet streams, and has been evaluated at $\sigma_J^2(\infty,k_{2g}) = 8.75\mathrm{m}^2\mathrm{s}^{-2}$. Assuming the unresolved variance in the range $k_{4g} < k < k_{2g}$ remains unchanged, the unresolved variance in jet stream flows may be estimated as

$$\begin{aligned} \sigma_h^2 = \sigma^2(\infty,k_{2g}) + \sigma_J^2(\infty,k_{2g}) + \sigma^2(k_{2g},k_{4g}) &= 3.95 + 8.75 + 1.96 \\ &= 14.66\mathrm{m}^2\mathrm{s}^{-2}. \\ \sigma_h &= 3.8\mathrm{ms}^{-1} \end{aligned}$$

A representativeness error of $3.8\mathrm{ms}^{-1}$ would therefore appear more appropriate for jet stream situations. Since this value is specific to jet flows it should represent an overestimate if used as a general rms error for the level of the jet stream. For a cautious estimate of the representativeness error associated with grids of resolution ~170km we may therefore specify σ_h in the range $2.4 - 3.8\mathrm{ms}^{-1}$, where the lower value is determined from the LP spectrum and the higher value, assumed to apply at jet levels, from the MRF spectrum.

As a check on the above estimate we may refer to values determined using other techniques for radiosonde wind observations, which sample the wind field on a scale similar to that of the single lidar shots. By comparing radiosonde observations with short range forecast fields Hollingsworth (1986) calculated vector rms observation errors for radiosondes in the range $2\text{-}3.5\mathrm{ms}^{-1}$ (single wind components), with the higher value corresponding to the jet stream level (~250mb). Hollingsworth's estimate, valid for a grid resolution of ~300km, is similar to the those obtained for a grid resolution of ~170km using the spectral method described above. For a second comparison we refer to the work of Kitchen (1989) who, using data from the U.K radiosonde network, found errors in the range $1.7\text{-}2.3\mathrm{ms}^{-1}$ for "ideal" radiosondes (which were considered to remain vertically above the point of release), and a grid resolution of 150km. The results of both the above studies support our assertion that the characteristics of LP and MRF spectra result in a tendency to over estimate the error. However, to err on the cautious side is considered preferable for the purposes of an OSSE - since it is clearly desirable to avoid the over optimistic results that may result from under specification of the observation errors.

The advantage of the spectral analysis method is that it can be easily applied to any grid resolution and, having established that the method should give errors which are on the "safe" side, a similar analysis to that described above was repeated assuming a horizontal grid resolution of 100km (the nominal resolution of the nature run). The contributions to the unresolved variances are summarised in table 4.1 (rows 1&2) and give σ_h in the range 1.7 - 2.4ms^{-1} where the upper values refers to the level of the jet stream.

In further analysis of the MRF data combined spectra were produced for sectors with mean wind speeds in the range <30ms^{-1}, 30-40ms^{-1}, 40-50ms^{-1} and 50-60ms^{-1}. Comparison of all four spectra showed very similar amplitudes and slopes, suggesting there was no basis for modulating the representativeness error according to the mean wind speed on scales of ~500km.

The wind spectra discussed above, and the derived representativeness errors, pertain to mid-latitude wind regimes, and we therefore need to assess their applicability in tropical regions. Nastrom and Gage (1985) have performed a comparison of spectra over a range of latitude bands and found spectral slopes to be independent of latitude, whilst spectral amplitudes were found to be lowest in the tropics and highest in mid-latitudes. The horizontal representativeness errors quoted above will therefore tend to overestimate the error in tropical regions. However, for the reasons stated previously it is considered preferable to err on the cautious side, and for this reason we propose that the errors derived from mid-latitude datasets be used at all latitudes. Moreover, although, in principle, it would be possible to take account of latitudinal variations, to do so would be inconsistent with the specification of errors for the currently deployed components of the observing system - which will follow those used in operational analysis schemes - and which do not generally include latitudinal variations in error for a given observation type.

	170km grids		100km grids	
	average	jet	average	jet
Unresolved variance 2-4 grid lengths	1.96	1.96	0.53	0.53
Unresolved variance below 2 grid lengths	3.95	12.7 (8.75+3.95)	2.37	5.07
Unresolved vertical variance *	0.25	0.75 (3*0.25)	0.25	0.5 (2*0.25)
Vertical velocity aliasing	0.04	0.04	0.04	0.04
Instrument error	1.0	1.0	1.0	1.0
Total error variance (σ^2)	7.2	16.45	4.19	7.14
Observation error (σ)	2.7	4.1	2.0	2.7

Table 4.1 Summary of contributions to "background" observation errors in lidar wind observations. An instrument error of 1ms^{-1} has been assumed.

* For the "jet" case the vertical variance has been scaled by the ratio of the horizontal variances in the "jet" and "average" cases, i.e. 12.7/3.95 ~ 3.

4.2.2 Vertical representativeness errors

The vertical resolution of the lidar shots is likely to be of order 500m, similar to the vertical resolution of nature run, and the representativeness error arising from vertical variability in the wind field might therefore be expected to be small. However, as discussed below, vertical structure in the aerosol distribution will tend to enhance the vertical representativeness error. Campaigns to investigate backscatter characteristics have found that the backscatter coefficient is prone to vary by several orders of magnitude over a few 10s of meters (as a result of aerosol stratification). An example, reproduced from Vaughan *et. al.* (1987) is shown in figure 4.2 which shows a plot of backscatter (at 10μm) against height. Very strong backscatter was observed near 6km and 8km while near 8.5km the backscatter dropped to the minimum detectable. The example illustrates how the lidar return from a single

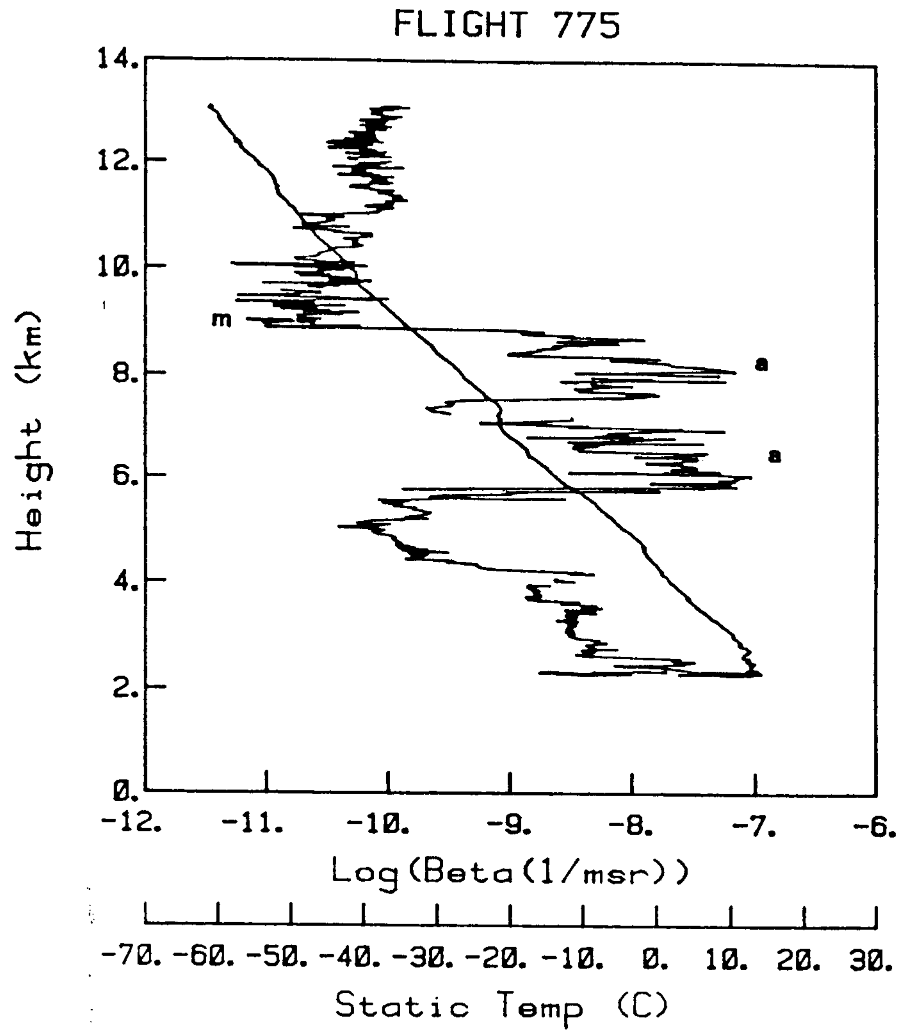

Figure 4.2: Vertical profiles of backscatter (Beta) at 10μm and temperature (from an example in Vaughan *et.al.*, 1987). Note the very strong backscatter at levels marked "a" and minimum detectable at level "m".

shot may be overwhelmed by backscatter from a thin horizontal slab within the target volume. In such cases the effective vertical resolution of the lidar data may be reduced to a scale much smaller than the vertical resolution of the NWP model.

To estimate the vertical representativeness error we refer to the work of Endlich *et. al.* (1969), who performed a spectral analysis of vertical profiles of the horizontal wind speed. The vertical profiles were obtained by radar tracking of rising balloons, and were processed to yield 50m layer averages at height intervals of 25m. Figure 4.3 shows spectra obtained for three different cases characterised by strong (April case), medium (November case) and light (July case) winds. Each spectrum shown in figure 4.3

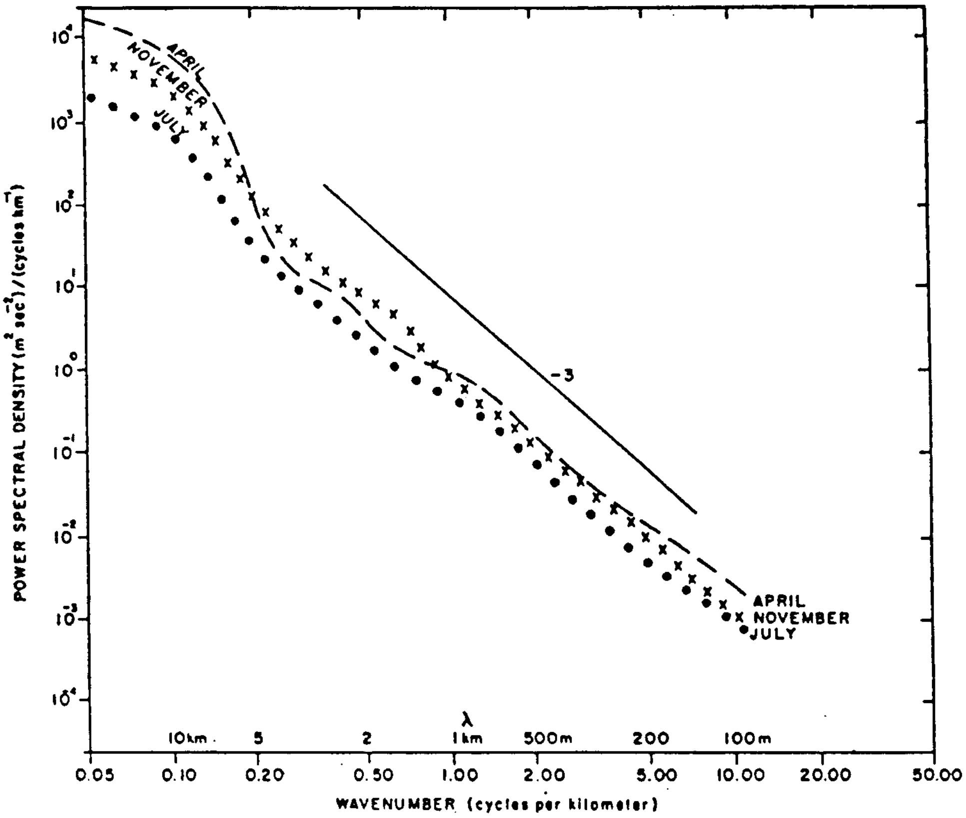

Figure 4.3: Spectra derived from vertical profiles of the horizontal wind by Endlich *et.al.* (1969). The April, November and July spectra correspond to wind profiles classified as "strong", "medium" and "light", respectively.

represents a graphical average of individual spectra obtained from several profiles measured at 1-2hr intervals. All three spectra show a slope of ~-2.8 for vertical wavelengths shorter than 1km. Slightly greater amplitudes are evident in the strong wind case. Spectra for separate zonal and meridional components were also obtained and found to be similar to the combined speed, except for long wavelengths which exhibited more energy in the zonal component due to the westerly character of the flow in each case. Assuming a -2.8 power law, we can integrate the spectrum and determine the representativeness error associated with a given vertical grid resolution (assuming "pin point" vertical resolution of the lidar shots). The result is shown in table 4.2, which shows the vertical representativeness error (σ_m) as a function vertical grid resolution. Since, in practice, aerosol stratification will not contaminate all shots, the values in table 4.2 should be overestimates, and for this reason we propose a value of $\sigma_m = 0.5 \mathrm{ms}^{-1}$, somewhat smaller than that indicated in table 4.2, for grids with vertical spacing of ~500m. To obtain a value for σ_m appropriate for the jet stream level we assume that the vertical error variance increases in the same proportion as the horizontal error variance (i.e. by about a factor of 3, for grids of ~170km). The resulting values are summarised in table 4.1 (row 3).

Vert. grid resolution	Vert. rep. error (ms^{-1})
500m	0.8
250m	0.4
200m	0.2
100m	0.1

Table 4.2 "Background" vertical representativeness errors for different vertical grid resolutions derived from spectra published by Endlich *et.al.* (1969).

4.2.3 Vertical velocity "aliasing"

The contribution from vertical velocity aliasing will be most important in localised regions where the vertical velocity is large, and specific meteorological situations which may give rise to large vertical velocities are considered in section 4.5. In this subsection we specify the small contribution to errors of this type which will arise from "background" structure in the vertical velocity field. Ecklund *et.al.* (1986) have presented vertical velocity spectra derived from Döppler radar measurements at Poker Flat, Alaska; Platteville, Colorado; Rhone Delta, France and at Ponape in the central Equatorial Pacific. They produced spectra for "quiet" and "active" periods by separating the data into periods when the wind speed throughout the troposphere was less than or greater than $10\mathrm{ms}^{-1}$. The quiet-time spectra, reproduced in figure 4.4, show similar characteristics for all datasets. The spectra are flat over the range of periods greater than the Brunt-Vaisala (B-V) period (10mins), with a rapid decrease in amplitude occurring at periods less than the B-V period. A peak in the spectra at periods slightly longer than the B-V period is typical. By integrating the spectra, Ecklund *et.al* estimate the "background" variance of the vertical wind to lie in the range

50 - 200cm^{2}s^{-2} (0.07 - 0.14ms^{-1}, rms), which is in accord with measurements made by Roll (1965). For comparison with the results of Ecklund *et.al.*, which pertain to conditions over rough terrain, a vertical velocity spectrum was produced for the MRF dataset - which pertains to conditions in jet streams over the Atlantic. The spectral slope and amplitude of the MRF vertical velocity spectrum were found to lie between those for quiet-time and active-time spectra found by Ecklund *et.al.* (Ecklund *et.al* show that the active-time spectra, like the horizontal wind spectra, exhibit a slope of -5/3). Integration of the MRF spectrum gives a total vertical wind variance of 0.05m^{2}s^{-2} (0.22ms^{-1} rms). Considering both the results of Ecklund *et.al.* and those obtained with the MRF dataset, a value of σ_w = 0.2ms^{-1} would seem a reasonable estimate for the background contribution from vertical velocity aliasing.

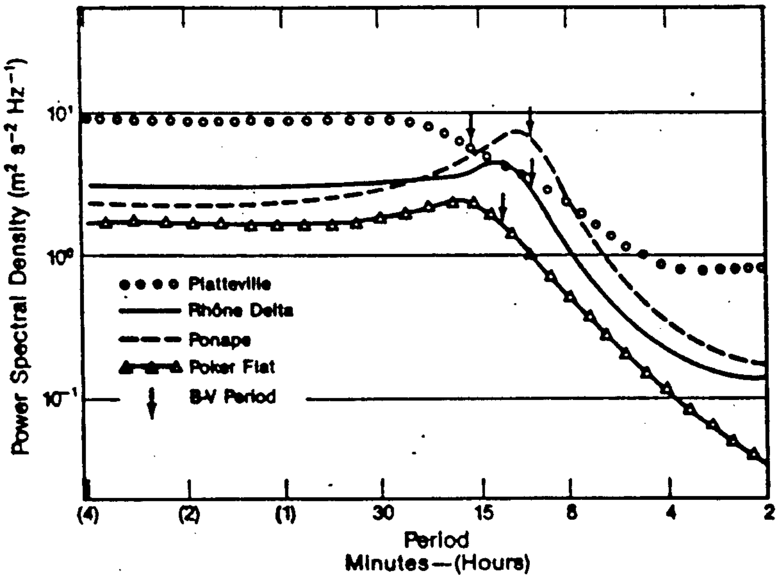

Figure 4.4: Intercomparison of quiet-time vertical velocity spectra observed at Poker Flat, Alsaka; Plateville, Colorado; Rhone Delta, France, and Ponape , central Equatorial Pacific (from Ecklund *et.al.*, 1986).

4.2.4 Summary

In the above we have attempted to specify "background" values of the representativeness error for Döppler lidar winds, contributions arising from the finite horizontal and vertical resolution of the NWP grid and from vertical velocity aliasing have been considered. The results are summarised in table 4.1 with reference to NWP model horizontal grid resolutions of 170km and 100km and with a separate column showing errors appropriate for the jet stream level. Overall observation errors are also shown, assuming an instrument error of $1ms^{-1}$, and that all errors are independent. For grid lengths of 100km the observation errors for single component winds lie in the range 2 - $2.7ms^{-1}$, with errors of horizontal representation dominating the overall errors.

4.3 Local enhancement of the "background" representativeness error

The background representativeness error discussed above will underestimate the error in regions where small scale "roughness" in the wind field is above average - in the planetary boundary layer (PBL), for example. In this section, therefore, we give special consideration to the errors likely to be associated with specific meteorological situations characterised by above average wind variability. Errors from regions affected by the following meteorological phenomena will be considered,

a) Boundary layer flows
b) Clear air turbulence
c) Orographic gravity waves
d) Stratiform cloud tops
e) Convective cloud tops

We shall refer to statistics from existing observational studies and, in the case of (a) and (c) to case study simulations performed with the UK Met. Office mesoscale model.

4.3.1 Observational studies

Some published statistics on wind variability associated with the meteorological phenomena listed above are summarised in table 4.3, and give an idea of the likely error that will result in the lidar observations. Further details of the specific studies are given below.

	Standard deviations (ms^{-1})	Source
Convective PBLs	$\sigma_v = 1.26(\text{land});0.88(\text{ocean}) \simeq 1.$ $\sigma_w = 1.16(\text{land});0.6(\text{ocean}) \simeq 0.9$ Assuming isotropy, $\sigma_h \simeq 1/\sqrt{2} \simeq 0.7$	Hicks (1981); Minnesota and Coral Sea field experiments.
Stable PBLs	$\sigma_h \simeq 0.5$	Mesoscale model case study
C.A.T.	$\sigma_u = 3.8$; $\sigma_v = 3.3$; $\sigma_w = 2.5$ Assuming isotropy, $\sigma_h \simeq 3.2/\sqrt{2} \simeq 2.3$	Kennedy and Shapiro (1980)
Orographic gravity waves	$\sigma_w =$ 1-2 (UK) 2-3.5 (Rockies)	UK - Brown (1983) Mes. model studies Rockies - Vergeiner and Lilly (1970)
Stratiform cloud tops	$\sigma_{u,v} = 0.3$; $\sigma_w = 0.4$ Assuming isotropy, $\sigma_h \simeq 0.35/\sqrt{2} \simeq 0.2$	Nicholls (1984)
Convective cloud tops	$w_{max} = 25$ represent with log-normal distribution	Lopez (1977) LeMone and Zipser (1980) Roach (1967)

Table 4.3 Summary of error standard deviations, appropriate for various meteorological conditions, for use in simulating lidar data.

a) Boundary layer turbulence.

Turbulent fluctuations in the convective PBL have a coherent structure on a scale which is comparable to that of the lidar shots. Lidar returns from the boundary layer will therefore reflect the turbulent motion, and appropriate representativeness errors should be included in the simulated data. Turbulent motions in the stable boundary layer are generally of smaller scale and amplitude (with the exception of shear driven mechanical turbulence, important in strong wind conditions), and will have less impact on the larger scale representativeness of the lidar winds. Turbulence statistics for the convective PBL, taken from Hicks (1985), are shown in table 4.3 and refer to studies of the convective planetary boundary layer (PBL) in a Minnesota field experiment (Izumi and Caughey, 1976) and over the Coral Sea (Warner, 1972,1973). Standard deviations for the transverse and vertical turbulent velocity components are shown - σ_v and σ_w respectively. Data at heights between 0.1Z and 0.9Z were used where Z is the height of the mixed layer. For the Minnesota data values of σ_v=1.26ms^{-1}, σ_w=0.88ms^{-1} were found; slightly lower values were found for the tropical ocean dataset. If we assume, for simplicity, that the turbulent fluctuations are isotropic with a standard deviation of ~1ms^{-1} then, for the line of sight (LOS), $\sigma_{LOS} = \sigma_v = \sigma_w \simeq$ 1.0ms^{-1}. Horizontal single-shot lidar winds in such regions are likely to possess corresponding errors i.e. $\sigma_h = \sigma_{LOS}/\sqrt{2} \simeq$ 0.7ms^{-1} (assuming a scan angle of 45^0).

Errors arising from the mean structure of the PBL wind profile, rather than the turbulent fluctuations, are discussed in section 4.3.2.

b) Clear air turbulence.

Kennedy and Shapiro (1980) have made measurements of wind variance associated with a zone of moderate to severe clear air turbulence (CAT). The mean standard deviations found on two passes through the zone at 407mb and 358mb are given in table 4.3 (the direction of the u-component being defined along the principle component of the flow). Approximating the turbulence with isotropic fluctuations of standard deviation 3.5ms^{-1} suggests an rms error in observations of the horizontal wind of order $\sigma_h = 3.5/\sqrt{2} \simeq$ 2.5ms^{-1}.

Algorithms are available for predicting the occurrence and intensity of CAT from NWP model fields and could be used to modulate the rms errors. Dutton (1980), for example, has described a simple empirical index defined by a linear combination of the horizontal wind shear and the square of the vertical wind shear. However, the algorithms are generally tuned for aviation safety purposes and tend to over predict the occurrence of CAT. Some tuning of the algorithms, and adaptation to work with the NWP model used to generate the nature-run, would therefore be a necessary preliminary step.

c) Orographic gravity waves

Brown (1983), has analysed vertical velocity measurements associated with gravity waves measuredduring five separate research flights over the U.K.. His results suggest that vertical velocity aliasing errors of σ_w= 1-2ms^{-1} will be typical in gravity wave activity associated with orography on the scale of that in the U.K.. Vergeiner and Lilly (1970) have published a large number of vertical velocity measurements made in gravity waves over the Rockies. They note that wave amplitudes were typically in the range 3-5ms^{-1} which, if we assume that the waves are sinusoidal, may be interpreted as corresponding to rms vertical velocity in the range $\sigma_w = 2\text{-}3.5\text{ms}^{-1}$. The above figures suggest the probable range of errors associated with orographic waves. The actual error at a given location will depend on details of the terrain and the flow type, and it may be possible to simulate some of the structure in the errors by modulating the errors, within the range 0-3.5ms^{-1} (rms), according to the intensity of gravity wave activity as specified by output from the gravity wave drag scheme in the nature run (see Courtier *et.al.*, 1992). This strategy would provide a means of modelling the errors from weakly trapped waves which dissipate quickly on the downstream side of the mountain, but would not address errors resulting from trapped lee waves - which may propagate for large distances (~1000km) downstream. Simulation of errors from the weakly trapped waves is probably more important, however, since these waves propagate vertically and can disturb the local flow over the entire troposphere. Moreover the cases discussed by Brown (1983) indicate that the weakly trapped waves frequently correspond with those of largest amplitude (largest aliasing errors). Use of the gravity wave drag scheme to modulate the errors should, therefore, enable simulation of the errors associated with orographic waves in the regions where such errors are likely to be most significant.

To complement the observational studies mentioned above, a number of 3-D simulations of orographic gravity waves, using the UK Met. Office meso-scale model, are presented in section 4.3.2.

d) Returns from stratiform cloud tops

Returns from cloud tops will sample the small scale turbulent motion of the cloud particles, plus any bulk motion of the cloud particles in the cloud system, in addition to the large-scale flow. Nicholls (1984) has presented measurements of the variance of the turbulent wind components in daytime stratocumulus over the North Sea. For the purposes of specifying typical errors these measurements are probably reasonably representative of other stratiform cloud types. Values of $\sigma_w^2 \simeq 0.15\text{m}^2\text{s}^{-2}$ were found near the cloud top and dropped rapidly to $\sigma_w^2 \simeq 0.05\text{m}^2\text{s}^{-2}$ above cloud top. Variance for each of the horizontal components was found to be similar at $\sigma_u^2 = \sigma_v^2 \simeq 0.1\text{m}^2\text{s}^{-2}$. Assuming, once again, that the fluctuations may be approximated by isotropic turbulence, the rms error in the horizontal wind arising from turbulence at stratiform cloud top may be estimated as $0.35/\sqrt{2} \sim 0.2\text{ms}^{-1}$.

d) Returns from convective cloud tops

Shots striking convective cloud tops will sample the bulk upward motion of cloud particles in convective turrets, and vertical velocity aliasing errors will be important in these cases. Shots striking the cloud walls will, presumably, also sample upward velocity although of lesser magnitude. Descending particles will only rarely be encountered (in rain, for example) since in dissipating convective turrets, the particles are evaporating rather than descending.

As a simplification to the problem we therefore seek a distribution which will describe the growth rate of convective cloud tops in a population of cumulus clouds. The vertical velocity contamination may then be simulated by first deciding whether the shot strikes a cumulus top - an eventuality which may be expressed as a simple function of the convective cloud cover (i.e. for 3/4 cover, 3 out of 4 shots will strike a cumulus top). Secondly, for those shots which strike cloud the vertical velocity contamination is determined by the distribution describing the growth rate of the cloud tops.

Lopez (1977) has shown that cloud height in both tropical and extratropical cumulus populations closely follows a log-normal distribution, and it would seem reasonable to assume that the growth rate of convective turrets follows a similar distribution. In a study of convective storm tops in Oklahoma, Roach (1967) observed that the growth rate of convective turrets, could reach 25ms^{-1} in exceptional cases; a log-normal distribution with a tail allowing a small probability of cloud top growth rates of 25ms^{-1} might therefore provide a reasonable simulation of the distribution of cloud top vertical velocities. Cumulative probabilities based on a log-normal distribution defined by,

$$f(x) = \frac{1}{\sqrt{2\pi}\, sx} \exp\left(-\frac{1}{2s^2}\left(\ln(x/x_0)\right)^2\right), \qquad (4.2)$$

are shown in figure 4.5. The parameters s and x_0 are set at s= 1.0 and x_0= 1.7 respectively, which gives a probability of cloud top velocities greater than 20ms^{-1} of 0.004. A one-tailed Gaussian distribution with a zero mean and an rms of 7ms^{-1} (which produces as similar probability of cloud top vertical velocities of 20ms^{-1}) is shown for comparison. For the lognormal distribution

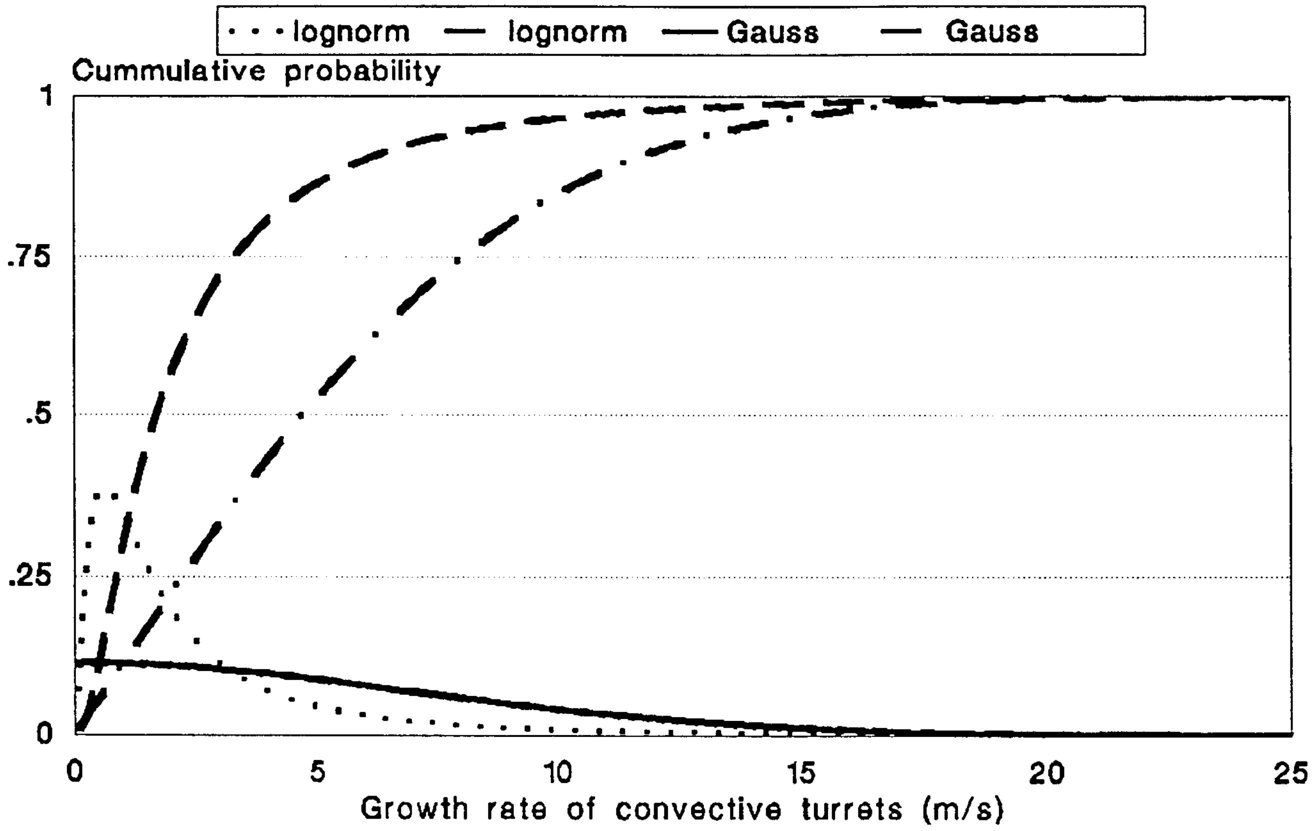

Figure 4.5: Growth rate of convective turrets as modelled assuming log-normal and Gaussian distributions, and specifying (arbitrarily) that the probability of a growth rate in excess of $20 ms^{-1}$ should be ~0.004. The log-normal distribution is shown in dotted line and the Gaussian in solid line. The cumulative probability of growth rates below a given abssisca value are shown for the log-normal distribution (dashed) and the Gaussian (dash-dot).

15% of all shots striking cloud top would have errors greater than $5ms^{-1}$, and 5% would have errors greater than $10ms^{-1}$. In contrast, use of the Gaussian distribution would imply that 50% of shots striking cloud top would have errors of more than $5ms^{-1}$ and 15% would have errors greater than $10ms^{-1}$. This suggests that use of a Gaussian distribution to simulate vertical velocity aliasing errors in returns from convective cloud tops would seriously over estimate the errors.

4.3.2 Studies with the UK mesoscale model

a) Unrepresentative sampling of the mean boundary layer wind profile

Vertical wind shear and marked inhomogeneities in aerosol distribution are relatively common features of the PBL, and will contribute to representativeness errors in winds from this level. Consider, for example, a region in which the aerosol is concentrated in the surface layers and a typical boundary layer wind profile exists - i.e. decreasing speed and backing direction with decreasing height. The lidar shots will sample the low-speed, aerosol rich regions and consequently will show a bias with respect to the mean boundary layer wind: the bias in wind speed will be negative, and the bias in direction will reflect a measured wind direction consistently backed from the true direction.

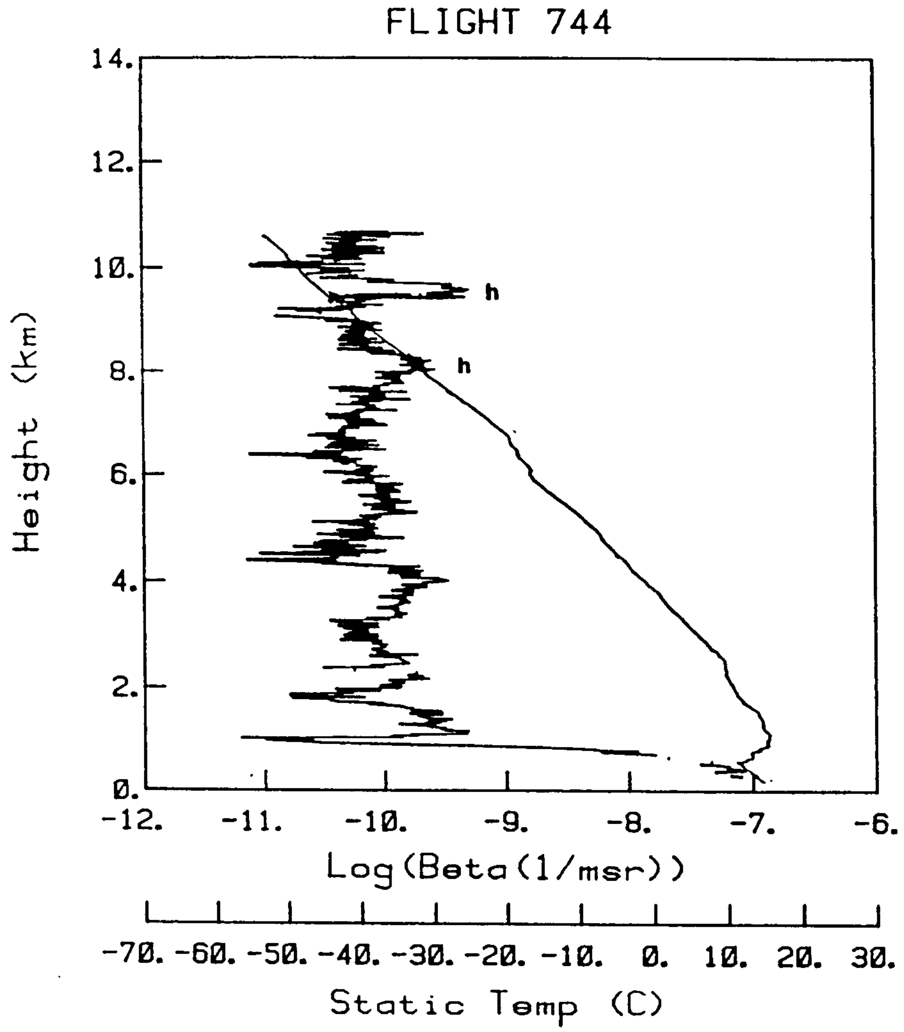

Figure 4.6: Example vertical profiles of backscatter at 10μm (Beta) and temperature (from Vaughan *et.al.*, 1987). Note strong backscatter below the low-level temperature inversion, decreasing rapidly by 3 orders of magnitude above the inversion.

It is well known that low-level temperature inversions can lead to marked discontinuities in the vertical distribution of aerosol. An example of this effect (taken from Vaughan *et.al.*, 1987) is illustrated in Fig.4.6. The temperature trace (on the right) shows a marked temperature inversion with a base at about 600m; backscatter below the inversion is about 3 orders of magnitude greater than above the inversion, with the transition occuring across a layer about 250m deep.

To investigate the errors associated with unrepresentative sampling of the PBL wind profile, the following experiment has been performed using output fields from the UK mesoscale model (Golding 1987, 1990). Shots were considered to be located at all the model grid points, and only low level shots, which for convenience were assumed to sample the vertical interval 5-480m (which represents model levels 3-12), were considered. The shots were assumed to have a vertical scale equal to the above interval (475m). The model fields were checked for increasing temperature with height equal to 1K/500m over a depth of 50m or more. When such an inversion was found, aerosol trapping was assumed to occur at that grid point, and the wind perceived by the lidar shot was assigned as equal to the mean wind in the sub-inversion layer (i.e., it was assumed that returns from the aerosol rich part of the target volume below the inversion overwhelm those from above the inversion). The error in the perceived horizontal wind was defined as $V_e = V_s - V_m$, where V_m is the mean velocity over the full layer (5-480m) and V_s is the mean velocity over the sub-inversion layer. Since the depth 5-480m is similar to the resolution of the nature run, the error may be interpreted as a representativeness error.

Figures 4.7 and 4.8 show results from a case study using analysis fields valid for 00GMT 9 Feb 1991. Figure 4.7 depicts the mean wind over the 5-480m layer (V_m) and shows a weak cyclonic circulation situated over the Channel, with a NE'ly flow present across much of the U.K. The wind errors, V_e, are shown in figure 4.8; regions where $|V_e| > 2ms^{-1}$ have been shaded. The tendency for the perceived wind vector to be too weak in magnitude and to be oriented to the left of the actual flow is evident. The appearance of the error vectors suggests that the cyclonic vorticity of the flow is under estimated and the convergence in the flow is over estimated. Note that, for the simple model described here, the error is zero over the sea, where low-level temperature inversions of the required strength were not present in the model fields. In practice, although low-level temperature inversions are less common over the sea, unrepresentative sampling of the boundary layer wind profile is still

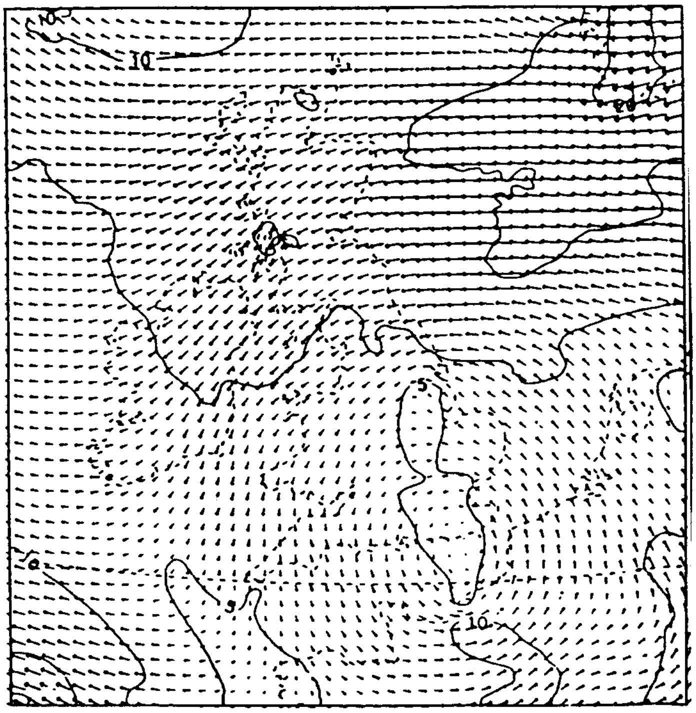

Figure 4.7: Mean wind over the layer 5-480m (V_m) obtained from the mesoscale model analysis field valid at 00GMT 8 Feb.1991. Solid lines are isotachs at intervals of $5ms^{-1}$.

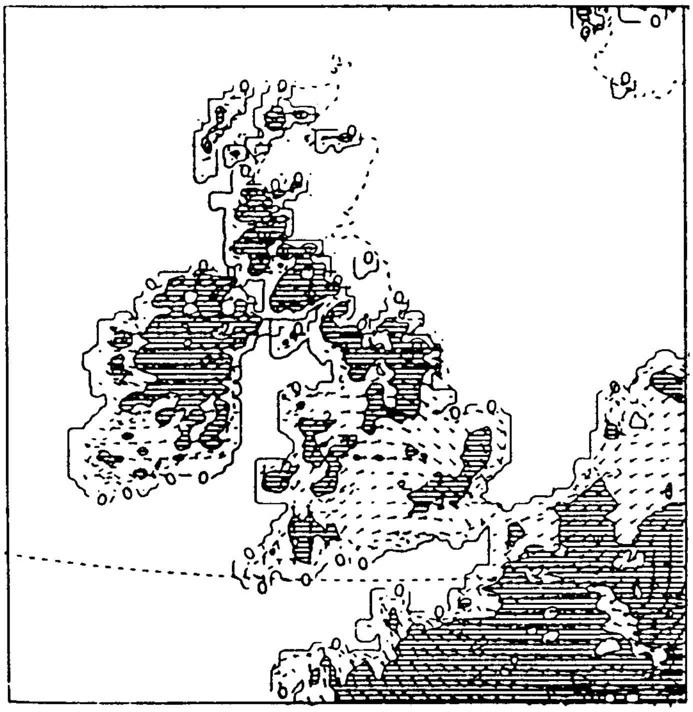

Figure 4.8: Difference (Ve) between the mean wind speed below the inversion and the mean wind speed in the 5-480m layer (Vm). Regions where $|V_e| > 2ms^{-1}$ have been shaded. The magnitude of the wind vectors has been multiplied by a factor of five compared with those in figure 4.7. Isotachs are shown in $2ms^{-1}$ intervals. Note the confluent pattern in V_e over northern France and southern England.

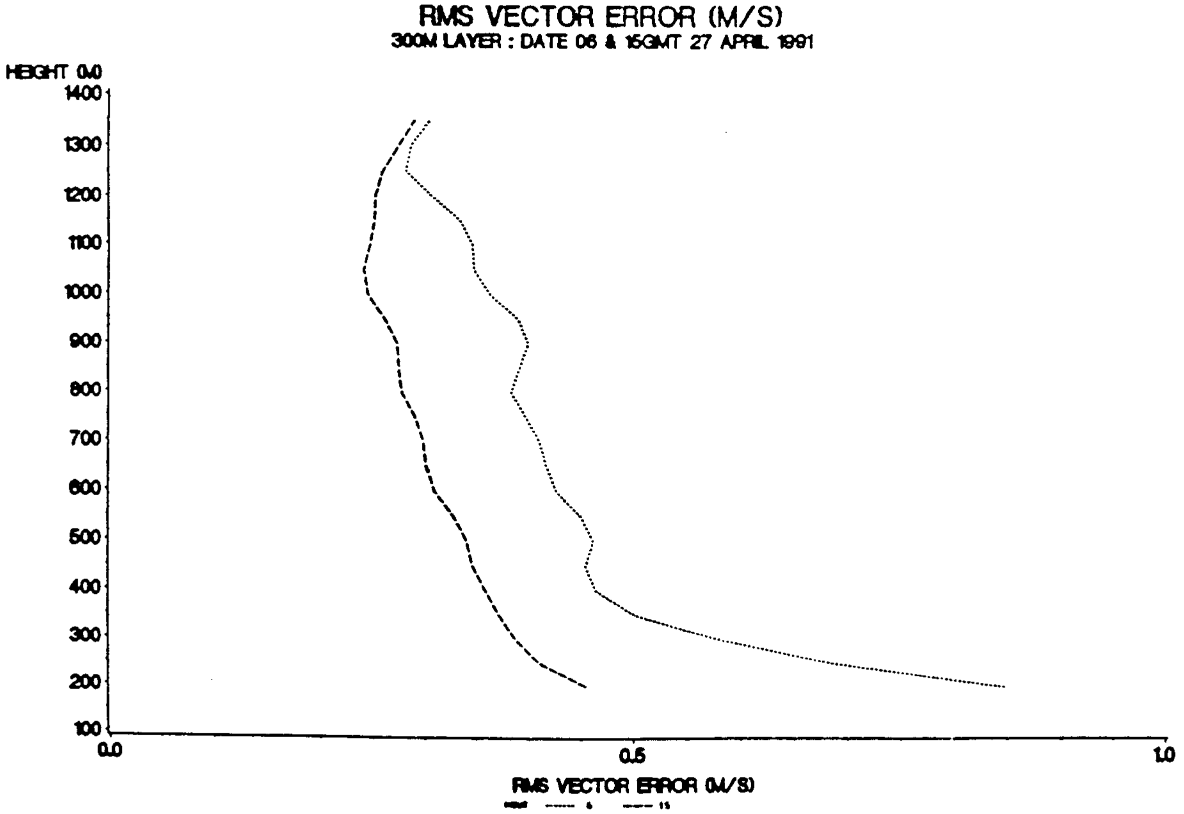

Figure 4.9: Vertical profile of the rms vector difference between the mean wind over 300m interval and the mean wind over the lower half that interval, from mesoscale model analysis fields valid at 06GMT (dotted) and 15GMT (dashed) 27 April 1991.

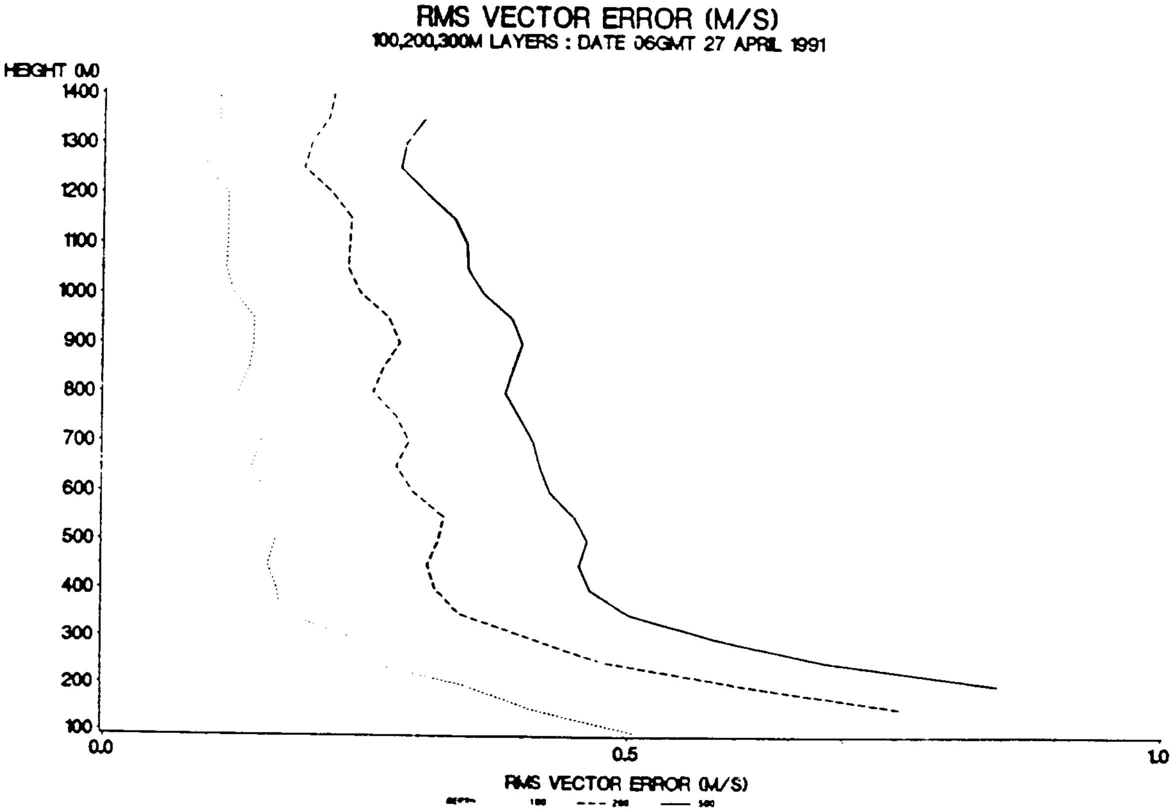

Figure 4.10: As figure 4.9, but for the 06GMT field only and showing the profiles obtained with vertical intervals of 100m (dotted), 200m (dashed) an d 300m (solid).

likely to occur (high levels of near surface aerosol in the form of sea-spray might give rise to similar effects, for example).

To assess the potential for errors at higher levels in the boundary layer, additional experiments have been performed in which it was assumed, for simplicity, that for all shots the target depth is exactly bisected by a discontinuity in aerosol concentration. The rms vector differences between the wind in the lower half of the shot depth and that over the full shot depth give a measure of the potential error from this source at a given level. Fig.4.9 shows results from a case study using analysis fields valid at 06GMT and 15GMT 27 April 1991. The case was chosen because of the presence of temperature inversions on the morning of that day which were "warmed out" during the afternoon. Errors are shown for 06GMT, when nocturnal inversions would have been near maximum strength, and at 15GMT when the boundary layer should have been well mixed. The vertical scale of each shot is assumed to be 300m. At both times rms errors of 0.3 - 0.5ms^{-1} are present above 300m - with slightly larger values in the 06GMT field - and show, in general, a decreasing trend with height. For the 06GMT case there is a rapid increase in the rms error below 300m to around 0.9ms^{-1} near 200m. The effect of reducing the vertical resolution of the shot is shown in figure 4.10, which shows rms errors for the same case at 06GMT for resolutions of 100m, 200m, and 300m. The difference is most marked below 300m where the error reduction from increasing the resolution is almost twice that above 500m.

The experiments described above illustrate that in the presence of backscatter discontinuities, "near surface" returns are likely to possess negative biases in wind speed, and directions which are backed from the actual wind direction. Errors are likely to be largest in "near surface" shots, and for stable boundary layers where the absence of mixing can result in the maintenance of strong vertical shear.

b) Vertical velocity aliasing in orographic waves

A research version of the operational mesoscale model, with 3km horizontal resolution, has been proved capable of simulating certain classes of long orographic lee waves with some accuracy. An example of the success of the model (Shutts, 1990) is given in figure 4.11, which shows results of an evaluation of model performance for a case study of lee wave activity over the Welsh mountains. The continuous line shows the actual vertical velocity as measured by the ascent rate of a sonde balloon, and the crosses show the vertical velocity predicted by the model along the trajectory of the balloon. A close correspondence in both the amplitude and phase of the simulated and actual vertical velocity is clear. In the following we take advantage of the success of the model in simulating this case of lee wave activity to probe the magnitude, vertical structure and dependence on orographic height of the vertical velocity aliasing errors associated with orographic waves.

Figure 4.12 shows the rms vertical velocity (or rms aliasing error) as a function of height derived from a model simulation of the case described above (06 October 1989). Results of three runs are shown; run "A" is for the standard model orography (the model uses smoothed orography with a peak height of 741m corresponding to Mt. Snowdon (actual height, 1085m). Runs B and C are for elevated orography; B = 2 × standard, C = 2.5 × standard. The rms error is calculated for all points in which the orographic height is greater than 200m. All three runs show rms errors of $\sim 1\mathrm{ms}^{-1}$ or more extending over the entire depth of the troposphere. The shape of the profile is probably typical for deeply propagating, weakly trapped waves. The profiles are fairly constant with height in the troposphere and give approximate rms errors of $1\mathrm{ms}^{-1}$, $1.6\mathrm{ms}^{-1}$ and $1.8\mathrm{ms}^{-1}$ for runs A,B and C respectively; the magnitude of the errors decreases rapidly between 12-14km. A frequency histogram of vertical velocity, for the layer 5-10km is shown in figure 4.13 for run C. The expected frequencies from a Gaussian distribution with the same rms vertical velocity are shown for comparison. The Gaussian is seen to underestimate the frequency at the peaks and tails and to overestimate the middle ranges. However, for the purposes of simulating lidar data, the agreement is probably good enough to justify its use in modelling the errors associated with orographic gravity waves close to the source of the disturbance. Values of $\sigma_W = 1\text{-}2\mathrm{ms}^{-1}$, found with the model studies described above, are in agreement with those of Brown (1983) for orography of the stature of that in the U.K.

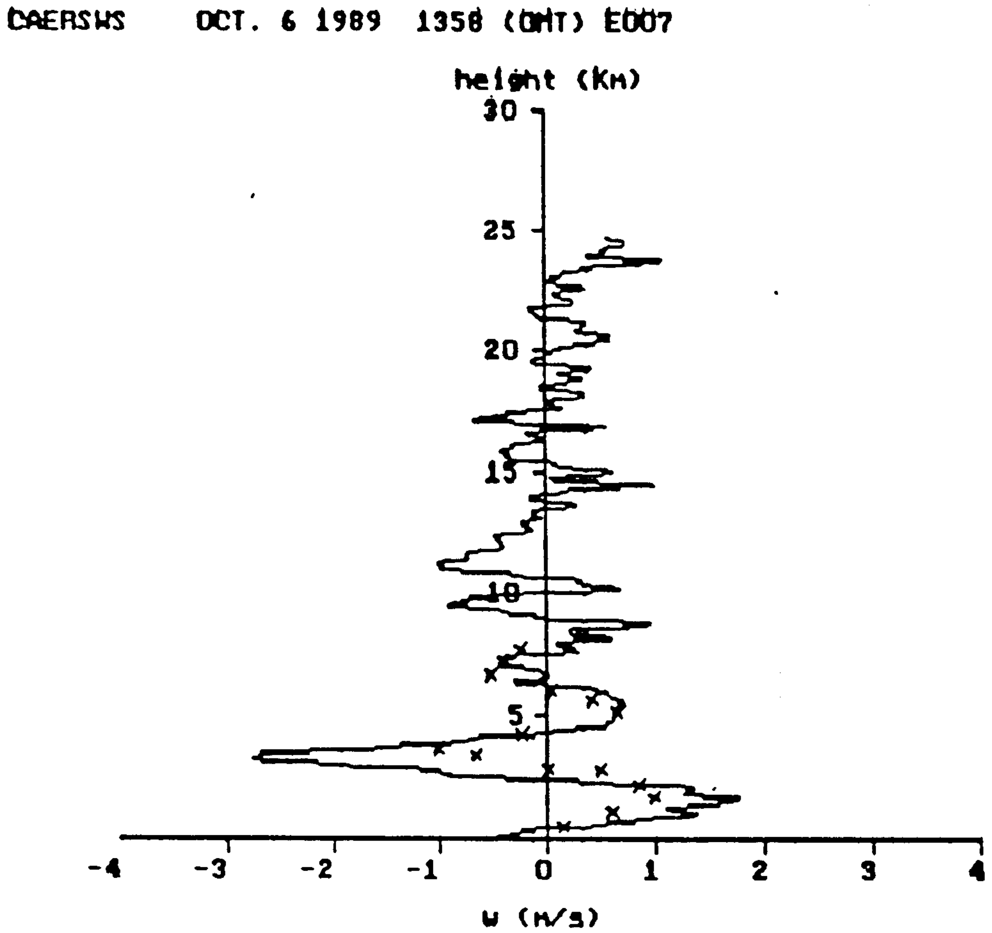

Figure 4.11: Verification of a simulation of lee wave flow over Wales, on 6 Oct 1989, by the high resolution (3km) version of the UK mesoscale model. The continuous lines shows the ascent rate of a radiosonde balloon released at a field site (an appropriate "still air" ascent rate has been subtracted) The crosses show the vertical velocity from the model simulation along the trajectory of the balloon. Note the excellent correspondance in both phase and amplitude. (From Shutts 1990).

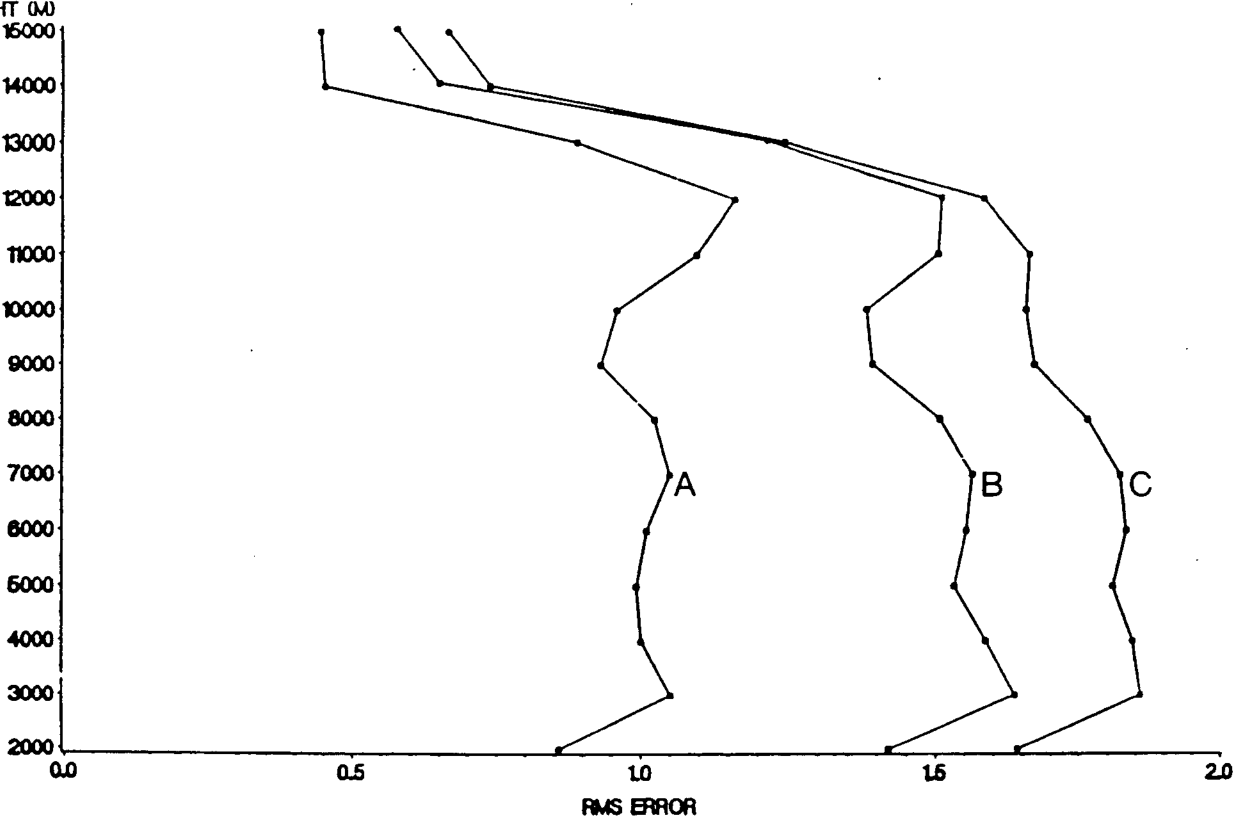

Figure 4.12: Vertical profiles of rms vertical velocity(i.e. aliasing error) from a model simulation of lee wave activity over Wales on 6 October 1989. Three profiles are shown: A - standard model orography;B - standard orography x 2; C - standard orography x 2.5. Only model grid points where orographic height > 200m are considered.

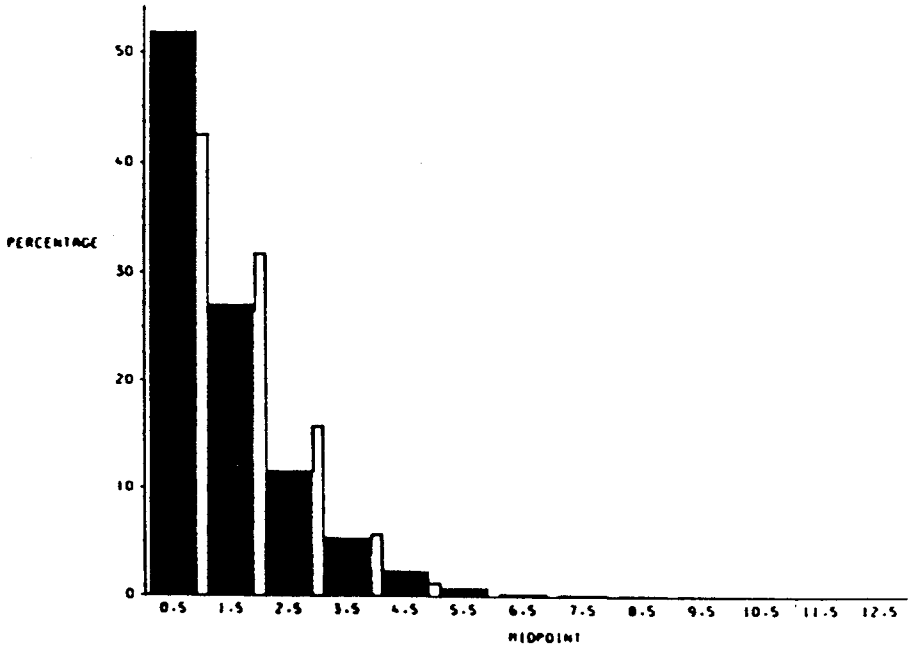

Figure 4.13: Histogram showing the frequency of vertical velocities of a given magnitude ($1ms^{-1}$ bins) for run "C" (figure 4.12) over the 5-10km layer (dark bars). The overall rms vertical velocity is $1.74ms^{-1}$ and the equivalent histogram for a Gaussian distribution of this rms is shown by the thin blank bars. Note that the Gaussian distribution underestimates the peak and tail of the actual distribution.

4.4 Summary

The conclusions of this section are best summarised by reference to table 4.4, which shows proposed lidar observation errors based on estimates of the representativeness errors, discussed in the preceding sub-sections, and assuming an instrument error of $1ms^{-1}$. The background representativeness errors discussed in section 4.2 have been modified slightly to give maximum errors at 250mb, and are in the range $2\text{-}3ms^{-1}$. The vertical distribution of the background errors has been based on that currently used for radiosondes in the UK. Met. Office Unified model (shown in column 3 for comparison). Examples of local enhancements to the background error, from the effects discussed above, are shown in column 2, and assume that the errors follow a Gaussian distribution and are independent. Orographic wave activity and CAT are seen to put a considerable increment on the rms background error values. A typical rms error of $2ms^{-1}$ has been assumed for both orographic and CAT effects. In practice these errors could be modulated according to output from the gravity wave drag scheme in the nature run and CAT prediction algorithms although, to ensure a reasonable distribution of errors, this would require some tuning and experimentation with the NWP run used to generate the nature run . The effects of convection are also likely to be significant, as reference to Fig.4.5 will confirm, however since it is proposed that errors associated with convection are modelled using a log-normal distribution these errors cannot be included in an overall rms figure. An rms error of $0.7ms^{-1}$ has been assumed to apply for all boundary layer types and covers the estimates given for convective PBLs and those found for the stable PBL in the model case study ($0.3 - 0.9ms^{-1}$). Errors from stratiform cloud tops make a negligible increment on the background errors and are not shown.

Pressure (mb)	background error (ms^{-1})	Orog/C.A.T (2.0)	Radiosonde errors (UK unified model)
1000	2.1	2.9	2.0
850	2.0	2.8	1.8
700	2.0	"	1.6
500	2.0	"	2.1
400	2.6	3.3	2.6
300	2.9	3.5	3.0
250	3.0	3.6	3.2
200	2.6	3.3	2.7
150	2.4	3.1	2.4
100	2.0	2.8	2.1
70	"	"	"
30	"	"	"
20	"	"	"
10	"	"	"

Table 4.4

Proposed observation errors for simulated Döppler lidar winds, assuming an instrument error of 1ms^{-1}. The error for the 1000mb level includes a background error of 2ms^{-1}, and a contribution of 0.7ms^{-1} rms from the effects of PBL turbulence. In column 2 a typical rms errors of 2ms^{-1} has been assumed to illustrate the likely increase in the rms observation error in regions of orographic wave activity or C.A.T. Column 3 shows observation errors currently assumed for radiosondes in the UK Met. Office Unified model analysis scheme.

5 Simulation Studies

In this section we use the analysis tools developed in sections 2 and 3 to assess various instrument scenarios.

5.1 OI studies of scan patterns

The minimum variance formulation of OI enables the analysis error covariance to be calculated using (2.4), without simulating observed values with random errors. As long as error distributions are Gaussian, the effect of observations on the analysis error, can be calculated directly.

Our first study follows on from section 2.1. What is the best way to distribute shots across the swath of a scanning instrument? A constant pulse rate will put more shots near the edge (figure 5.1), while a *cosine* shot management will distribute the shots more evenly on the ground (figure 5.2).

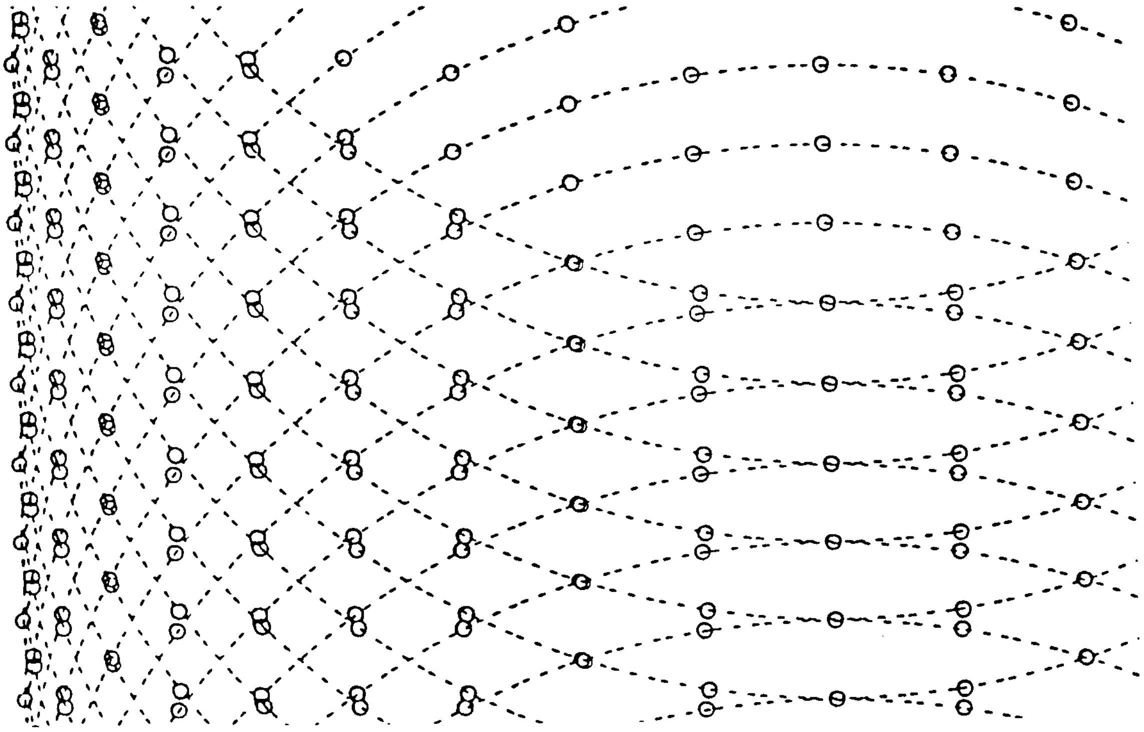

Figure 5.1. Portion of idealized distribution of shots from a conically scanning constant pulse-rate lidar. Observation positions are shown as O; the component radial to the scan tracks (dotted) is observed.

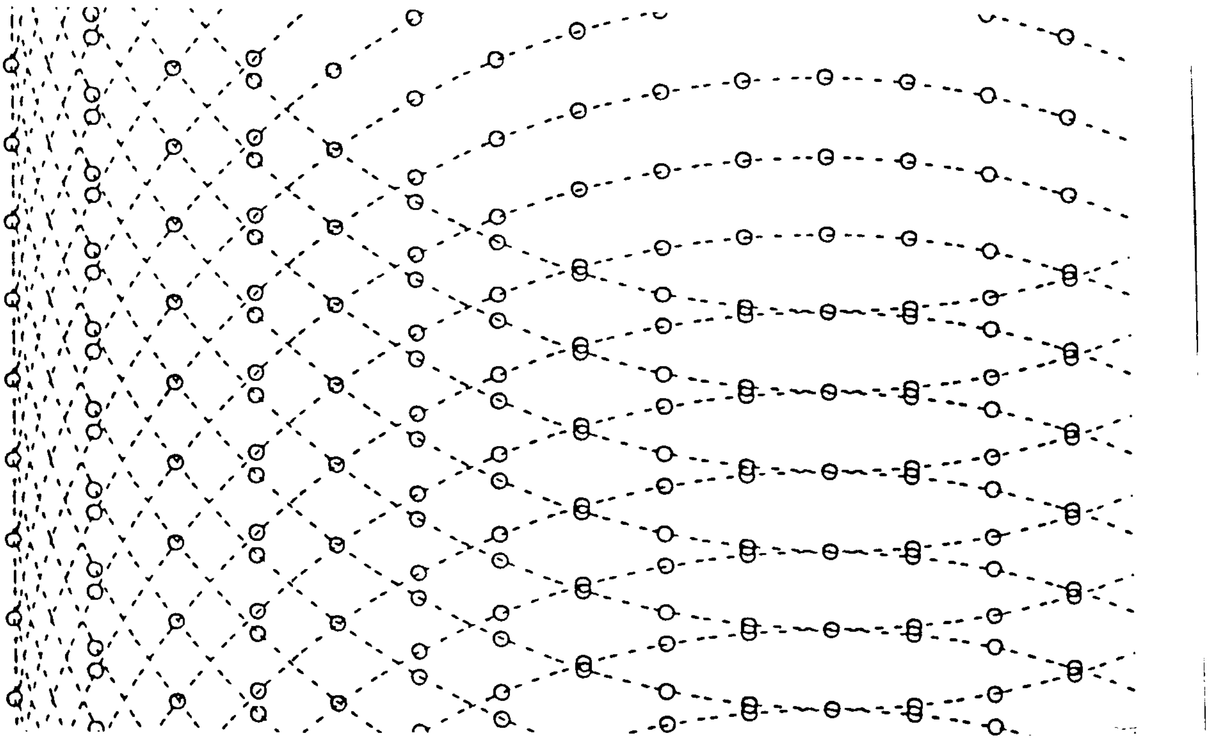

Figure 5.2. As figure 5.1 with *cosine* shot management, to give a constant density of shots on the ground.

The analysis error distributions for the along track and cross track wind components are shown in figure 5 .3 and figure 5.4. The solid lines were obtained using the "double TOAR" covariance function (2.7), while the thin lines used the Gaussian shaped function (2.5). The latter implies greater correlations, making more observations of use in decreasing the error at each point and improving extrapolation. But the qualitative results about shot management with the two functions were similar: The *cosine* shot management improves accuracy in the middle of the swath, but extrapolation from the edge is less accurate. Probably the optimal pattern is between the two. Underneath the satellite, a conical scan only observes the along-orbit component (figure 5.3). The cross orbit component (figure 5.4) has larger errors. Note however that OI interpolates information, so that this is much lower than the background error (5 ms^{-1}).

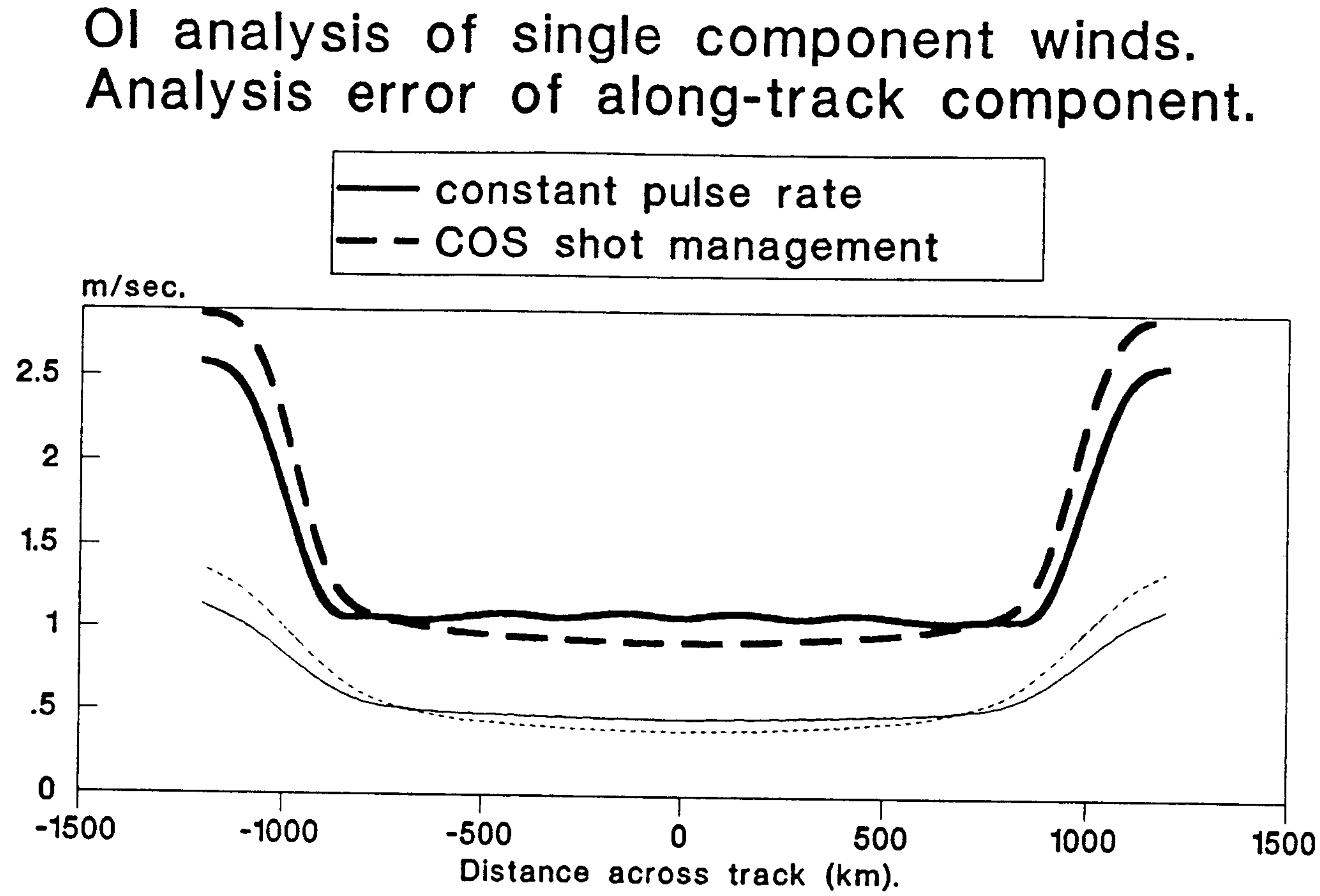

Figure 5.3. OI analysis errors in the along-track component, obtained using single component wind data from conical scan patterns shown in figures 5.1 and 5.2. Errors are plotted against distance from the centre of a 1500 km swath. The thick lines were obtained using a "double TOAR" covariance function, the thin lines using a Gaussian shaped function.

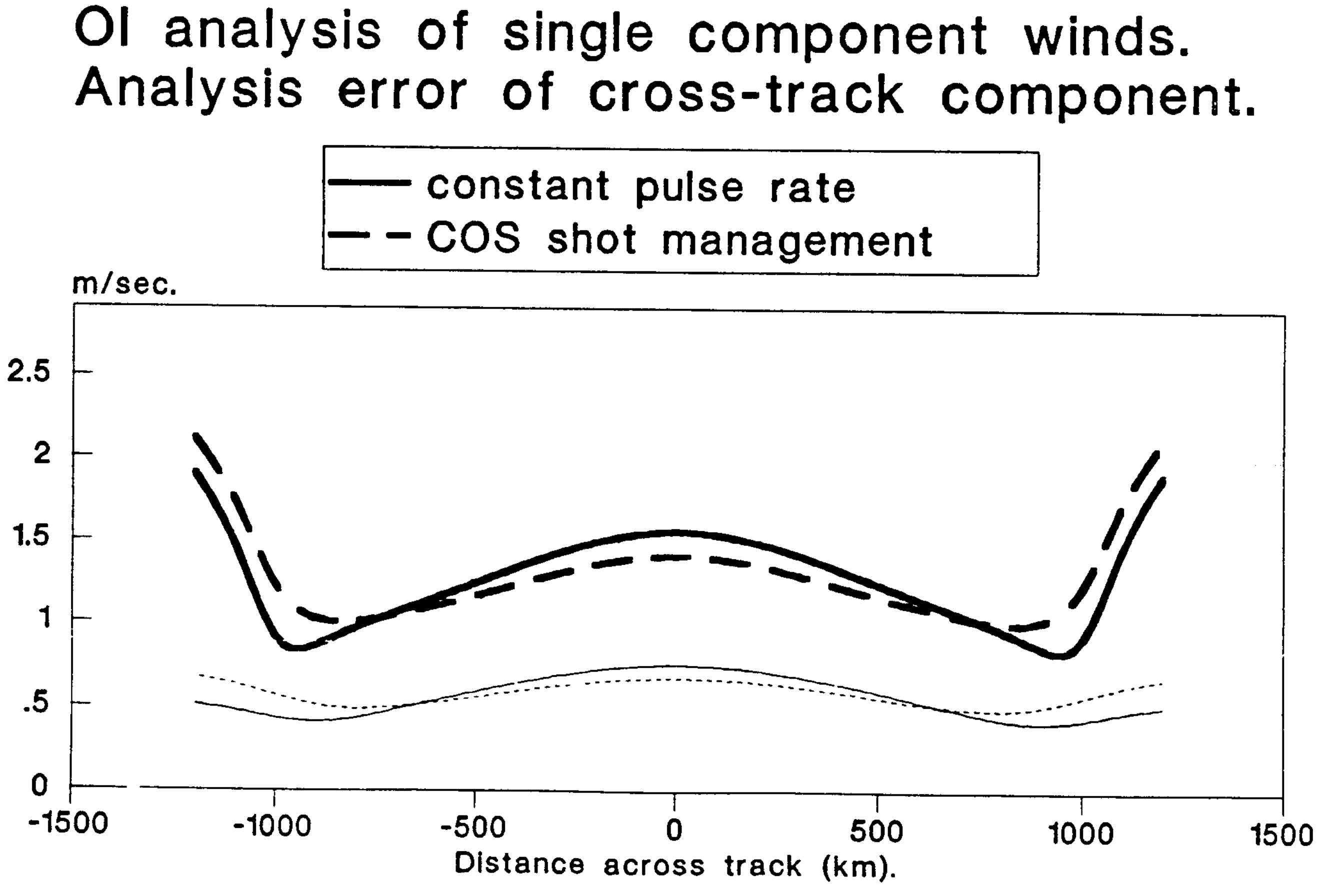

Figure 5.4. As figure 5.3 for the cross-track component.

5.2 Comparison of fixed and scanning instruments

Proposed LAWS and ALADIN instruments both have scanning lidar systems, like that considered above. A technologically less demanding alternative is to use fixed mirrors to produce four lines of shots: forward and backwards on each side of the satellite path. The forward and backward looks can be processed to give a line of vector winds on each side. A possible benefit of the 4-beam configuration is that shots are closer together, enabling better quality control of data from regions of poor signal-to-noise ratio. In order to assess this we used the nonlinear variational method of section 3.3, as well as the OI analysis error calculation. As expected, the variational method gave the same results as OI when P_g=0. A lower orbital height than in the previous tests, giving a narrower swath, was assumed. We simulated observations from a portion of an idealized satellite track, analysed them, and calculated the r.m.s. analysis error. Results from the two configurations were compared, with the same number of shots, with the same error characteristics, in each[1]. Background fields, with correlated, non-divergent, errors, were simulated and used in each analysis, using "double TOAR" background error covariances (2.7). The simulated errors for the background (r.m.s. 5 ms^{-1} in each component), and for good observations (r.m.s. 2.5 ms^{-1}), were Gaussian. The possibility of gross observational errors due to poor signal to noise ratio was allowed for by setting a proportion (Pg) of the observations to a number chosen at random between -25 ms^{-1} and +25 ms^{-1}. The experiments performed are listed in table 5.1.

All observations in a 1500x1500km box were included in the analysis. For a pulse rate of 2Hz this gave 392 data, for 10Hz 1949 data. The conical scan data were placed with a *cosine* shot management similar to figure 5.2, to give the quoted average pulse rate. The analysis error was calculated for a strip across the orbit, in the middle of the box. The results presented are from an average of nine realizations of each configuration. Figure 5.5 shows as an example the results for along-track and cross-track wind components, for a 2Hz pulse rate, with Pg=0.5. The ratio of the analysis error to the background error is plotted. Because of the statistical noise of only 9 realizations, the curves have been slightly smoothed, and forced to be symmetrical. This smoothing, with a scale of ~150 km, has an effect on the minima of the 4-beam curves in particular, increasing them by about 0.5 ms^{-1}. From the 4-beam curves, we see that the along-track component information does not extrapolate as well in the cross-track direction as does the cross-track component;

---

[1] In practice, optimal pulse rates and powers for the two instruments will differ.

analysis errors for the former are higher in the middle of the two lines of observations, and in extrapolations. This result follows from the covariance properties of a non-divergent wind error field. The same effect is seen when extrapolating the conical scan data. In the centre of the swath the conical scan across-track wind analyses are less accurate, as only the along track component is observed here. This effect was also noted in figure 5.3 and figure 5.4.

Table 5.1: 4-beam v conical lidar scan experiments

Satellite altitude (km)	Scan type	LIDAR pulse rate (Hz)	Observation errors		Analysis error Ea/Eb	plotted in figure
			Eo/Eb	Pg		
450	4-beam	2	.5	.75	.68	5.6bottom
450	4-beam	2	.5	.5	.57	5.5,5.6bot
450	4-beam	2	.5	0	.50	5.6bottom
450	conical	2	.5	.75	.63	5.6top
450	conical	2	.5	.5	.47	5.5,5.6top
450	conical	2	.5	0	.41	5.6top
450	4-beam	10	.5	.75	.57	5.7bottom
450	4-beam	10	.5	.5	.49	5.7bottom
450	4-beam	10	.5	0	.48	5.7bottom
450	conical	10	.5	.75	.42	5.7top
450	conical	10	.5	.5	.37	5.7top
450	conical	10	.5	0	.35	5.7top

Analysis errors are the rms vector errors
for the cross-orbit section shown in the figures.

The different characteristics of the along-track and across-track components were similar in all the experiments. From now on we present the r.m.s. vector error, combining the two. Figure 5.6 and figure 5.7 show the errors for 4-beam and conical scans, 2Hz and 10Hz average pulse rates, with curves for Pg=0, 0.5, and 0.75. The average values across the swath of these curves are shown in the last column of table 1.

Given an appropriate background error covariance model, and Gaussian error distributions, the OI equations can be used directly to predict the analysis error variance for any variable related to the observations. Because the method is intrinsically cheaper, and Monte Carlo simulations are not needed, a wide range of scenarios can be studied easily. We used OI to study the utility of the 4-beam and conical scan configurations in providing information on the vorticity and divergence fields, as well as on wind components. A Gaussian shaped covariance model was used; with this model covariances for all derivatives of the wind field are well defined. One set of experiments used a non-divergent covariance model (2.5). But in the Tropics, we wish to observe both the divergent and the rotational flows; the non-divergent covariance function used in the earlier experiment is not appropriate since it assumes the divergence of the background field is perfectly accurate. Yet, even in the Tropics, flow is largely non-divergent. We therefore assume that 25% of the background error variance is divergent. Streamfunction and velocity potential autocorrelations are both Gaussian shaped, and the cross correlation is zero.

Wind component errors predicted by OI are shown in figure 5.8 for both the non-divergent (Rdiv=0) and the tropical (Rdiv=.25) covariance models. The Gaussian shaped correlations imply that the background is more accurate at small scales than the TOAR function correlations do. Thus, particularly for the non-divergent correlations, extrapolation and interpolation in the direction of the wind component is more accurate. When divergence is allowed, we have less prior knowledge about the flow, and analyses are less accurate. In particular, extrapolation of the cross-track component is less accurate. OI can also predict the errors in the vorticity and divergence analyses; these are shown in figure 5.9. The more widely spread observations from a scanning instrument are better at defining these derived quantities than the 4-beam configuration. Note that the errors with the 4-beam configuration actually have local maxima near the lines of observations, since an observation provides little information about derivatives at the point.

It is clear from all the figures that analyses from a conically scanning instrument are nearly always superior to those from a 4-beam type instrument with all the shots concentrated in two strips. This is even true for large gross error rates (Pg=.75 and Pg=.5), when one might have expected that the close observations would have aided the quality control process. We can therefore conclude that, if the data are to be used in an analysis scheme, the conical scan instrument is to be preferred.

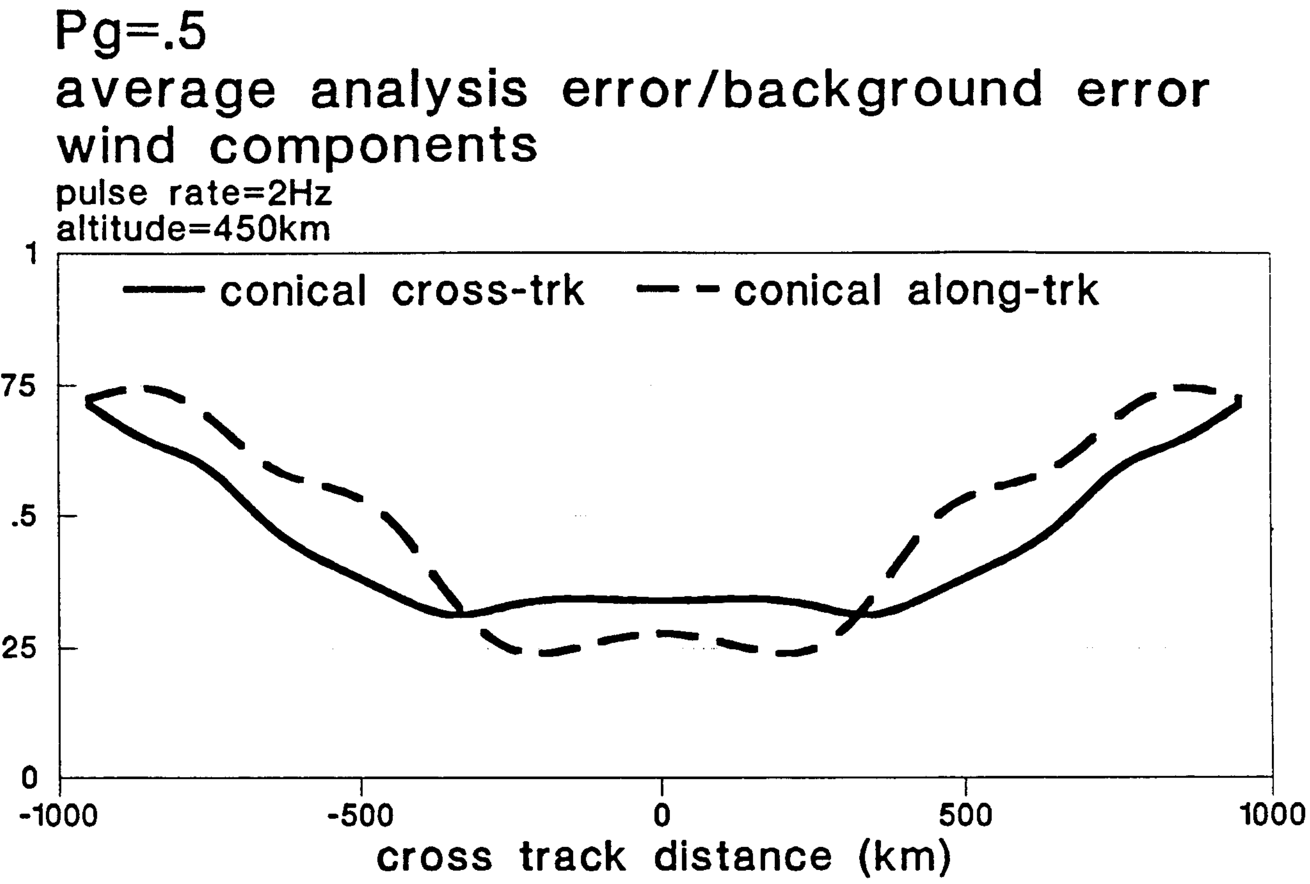

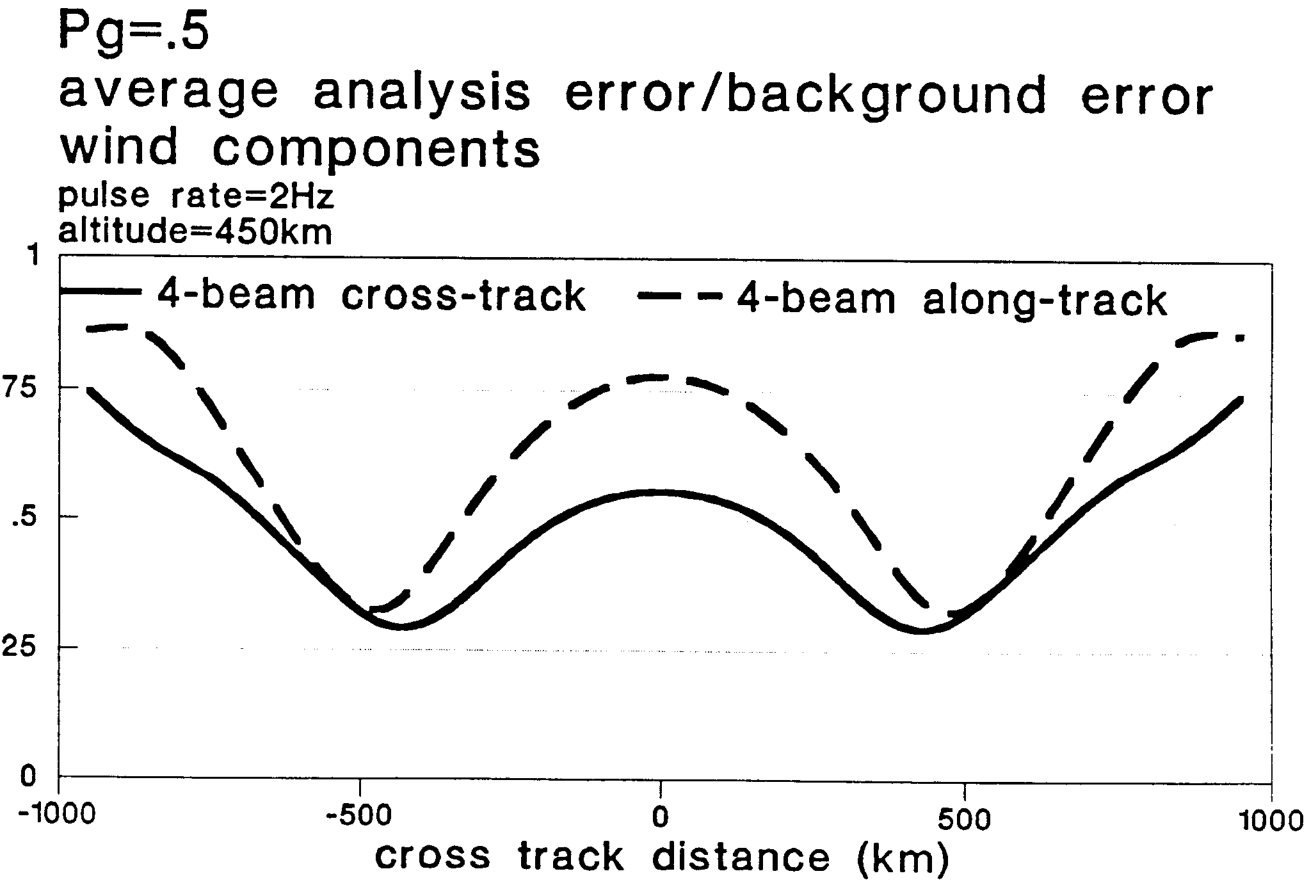

Figure 5.5. RMS analysis error/background error for along-track and cross-track components, from nine simulations, plotted against distance from the centre of the swath.

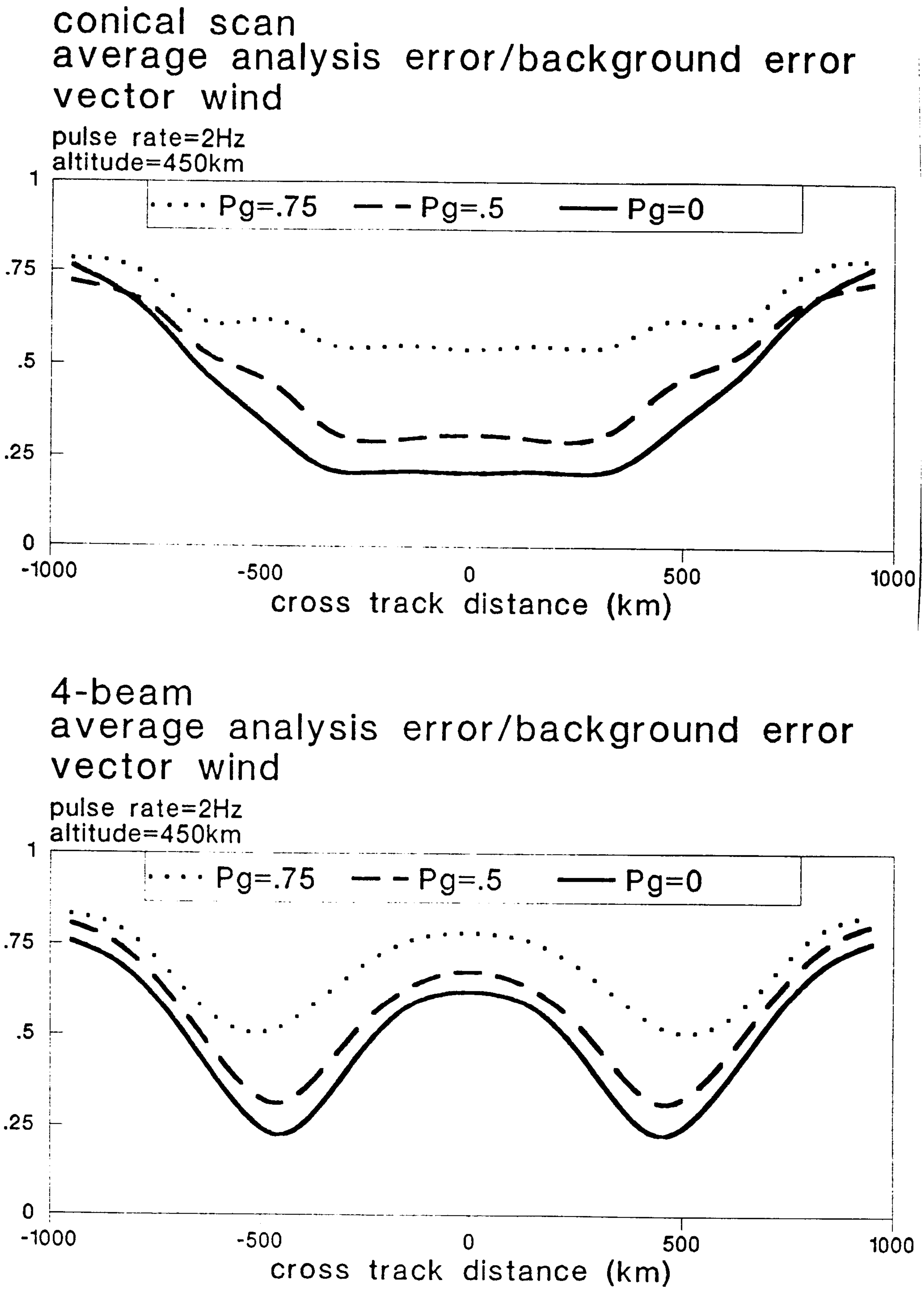

Figure 5.6. RMS vector wind analysis error/background error, for various probabilities of gross error, for conical scan and 4-beam configurations with a 2Hz pulse rate.

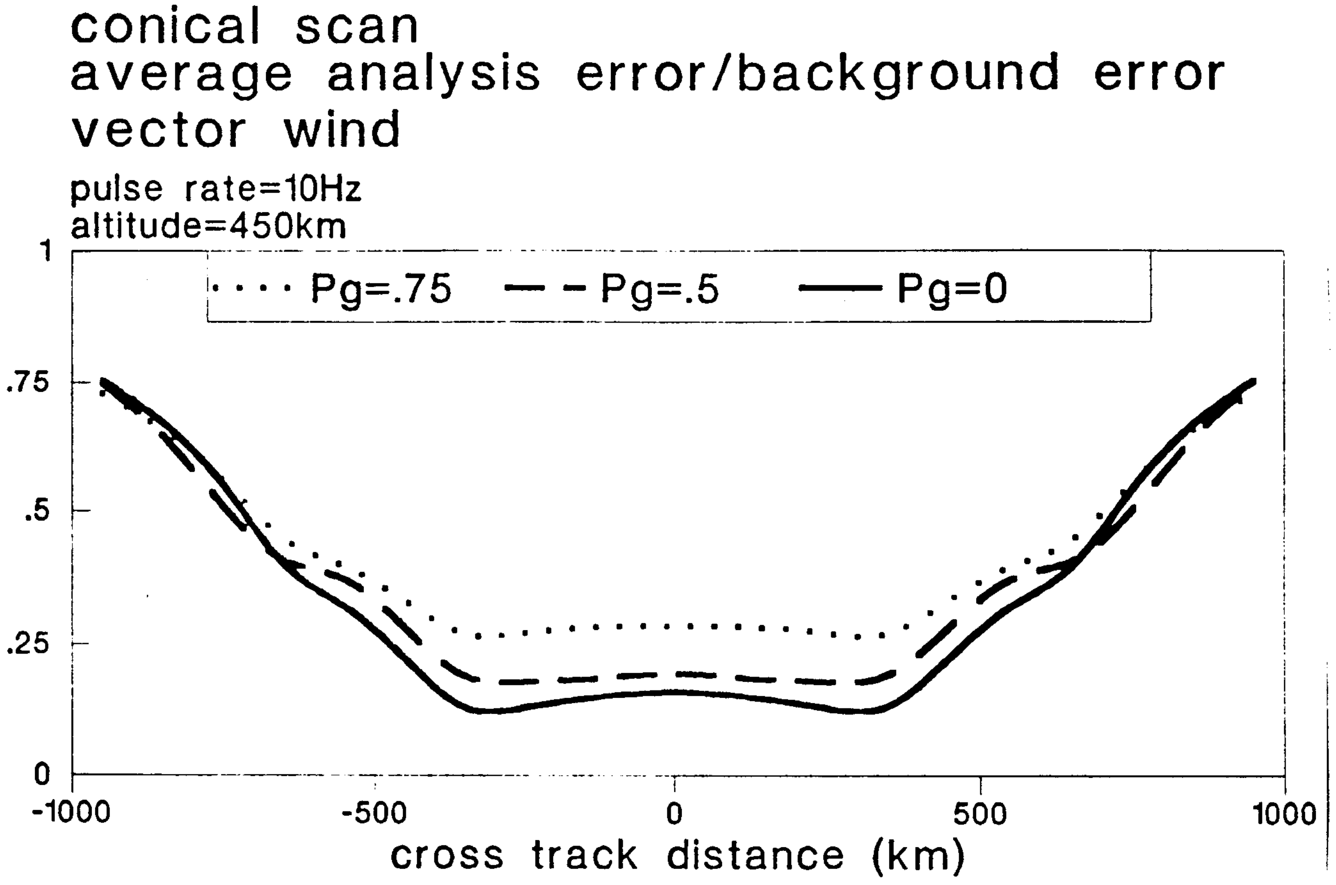

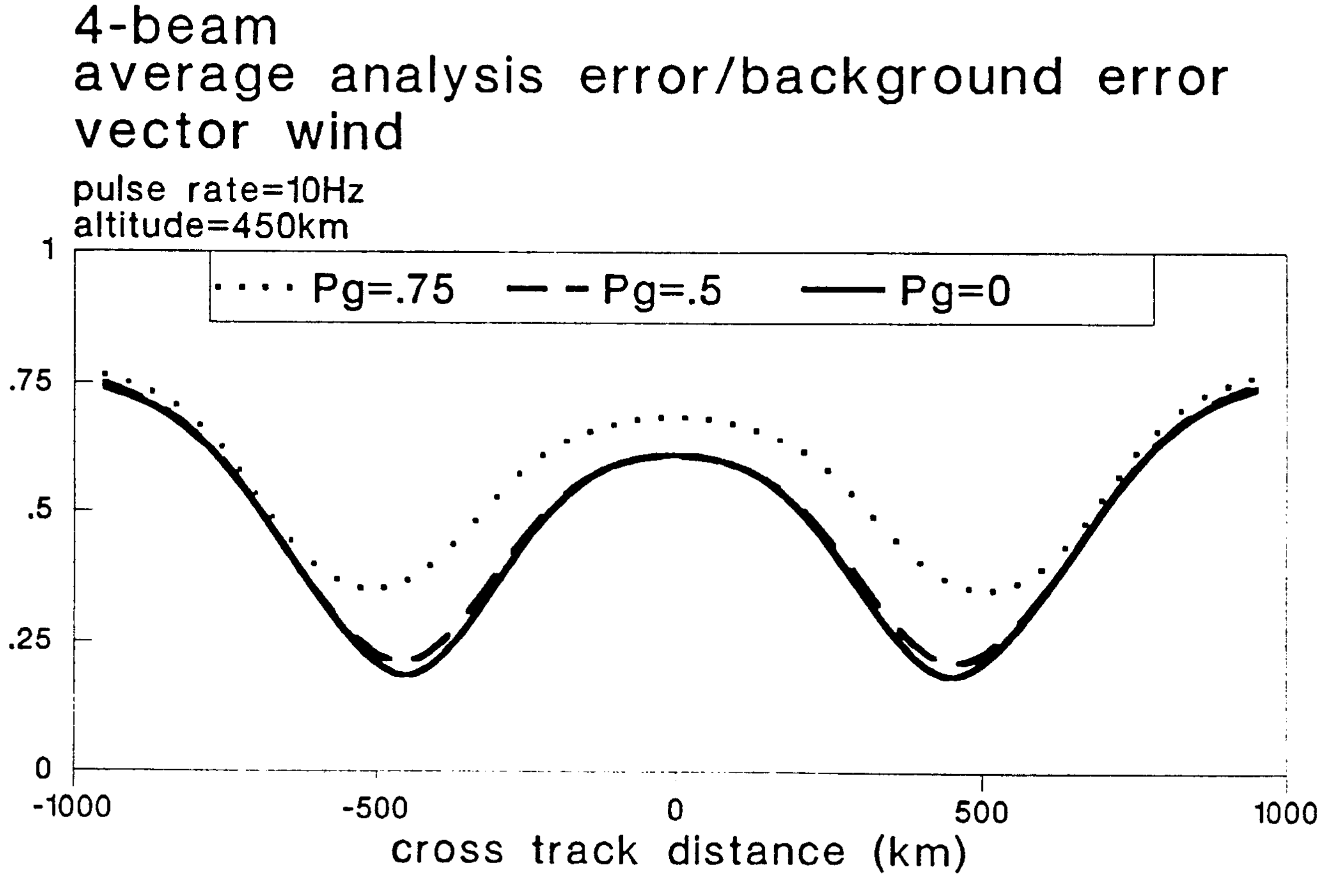

Figure 5.7. As figure 5.6 for a 10Hz pulse rate.

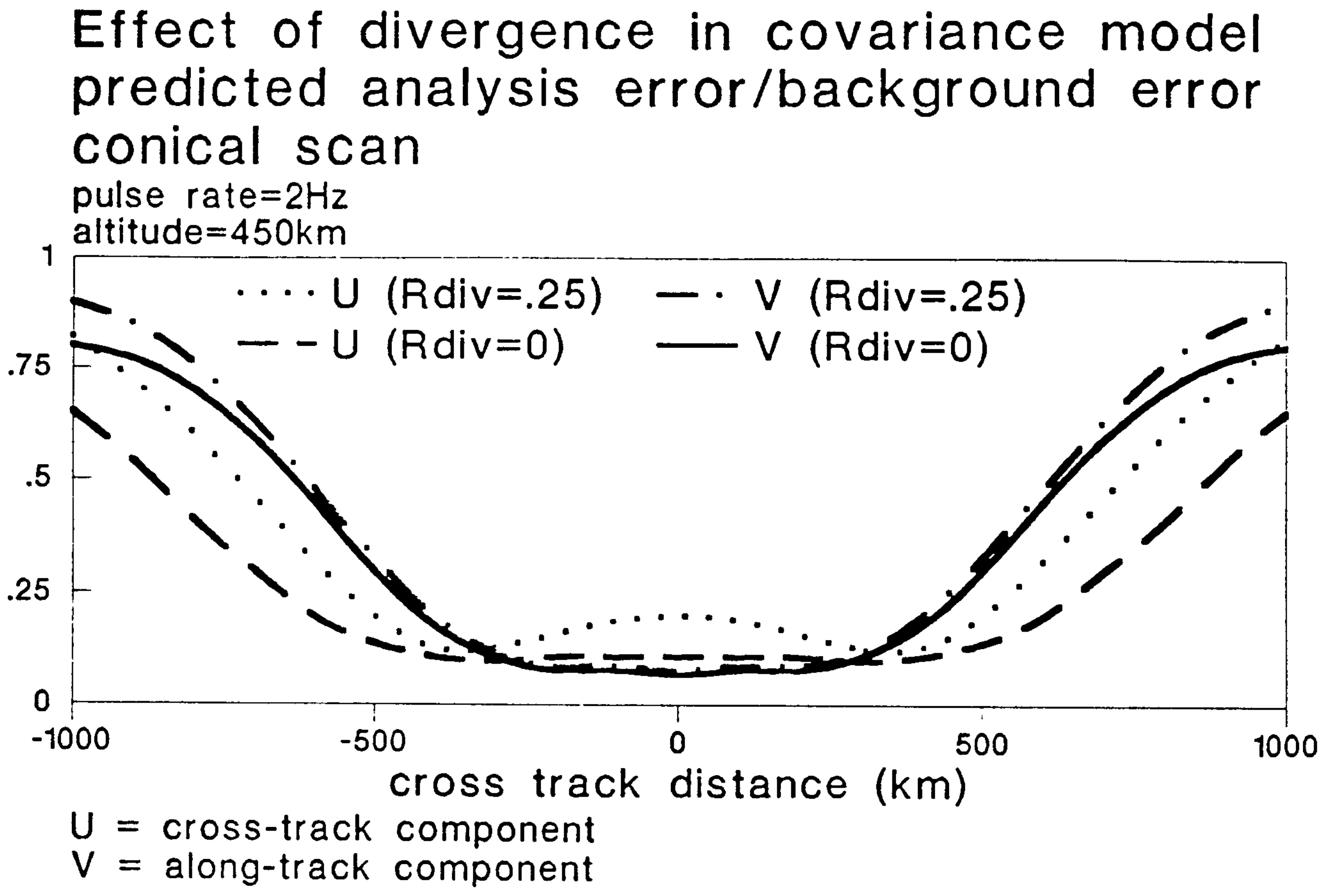

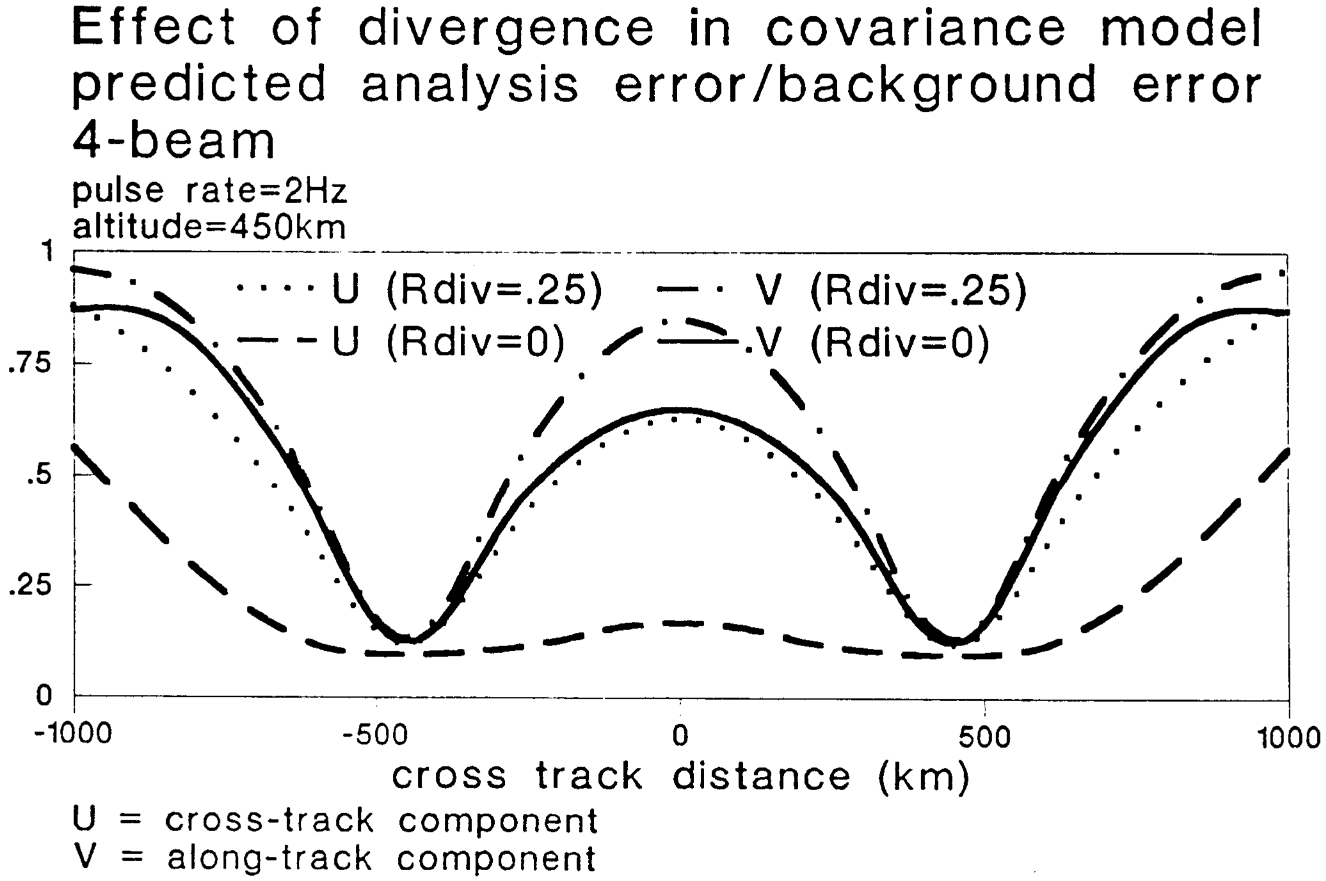

Figure 5.8. RMS wind component analysis error/background error, using OI (with Pg=0), and a covariance function allowing for a fraction Rdiv of the background errors to be in the divergent wind.

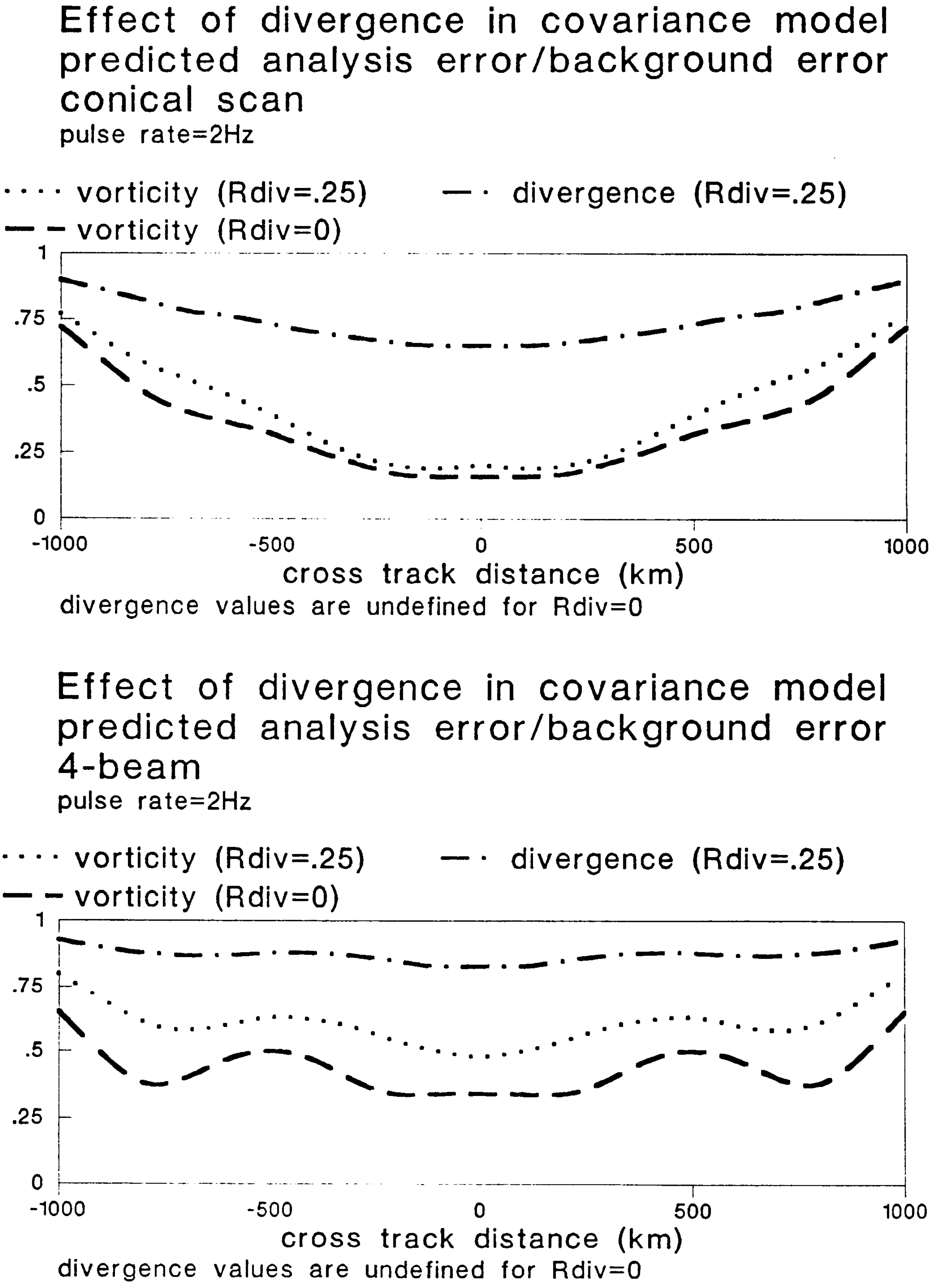

Figure 5.9. As figure 5.8, showing the relative analysis errors for vorticity and divergence.

6. Case studies of the effect of cloud obscuration on the utility of lidar winds

6.1 Impact on predictions of extratropical cyclogenesis

Intense extratropical cyclones are often associated with winds of damaging strength, and their accurate prediction is clearly desirable. Such systems typically form in oceanic regions, and may intensify very quickly. The precision with which NWP models are able to predict rapid cyclogenesis is greatly hampered by the current scarcity of observations over the oceans, and it is reasonable to expect that the increased wind data coverage that a space borne Döppler lidar would bring, would significantly improve NWP forecasts of these events. However, cyclogenesis is invariably accompanied by widespread cloud, and if structure in the wind field important to the cyclogenesis is regularly obscured, the benefit of the lidar data may be less than at first expected. To get a feel for the likely impact of cloud on the utility of the lidar data three case studies of cyclogenesis are presented below. The approach is to first identify the flow structure important to the onset of cyclogenesis, and then to ascertain the degree to which cloud cover would obscure the structure from observation by lidar. The cases selected have been the subject of observation sensitivity studies, and the flow structure important to the cyclogenesis has therefore already been established. The degree of cloud cover is estimated by NWP model relative humidity levels - 70% or greater humidity has been taken to imply complete cloud cover.

Case 1: 15/16 October 1987

The first case is taken from a study by Lorenc *et.al.* (1988) of the violent storm which affected southern England during 15/16 October 1987. Figure 6.1 shows the 250mb contour and isotach analysis, prior to the onset of the storm, at 00GMT 15 Oct. 1987 (solid lines are contours; dashed lines are isotachs, in knots). A strong jet core (160kn) is evident to the south-west of Newfoundland between 30-45W. Two 24hr forecasts of mean sea level pressure (PMSL) from initial analyses at this time are shown in insets a&b. The plotted data in the main part of figure 6.1 are AIREP observations of wind and temperature that were included in the initial analysis for forecast **b** but not in the initial analysis for forecast **a**. It can be seen that the observations are well placed to define the structure of the jet core in the NWP analysis, and the resulting impact may be appreciated by comparison of the two

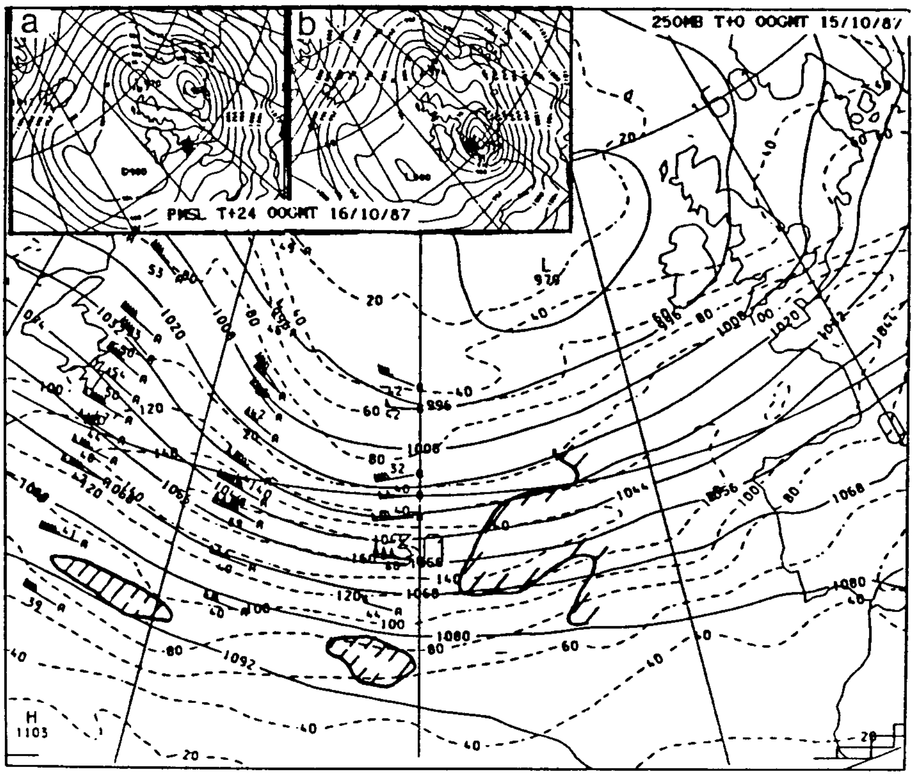

Figure 6.1: Nominal initial analysis at 00GMT 15/10/87 for the two 24hr forecasts shown in the insets **a** and **b**. Continuous lines are height contours in decametres; dashed lines are isotachs in knots. The plotted data are aircraft observations of wind and temperature that were used in the analysis for forecast **b** but not for forecast **a**. Areas covered by extensive cloud (as inferred from model humidity levels) have been delineated. The actual position of the low at 00GMT 16/10/87 is marked "●" in the insets.

forecasts. The actual position of the low at 00GMT 16 October is shown in both figures. Forecast **a** is clearly very poor, whilst forecast **b** succeeds in predicting the position of the low with considerable accuracy (the central pressure was also well predicted). Although there were other differences between the initial analyses for forecasts **a** and **b** (see Lorenc *et.al.*,1988), the role of the wind part of the AIREP report was considered to be crucial.

We now ask the question; how much of the critical region of the jet core would have been visible to a satellite borne lidar on an overhead pass? The region in which the model humidity (at 300mb) is equal to or greater than 70%

has been outlined in figure 6.1, and may be assumed to represent total cloud cover. It is clear that the main cloud head is located well to the east of the jet core (the jet core itself was in a region of relatively low humidity, 10-50%). We can conclude that, in this case at least, lidar observations would have made an important contribution to the satisfactory definition of the jet structure in the initial analysis.

Case 2: 12GMT 28 October 1989

A further example, taken from a study of the impact of Atlantic TEMPSHIP data on NWP forecasts (Graham, 1989), is illustrated in figure 6.2. The main figure shows the 250mb contour and isotach analysis at 00GMT 27 October 1989, some 36hrs before a cyclone, initially positioned at "X", intensified and moved over the UK. Two 36hr forecasts of PMSL from initial analyses at 00GMT 27 October are shown in the insets "a" and "b" - the actual position of the low at 12GMT 28 October is marked on both figures. Referring to the main figure, a strong jet core (140kn) may be seen in mid-Atlantic on the western flank of a trough in the 250mb flow. The plotted data represent the 250mb observations from TEMPSHIP wind profiles that were used in the initial analysis for forecast **b**, but not in that for forecast **a**. The impact of the data may be appreciated by comparison of the two forecasts. Although both forecasts produced a central pressure which was too low by 10mb, forecast **b** has made a much better prediction of the low position. Graham showed that much of the impact derived from three observations (singled out with arrows in figure 6.2), which were distributed both across the trough axis and within the strong shear on the northern side of the jet. Although the impact of the temperature and wind parts of the TEMPSHIP data were not separated; the large impact of the data on the analysis of the wind field suggested that the wind part was by far the most important. The largest impact on the wind speed analysis was at the 400mb level.

The region in which relative humidity was equal to or greater than 70% has been delineated, and may be taken to represent the area of total cloud cover. In this case much of the northern part of the trough, below 300mb, would have been obscured by cloud, and the benefit of lidar data for this case is less clear cut than in the former case. However, much of the region of the jet core, and the region of strong wind shear to its north and east would have been visible, and may well have compensated for the lack of coverage at the trough axis.

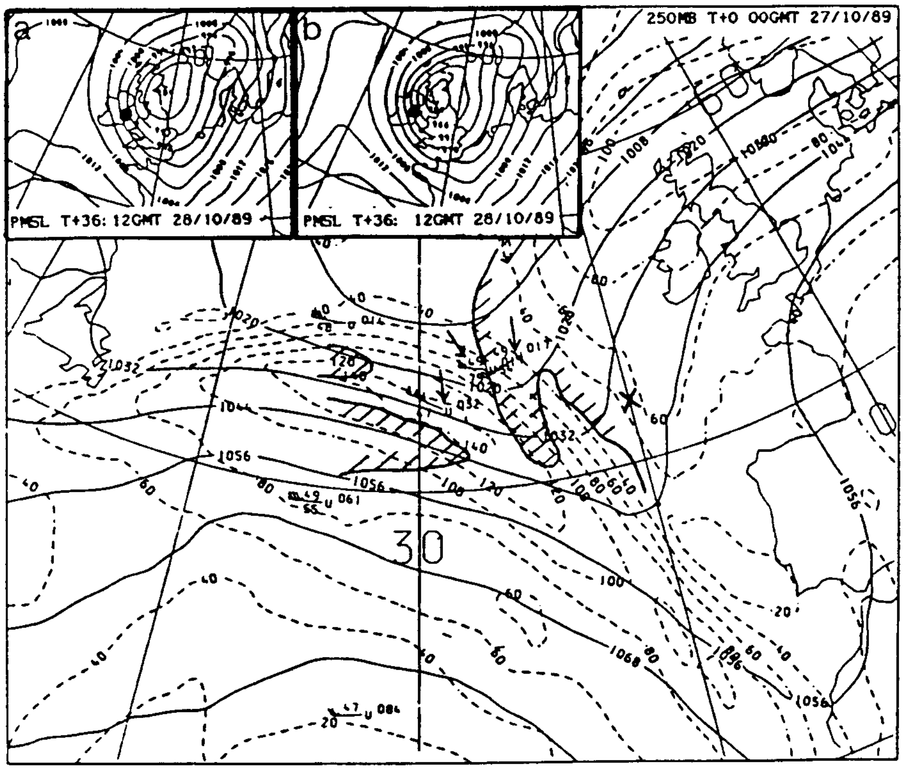

Figure 6.2 Nominal initial analysis at 250mb, 00GMT 27/10/89 for the two 36 hour forecasts shown in the insets **a** and **b**. Plotting conventions are as figure 6.1. The plotted data are the 250mb observations from vertical profiles of wind and temperature (from TEMPSHIPS) which were used in the initial analysis for forecast **b** but not for forecast **a**. The position of the low is marked "X" (00GMT 27/10/89) and "●" (12GMT 28/10/89 (insets)).

Case 3: 15 September 1989

To complement cases 1&2, we include a case (taken from Graham, 1991) in which a good analysis of the low-level wind field, rather than the jet stream, is crucial to the success of the forecast. Figure 6.3 shows the 700mb flow over the Atlantic at 12GMT 12 September 1989. An old hurricane circulation ("Gabrielle") was located at "X" and subsequently tracked north-eastward and intensified to be positioned west of Scotland at 12GMT 15 September. Two 72hr forecasts from slightly different initial analyses are shown in the insets "a" and "b". The plotted data on the **main** figure are the 700mb observations from TEMPSHIP profiles used in the initial analysis for forecast **a** but not for

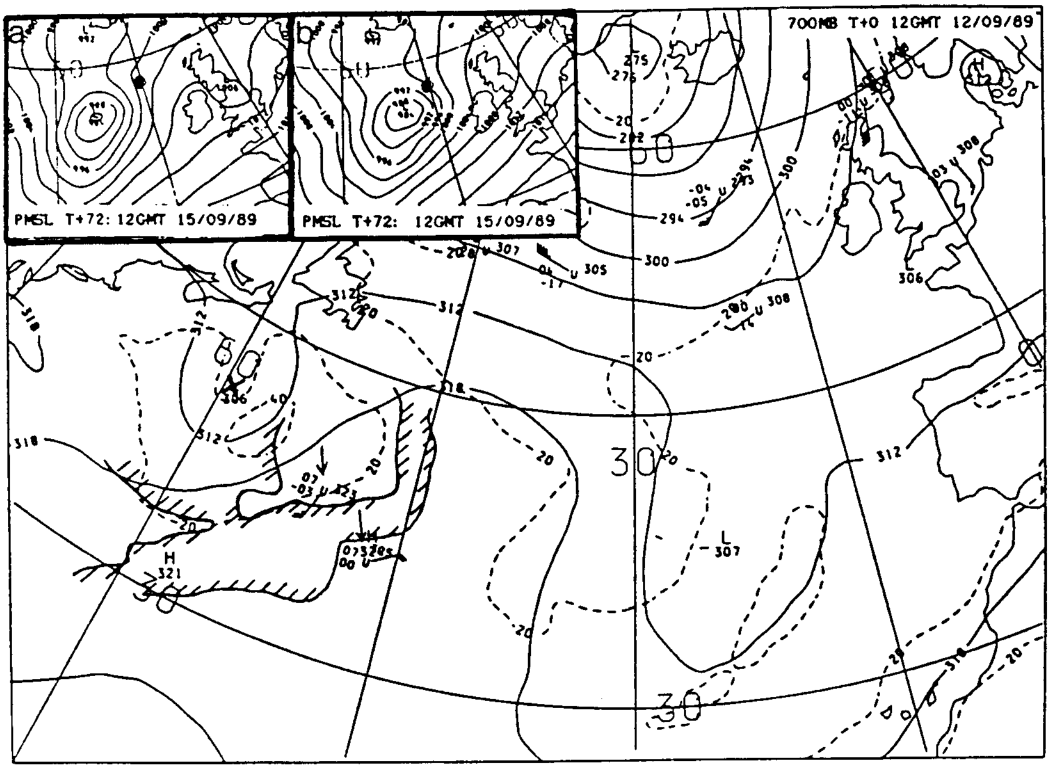

Figure 6.3 Nominal initial analysis at 700mb, 12GMT 12/09/89 for the two 72 hour forecasts shown in the insets **a** and **b**. Plotting conventions are as figure 6.1. The plotted data are the 700mb observations from vertical profiles of wind and temperature (from TEMPSHIPS) used in the initial analysis for forecast **b** but not for forecast **a**. The position of "Gabrielle" is marked "X" (12GMT 12/09/89) and "●" (12GMT 15/09/89 (insets)).

forecast **b**. The impact of the data may be appreciated by comparison of the two forecasts. In both forecasts the central pressure of the depression was too high (by ~10mb) and the position was south-west of the actual position (marked ●). However forecast **a** is clearly better guidance to the position of the low. Graham showed that most of the impact is due to the two observations singled out on the eastern side of "Gabrielle" which defined the band of enhanced low level wind strengths on the eastern flank of the circulation.

In this case cloud cover above the 700mb level was estimated using a 70% humidity threshold, at 700mb, 500mb and 300mb and assuming maximum overlap of the cloud at these levels. As can be seen from figure 6.3, the crucial wind structure would have been visible to the lidar, despite being at low altitude.

The overall conclusion suggested by the case studies is that cloud obscuration may not seriously effect the impact of lidar in improving NWP forecasts of cyclogenesis. The reason for this is that flow structures (i.e. jet streams) closely associated with cyclogenesis are often well defined some time in advance of the event, when they are not necessarily accompanied by widespread cloud.

6.2 Impact on utility for calculating moisture budgets

Part of the aim of the GEWEX experiment is an improved understanding of global and regional moisture transport, and deployment of a satellite Döppler lidar instrument is generally considered necessary to obtain the high resolution wind data necessary to achieve this goal. The benefit of lidar data in this respect will be impaired by the fact that low-level wind systems giving rise to significant moisture transport are frequently located beneath clouds - and therefore will not be observed by the lidar. To demonstrate this point, two examples of moisture transport associated with mid-latitude frontal systems are given below, using both synoptic observations and simulations from the UK Met. Office mesoscale model. Subsequently, with the aid of the UK Met. Office Unified model, we illustrate how cloud obscuration will introduce sampling biases in global observation of moisture flux based on lidar winds.

6.2.1 Impact on regional scales

Case 1 : 23 November 1990

Figure 6.4 shows a 12hr mesoscale model forecast of the 1.5km wind field over the UK valid for 12GMT 23 November 1990, the cloud fraction at the 4km level is also shown. A marked front lies approximately north-south across the British Isles, and may be appreciated by the marked wind shift across the front (along the eastern coast of Ireland, for example) and the band of extensive cloud cover. A vertical cross section through the line shown in figure 6.4 is reproduced in figure 6.5, which shows wind speed perpendicular to the cross section (approximately parallel to the front) - regions where cloud cover is 7/8 or more are shown shaded. A well defined maximum in the low-level flow, reaching 18ms^{-1}, may be seen ahead of the front at a height of ~1.5km. It is clear from figure 6.5 that the wind maximum will be completely obscured to observation from above by the accompanying frontal cloud. Shortly we shall show, using the mesoscale model fields, that the low-level jet - which will not be visible to the lidar - plays a dominant role in the local moisture transport. First, however, we verify that the main features of the model simulation are reasonable representations of the observed structure. The synoptic observations at 12GMT 23 November are shown in figure 6.6. An area of continuous rainfall associated with the front has been delineated and clearly corresponds well with the cloud band in the forecast (figure 6.4) The inset to figure 6.6 shows a time series, generated from radiosonde data at Cambourne (marked X), of the vertical profile of the wind component parallel to the front; the area of the cross-section corresponds to the enclosed part of the cross section in figure 6.5. It is clear that the low-level jet is a well defined feature of the actual flow and that the model has made a reasonable simulation of the flow structure. Such low-level jet structures ahead of the cold fronts are well documented and are known as "warm conveyor belts" (Browning, 1986).

The total and meridional moisture fluxes at 1.5km are shown in figures 6.7&6.8 respectively. The striking feature of both figures is the narrow band of strong northward moisture flux (max $9\times10^{-2}\mathrm{Kgm}^{-2}\mathrm{s}^{-1}$) associated with the low level jet. Comparison of figures 6.8&6.4 will confirm that this narrow band of strong moisture transport is located squarely beneath the frontal cloud band - and consequently would not be visible to the lidar.

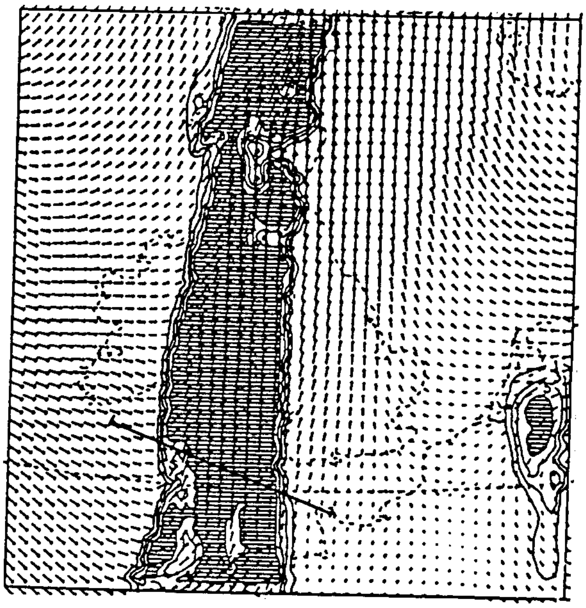

Figure 6.4 12hr forecast, valid 12GMT 23 Nov. 1991, for the flow pattern at 1.5km and cloud cover at 4km associated with a front over the British Isles. Cloud cover greater than 7/8 is shown shaded. The line drawn through south-west England shows the plane of the vertical cross section in figure 6.5.

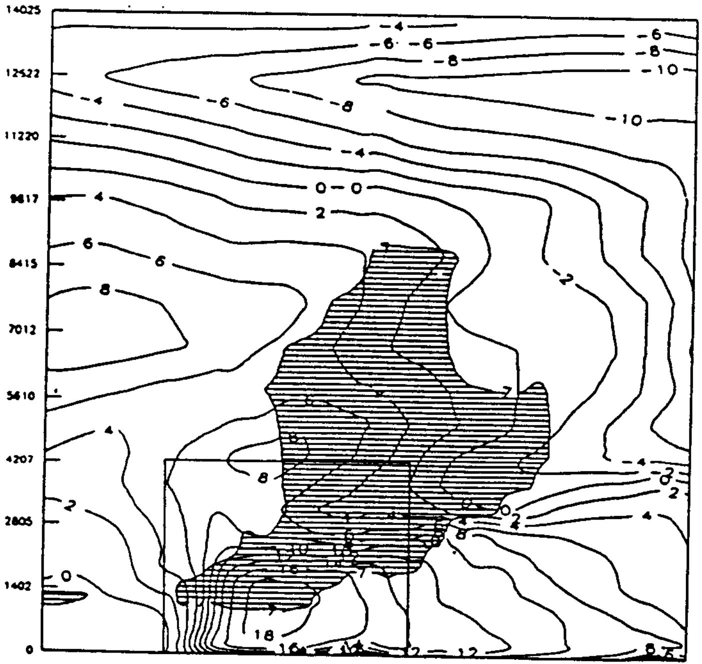

Figure 6.5 Vertical cross section (for T+12 forecast valid 12GMT 23 Nov. 1991) along the line shown in Fig.6.4. Continuous lines show wind speed perpendicular to the cross section (approximately parallel to the front); Regions more than 7/8 cloud cover are shown shaded. The enclosed region corresponds to that shown in the inset of figure 6.6.

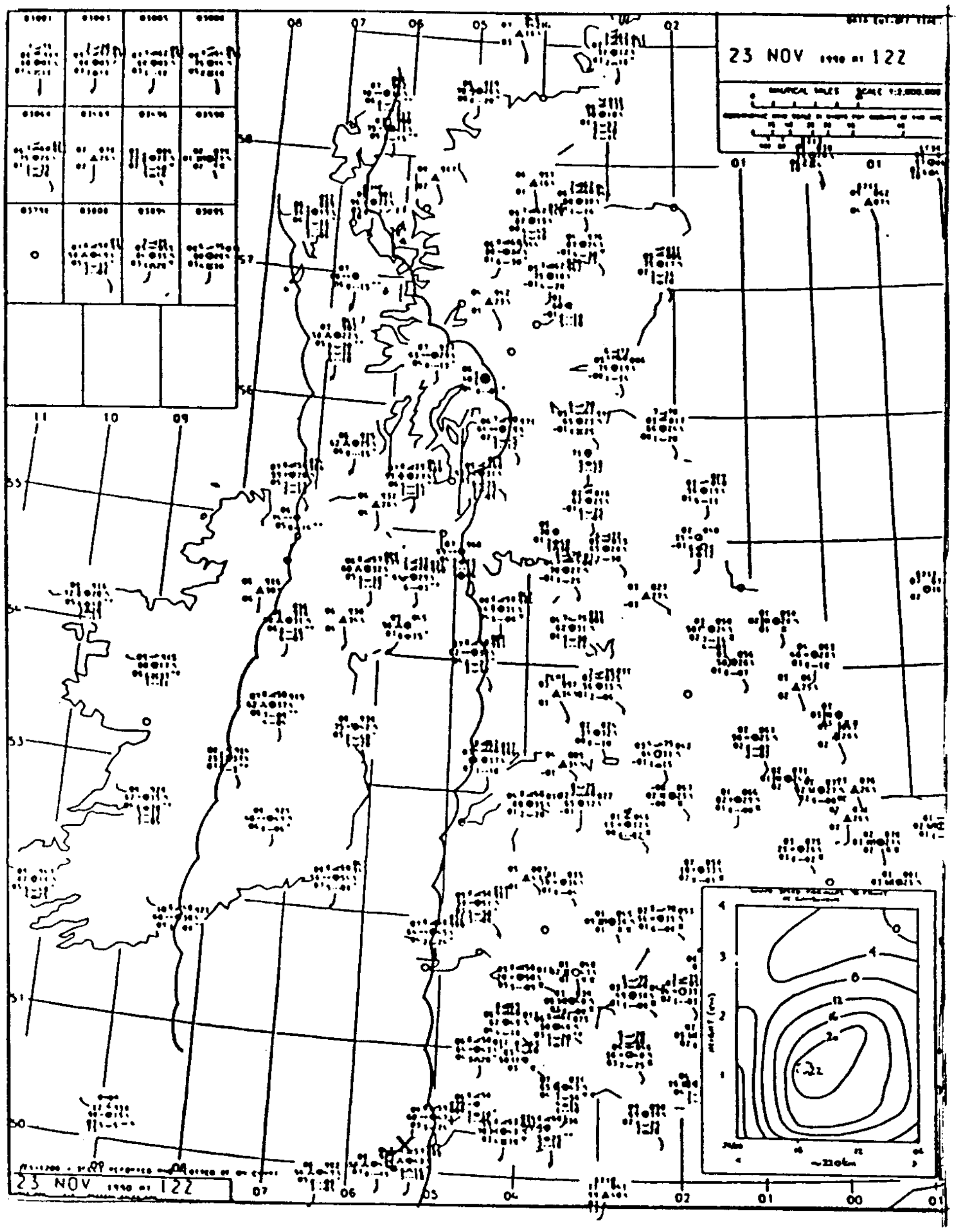

Figure 6.6 Synoptic observations at 12GMT 23 Nov. 1991. The band of of continuous rainfall associated with the front has been delineated. The inset shows a vertical cross section of the wind speed parallel to the front derived from radiosonde data from Cambourne (X).

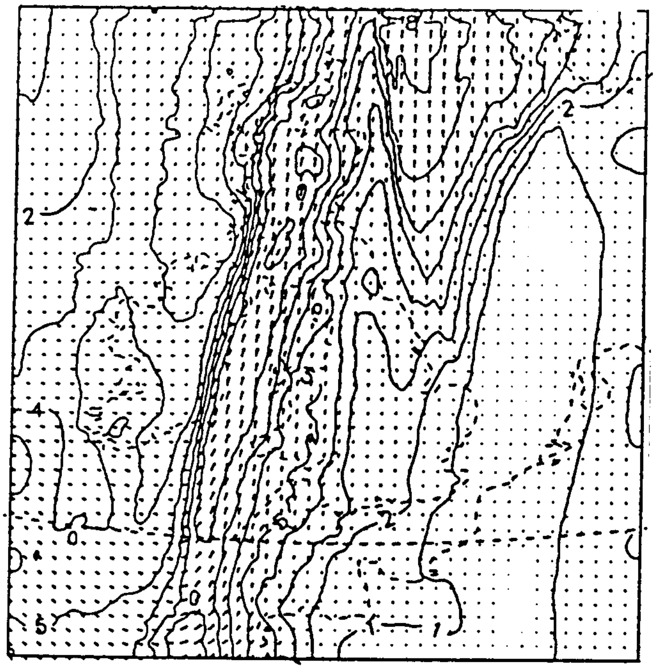

Figure 6.7 Total moisture flux (units $10^{-2}Kgm^{-2}s^{-1}$) at 1.5km derivedfrom the forecast fields. Times are the same as for figure 6.4.

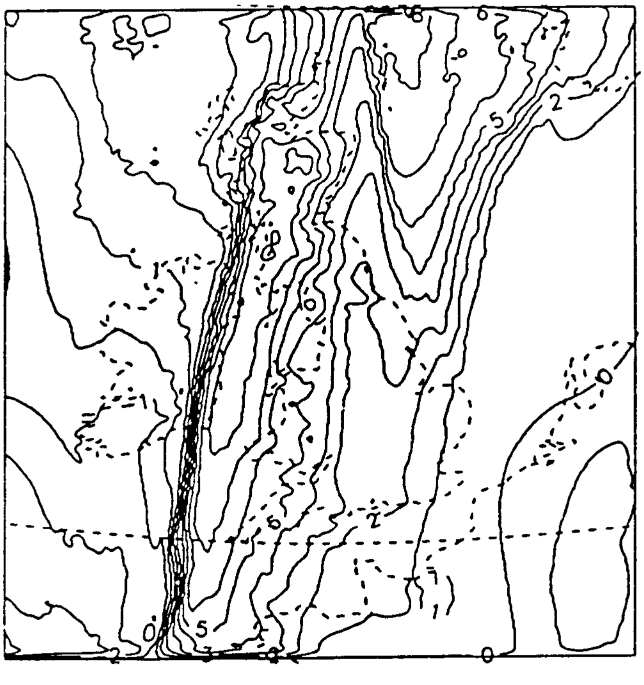

Figure 6.8 As for figure 6.7 but for the meridional component of the moisture flux.

Case 2: 4 April 1991

A similar example is illustrated in figures 6.9 - 6.11, for a front which crossed the U.K.on 4th April 1991. The rainband associated with the front, at 06GMT, is shown in figure 6.9, in which the region covered by rainfall of moderate or heavy intensity has been delineated. The inset to figure 6.9 is a time series of radiosonde winds from Cambourne - and shows a low-level wind maximum of $32ms^{-1}$ situated ahead of, and parallel to, the front at a height of 1km. Comparison of the radiosonde wind profiles with vertical cross sections obtained from mesoscale model fields showed that the low-level wind maximum was reasonably well simulated by the model. The total and meridional moisture flux at 1.5km calculated from the mesoscale model fields are shown in figures 6.10&6.11 respectively. A region of strong northward moisture flux within a narrow band associated with the wind maximum is again visible. The moisture flux reaches a maximum of $12\times10^{-2}kgm^{-2}s^{-1}$ over Wales and south-western England, directly beneath the main band of cloud and rain shown in figure 6.9.

The two cases described above illustrate that, in mid-latitudes at least, the presence of cloud in regions of marked moisture transport will frequently obscure such regions from observation by lidar.

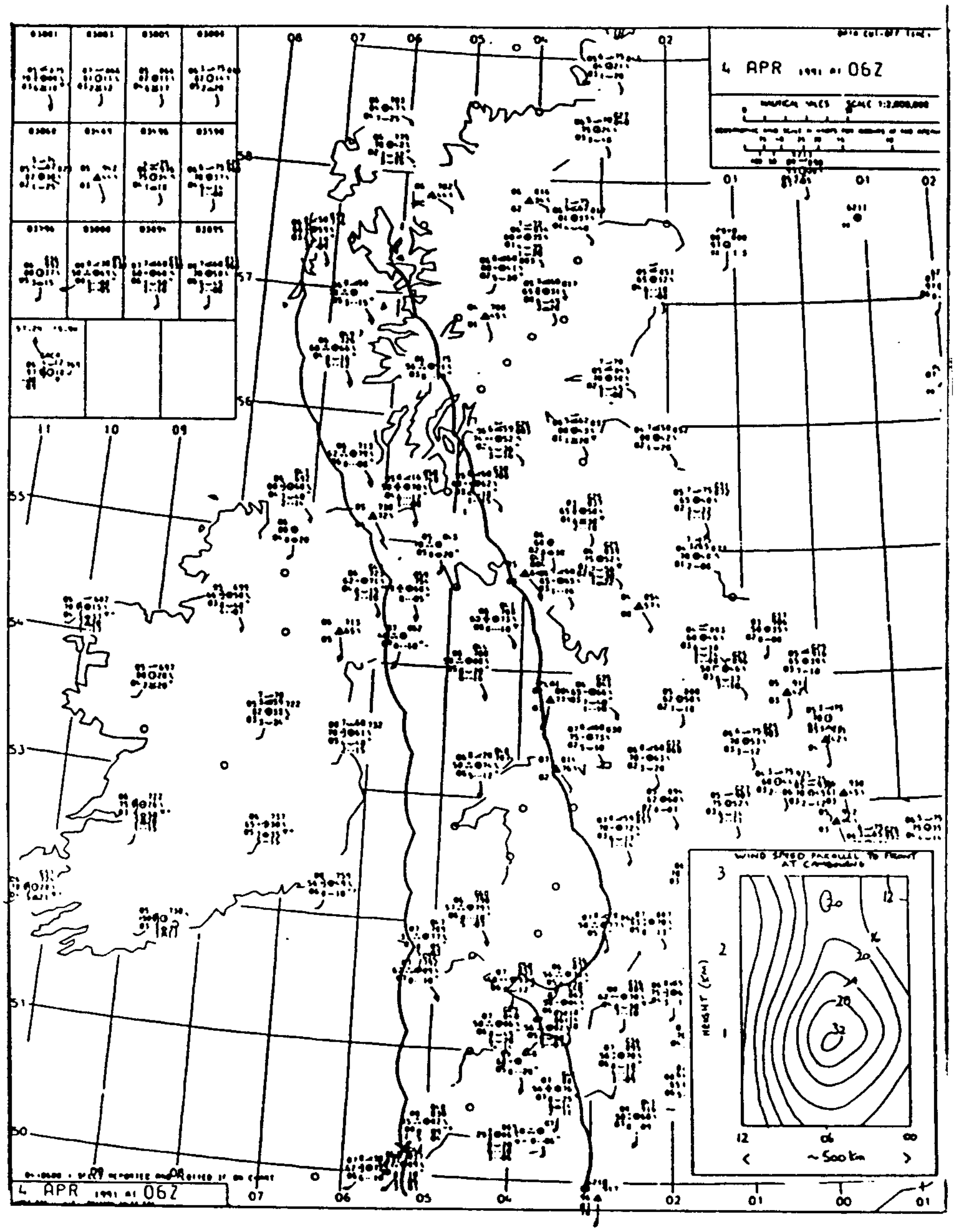

Figure 6.9 Synoptic observations valid 06GMT 4 April 1991. Theband of moderate to heavy continuous rainfall associated with the frontis shown. The inset shows a vertical cross section of wind speed parallelto the front derived from radiosonde data at Cambourne (X).

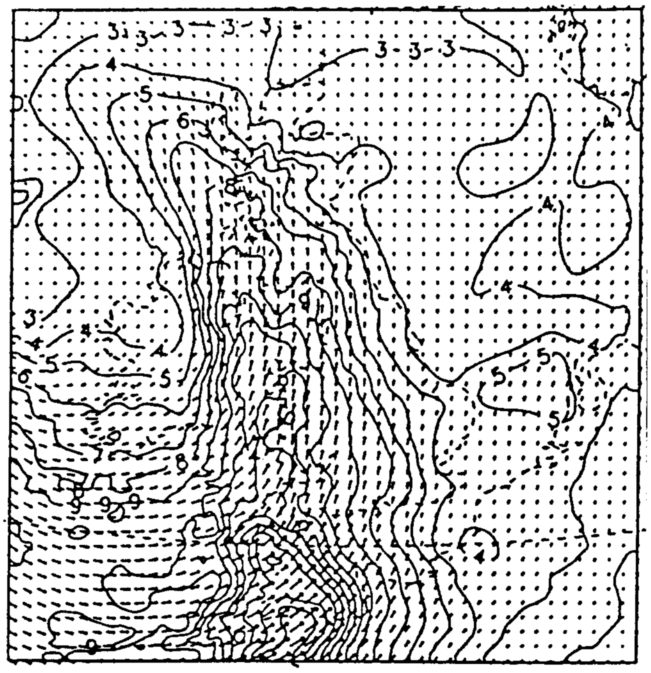

Figure 6.10 Moisture flux at 1.5km (units $10^{-2}Kgm^{-2}s^{-1}$) derived from model 6hr forecast valid 06GMT 04 April 1991.

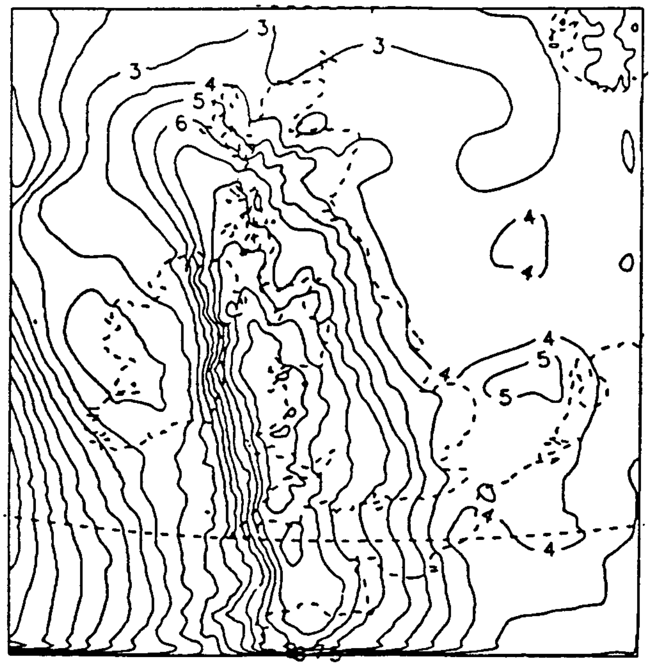

Figure 6.11 As for figure 6.10 but for the meridional componentof the moisture flux.

6.2.2 Impact on the global scale

The case studies discussed above suggest that, in mid-latitudes, lidar wind observations will be most numerous in regions of weak moisture flux. The utility of the observations for climate studies will be hampered by this bias in the sampling, and best use of the data is likely to come from its incorporation in an NWP 4-D data assimilation process. To illustrate the difficulties in using the observations, without a data assimilation process, to estimate global moisture transport we have performed the following study. Model analysis fields (from the UK Met. Office unified model) were used to compare the moisture flux across selected latitude circles with that part of the moisture flux which occurs beneath clear skies. Since the greater part of the moisture flux occurs at low-levels, only the flux at 850mb has been considered. The procedure, which was applied using an analysis for 12GMT 20 June 1991, was as follows. First, the 850mb meridional moisture flux across each model grid length was calculated along selected latitude circles. Second, to obtain the part of the flux occurring under clear skies, the flux across each grid length was multiplied by the fraction of clear sky, above 850mb, assigned to the grid square corresponding to the grid length. The fraction of clear sky is calculated by assuming a random overlap of high-level, medium-level and convective clouds, i.e.

$$\begin{aligned}\text{fraction of clear sky above 850mb} &= (1 - \text{high cloud fraction})\\ &\quad\times(1 - \text{medium cloud fraction})\\ &\quad\times(1 - \text{convective cloud fraction}).\end{aligned}$$

High, medium and convective cloud amounts were obtained from the model output fields. Low cloud amounts were not used in the above equation because the 850mb level falls within the height range assigned for "low" clouds and therefore, in some cases, the top of the low cloud may be below 850mb (i.e. stratus), and observation of the 850mb level would not be affected. The omission of low clouds will contribute to under estimation of the degree of obscuration. Finally, the total and "clear sky" moisture fluxes were partitioned into the contributions from a range of flux intensity bands; each band being of width $5\times10^{-2}\text{Kgm}^{-1}\text{s}^{-1}$.

The moisture fluxes across 50N and 30N are shown in figures 6.12 and 6.13 respectively for a number of categories of flux intensity. The histograms show the moisture flux integrated over each intensity band; the full bars show the total moisture flux and the black bars the "clear sky" moisture flux. Total and "clear sky" fluxes integrated over all intensity bands are shown in table 6.1. Referring first to figures 6.12 and 6.13 the following points are evident for both latitudes;

- More than half the total poleward flux is contributed by regions where the flux exceeds $5\times10^{-2}Kgm^{-1}s^{-1}$, and in these regions the "clear sky" flux is less than half the total flux (about 1/4 at 50N). Nearly all regions with poleward fluxes exceeding $10\times10^{-2}Kgm^{-1}s^{-1}$ are completely obscured by cloud - a result that is consistent with the conclusions of the case studies of frontal systems.

Reference to table 6.1 shows that;

- About half (less at 50N) the total poleward flux occurs beneath clear skies. In contrast there is little obscuration of the equatorward flux, about 80% of which occurs beneath clear skies. As a result the net "clear sky" poleward flux is considerably smaller than the net total flux, and is negative at 50N and 30N. Because of the strong weighting of lidar wind observations to clear sky regions, the smaller net poleward flux in the "clear sky" case would be likely to appear as a bias in flux estimates based on lidar wind data.

At 10N (figure 6.14) the pattern is somewhat different, with poleward moisture flux in the range $5\text{-}10\times10^{-2}Kgm^{-1}s^{-1}$ being the most obscured. The "clear sky" flux at this latitude is about .64 the total poleward flux.

The results given above suggest that the proportion of poleward moisture flux that occurs beneath clear sky increases with decreasing latitude. Because the results are very dependent on the model cloud formulation the reliability of this trend must be treated with caution. It may, however, reflect the organisation of mid-latitude weather systems in which poleward moving, ascending currents of moist cloudy air are a characteristic feature - as illustrated by the case studies in the previous subsection. Also, the greater proportion of clear sky flux at 10N may be influenced by poleward moisture flux in the south-west monsoon - a significant part of which may not be associated with widespread cloud.

The results suggest that it will be difficult to obtain reliable estimates of global moisture transport from data based on lidar wind observations, because the distribution of lidar data will be weighted towards regions of equatorward moisture flux. For the purpose of climate studies best use of the data will come from its incorporation in an NWP model assimilation process. The need for an NWP assimilation implies that, for the purpose of climate models, there is little advantage in making simultaneous measurements of wind and moisture from the same platform.

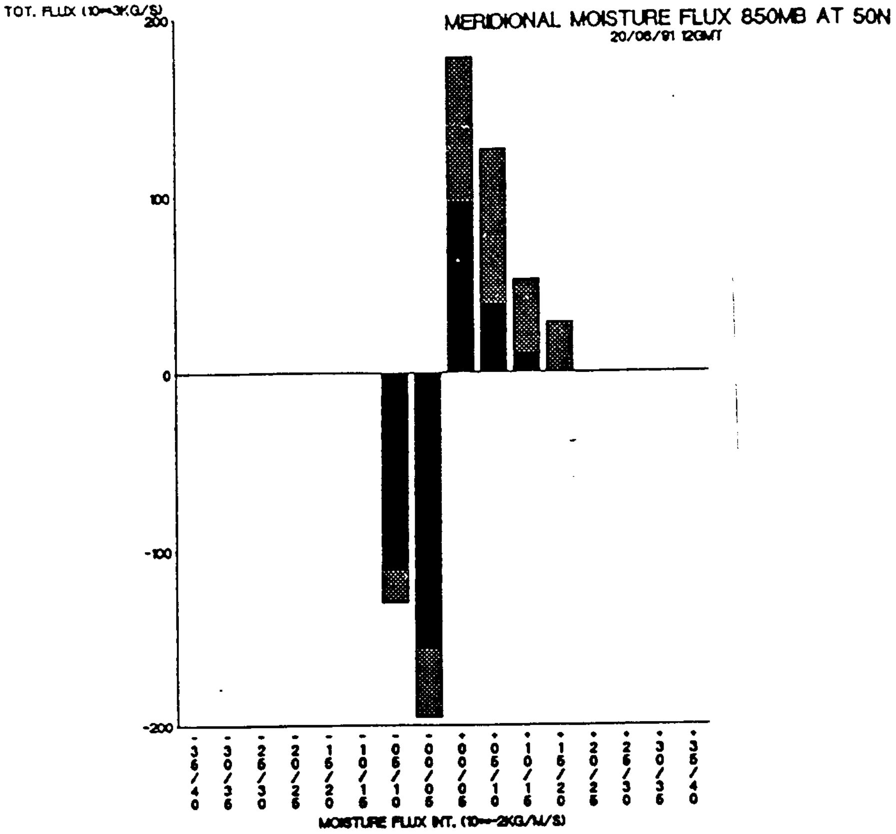

Figure 6.12 The meridional moisture flux, integrated over intensity bands, across 50N at 850mb (as derived from a global model analysis at 12GMT 21 June 1991. The full bars show the total moisture flux, the black bars the "clear sky" moisture flux, in the given intensity band.

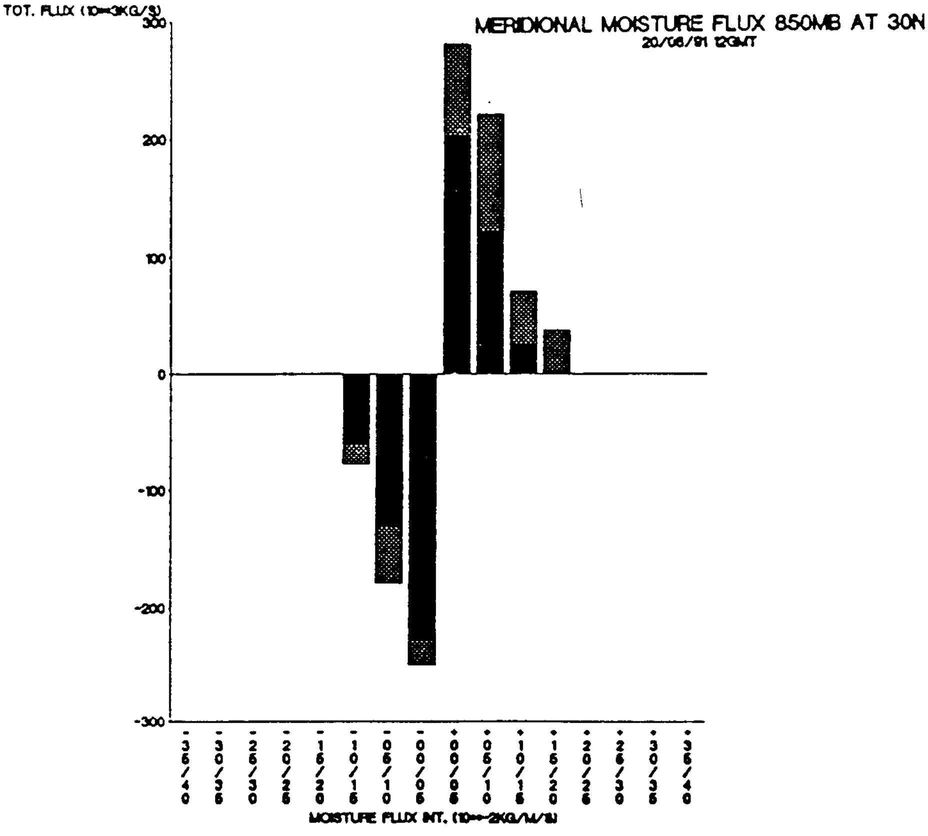

Figure 6.13 As figure 6.12 but for 30N.

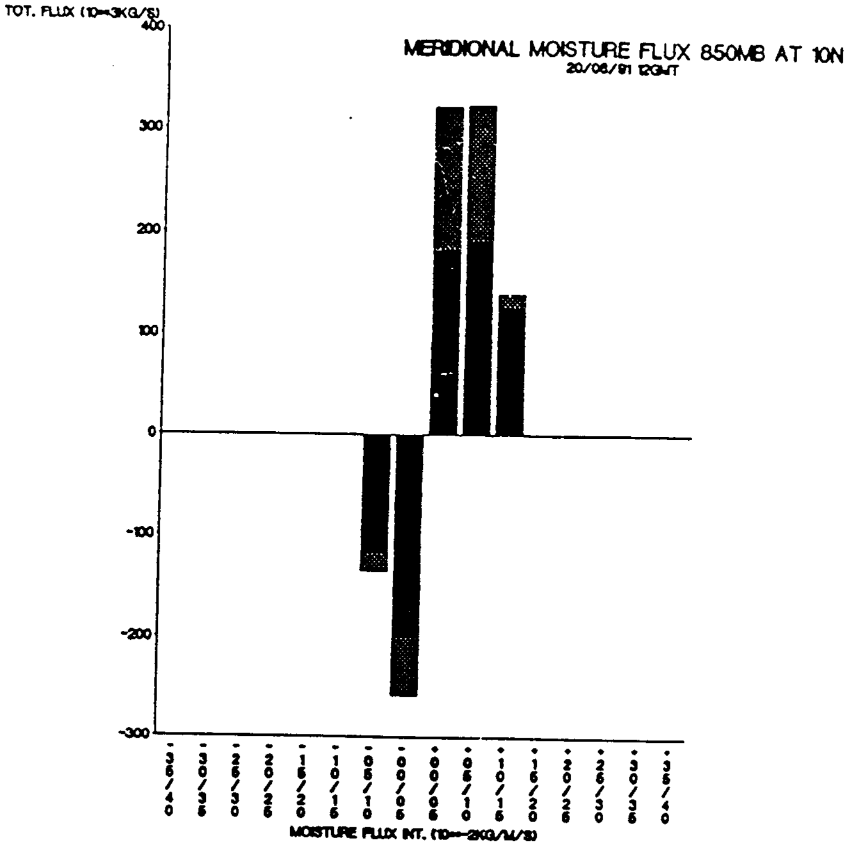

Figure 6.14 As figure 6.12 but for 10N.

	Poleward flux (Kgs^{-1})			Equatorward flux (Kgs^{-1})			Net flux (Poleward)	
latitude	total	clear sky	ratio	total	clear sky	ratio	total	clear sky
50N	389	148	0.38	330	267	0.81	+ 59	-119
30N	611	355	0.58	507	420	0.83	+104	- 65
10N	785	501	0.64	393	329	0.84	+392	+172

Table 6.1: Total and "clear sky" moisture flux at 850mb across latitudes 50, 30 and 10N. Note that the net poleward moisture flux under clear sky is considerably smaller than the total flux, and is of opposite sign at 50N and 30N, illustrating the difficulties of estimating global moisture transports from flux observations based on Doppler lidar winds.

6.4 Comments on the utility of a low power lidar instrument.

The use of low power lasers has been proposed as an option in lidar instrument design. Such instruments will only generate returns with a useful signal to noise ratio in regions where the backscatter coefficient is relatively strong; as in ice clouds (cirrus) typical of jet stream levels, and aerosol rich conditions typical of the planetary boundary layer (PBL). The instrument would therefore target the upper and lower tropospheric levels (with additional returns from water cloud at intermediate levels). Observations would not be possible in conditions of low aerosol concentration typical of cloud free regions of the middle troposphere.

In extratropical regions the wind field is dominated by the geostrophic wind component (i.e. that component of the wind field that is in geostrophic balance with the mass field). Indirect measurement of the geostrophic wind component may be obtained from information on the mass field supplied by atmospheric temperature sounders, and it follows that direct measurements of the wind field - provided by wind lidar - are likely to be most useful where departures of the wind field from geostrophic balance (the ageostrophic wind components) are most pronounced. Such departures are typically largest at jet levels and in the PBL, and on this basis it can be argued that a low power configuration would place the lidar observations at the levels where they are most needed. To investigate this line of reasoning, cross sections of ageostrophic wind speed have been obtained from the UK Met. Office Cyber model, and are discussed below.

The vertical structure of the ageostrophic wind component (at levels above the boundary layer) is illustrated in figures 6.15 and 6.16 which show, respectively, northern hemisphere, north-south cross sections of mean and rms ageostrophic wind speed. The cross sections were derived from model analyses for the first 10 days of January 1991. Both mean and rms values decrease with height from 800mb to a minimum at around 600mb, then increase to a maximum at the 250mb level. Reference to the mean total wind speed, reproduced in figure 6.17, shows that the 250mb level corresponds to the level of the jet stream. The ratio of ageostrophic wind speed to total wind speed gives that proportion of the wind speed that cannot be estimated from temperature sounding data, and the mean value of this ratio is reproduced in figure 6.18. The ratio shows very little vertical structure (in middle and high latitudes, below 100mb); at 50N, for example, the ratio is about 0.2 at both middle and jet levels and increases to about 0.3 at low levels.

To summarise, the contribution of the ageostrophic wind component to the total wind speed, when considered in proportion to that of the geostrophic component (which can be measured indirectly from temperature sounding data) is similar at all levels above the boundary layer in mid to high latitudes. It it is difficult, therefore, to justify selective targeting of the jet level on the basis of the vertical distribution of the ageostrophic wind. Because of the dynamical importance of the jet streams, selective targeting of the jet stream (as compared, say, to full vertical profiles at a lower resolution) may have some advantages - but this needs to be demonstrated by other means.

Further reference to figure 6.18 shows, as expected, that the ratio of the ageostrophic wind component to the total wind speed wind is much larger at low latitudes than at high latitudes (the ratio is about 1.0 near 10N between 700 and 600mb). The high degree of ageostrophy in these regions highlights the well established requirement for increasing the number of direct measurements of the wind field in tropical latitudes.

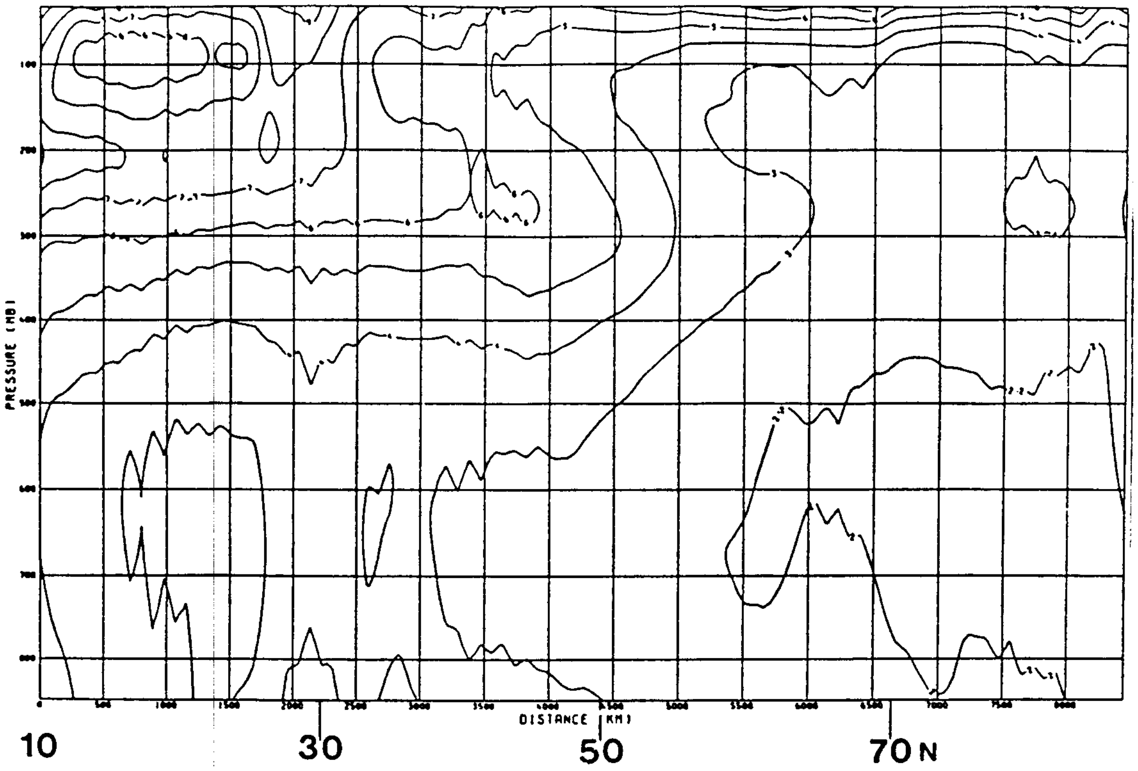

Figure 6.15 Vertical cross section (10N-86N) of mean ageostrophic wind speed for 1-10 January 1991 (from UK Cyber model fields). Units are ms^{-1}, contour interval = 1.

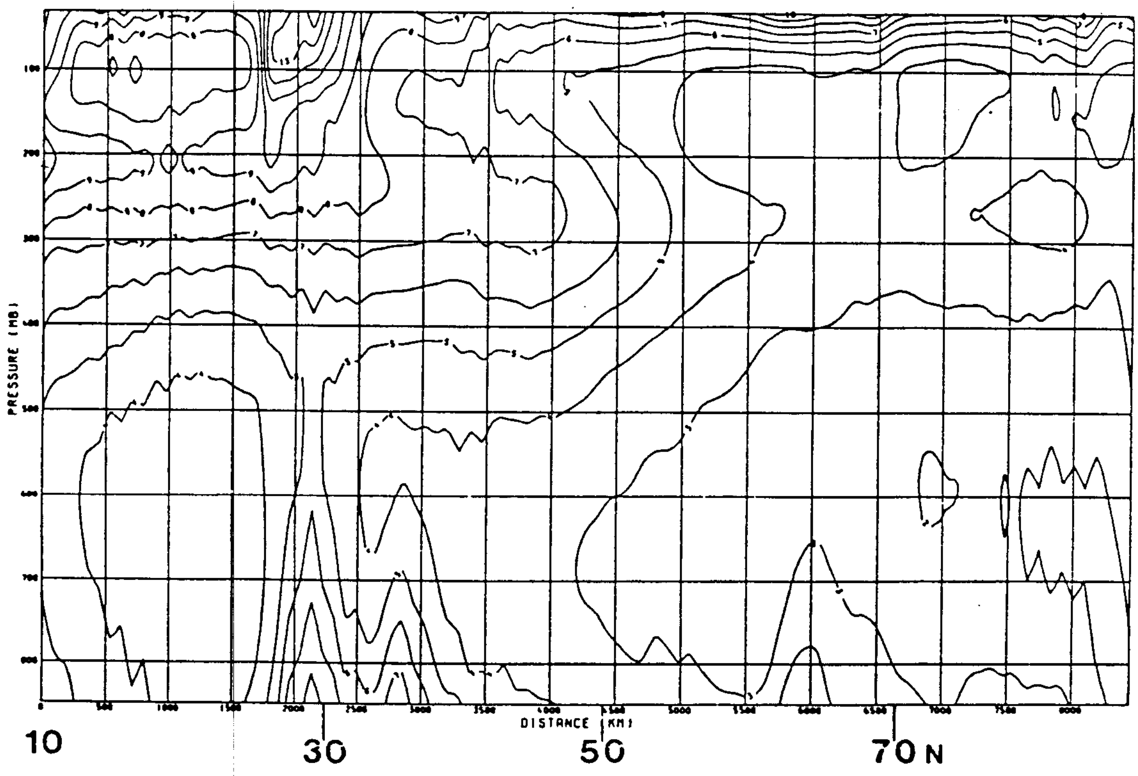

Figure 6.16 As figure 6.15 but for rms ageostrophic wind speed.

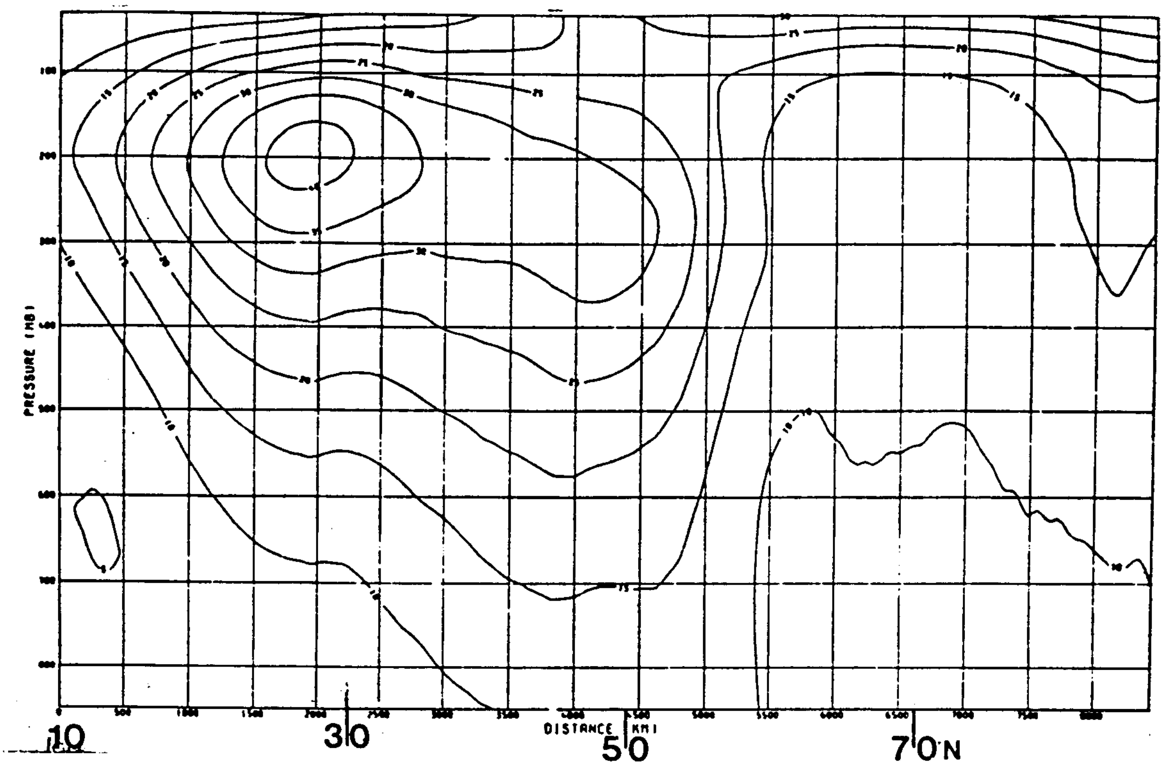

Figure 6.17 As figure 6.15 but for total wind speed.

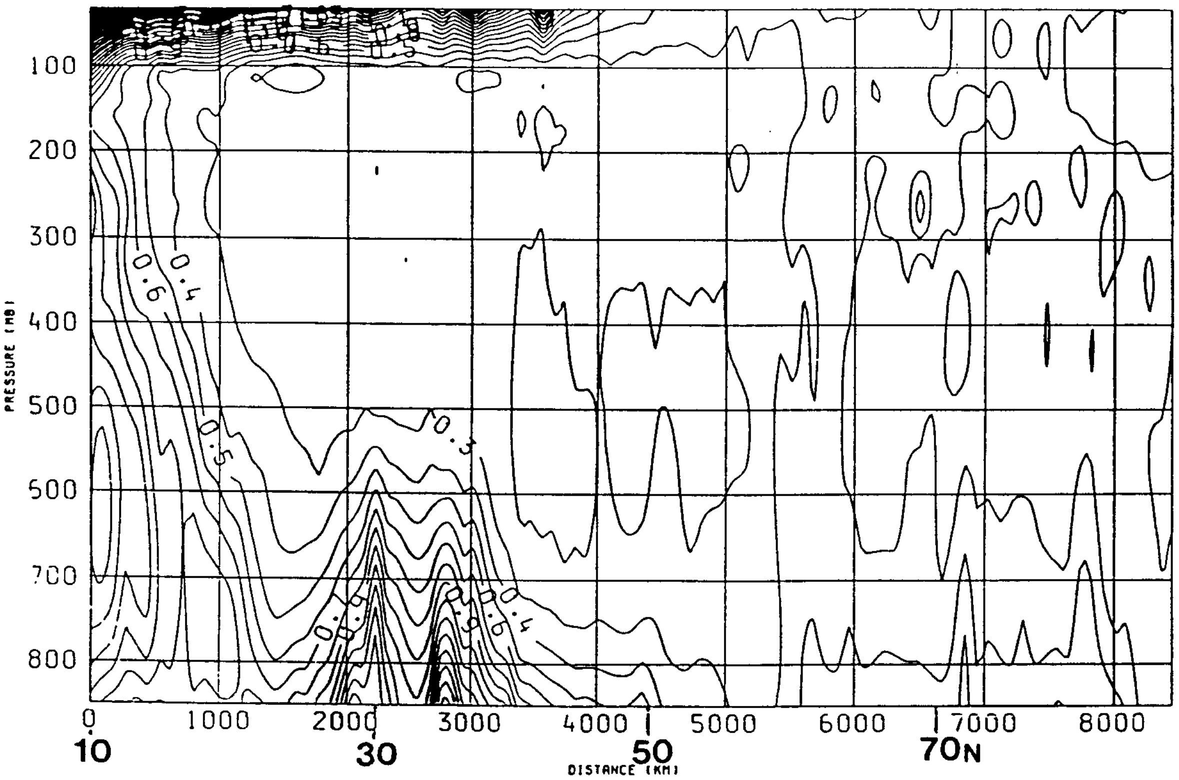

Figure 6.18 Mean ratio of ageostrophic wind speed and total wind speed (contour interval = 0.1).

6.5 Summary

The results of this section are summarised below.

- The results of three cases studies suggests that cloud obscuration may not seriously impair the potential of Döppler lidar wind data to improve NWP forecasts of cyclogenesis.
- Case studies of frontal structure suggest that, in mid-latitudes, regions of strong poleward moisture flux will be largely obscured from observation by extensive cloud cover.
- Estimates of global moisture transport based on lidar observations will be prone to underestimate the net poleward moisture flux, because the distribution of the data will be weighted away from regions of strong poleward moisture flux. This implies that best use of the data will come from its incorporation in an NWP data assimilation process. If model assimilated datasets are used there is little advantage, for the purpose of climate studies, in the BEST-type instrument configuration of simultaneous wind and moisture observations.
- Statistics for the ageostrophic wind speed obtained from the UK Cyber NWP model suggest that, in mid and high latitudes, the component of the wind that cannot be specified by temperature sounders (the ageostrophic part) is a similar proportion of the total wind speed at all levels. It is difficult, therefore, to justify selective targeting of the jet level on the basis of the ability of lidar observations to measure the ageostrophic component of the wind (in addition to the geostrophic component).

7 Summary and recommendations for an OSSE

In section 2 we have shown that single component winds can be used directly in practical assimilation systems; there is no advantage in aligning laser shots to obtain vectors.

As shown in section 3, care must be taken when combining data from Döppler processing of weak signals. Consensus averaging is a suitable practical method. With appropriate parameters it gives similar results to the more theoretically based maximum probability method. If prior information is incorporated into the process of combining the data, it can be very useful in avoiding gross errors.

In the circumstances of the simulation described in section 3, with the use of a background field from a good short-period forecast, a nonlinear analysis accounting for non-Gaussian errors is better than a (simpler) prior quality control step and a linear analysis.

Representativeness errors appropriate for the single-shot single component winds have been estimated in section 4. Combined with an instrument error assumed to be ~$1ms^{-1}$, they give "background" observation errors in the range 2-$3ms^{-1}$ (rms), a suggested vertical profile is given in table 4.4. Our studies suggest that the effects of orographic wave activity, clear air turbulence and convection will cause significant local increases in the rms observation errors above this background value: errors associated with orographic effects could be modelled with a Gaussian distribution, while those associated with convection probably follow a lognormal distribution.

In section 5 various different instrumental and scanning configurations were evaluated. It was shown that a conical scanning instrument is to be preferred to a fixed instrument with the shots concentrated in two strips. Our studies also suggest that with shot management across the swath, to give a constant spatial density, accuracy in the middle of the swath is improved, but extrapolation from the edge is less accurate.

Some aspects of the utility of Döppler lidar winds, in the light of the fact that observation will not be possible below clouds, have been addressed, in section 6. Our studies suggest that, in relation to NWP, the impact of Döppler lidar winds in improving forecasts of cyclogenesis - by improving initial conditions - may not be seriously reduced by the lack of observations beneath cloud.

In relation to utility for climate studies, it was shown that much of the poleward moisture flux occurs beneath extensive cloud cover, particularly in mid-latitudes. Consequently, the distribution of lidar winds will be weighted towards regions of weak or equatorward moisture flux, and estimates of global moisture transport, using flux measurements based on lidar winds, will be difficult. For climate studies, therefore, best use of the data is likely to come from its incorporation in a 4-D NWP data assimilation process. The need for an NWP assimilation implies that, for purposes of climate studies, there is less advantage in making simultaneous measurements of wind and moisture.

7.1 Recommendations for the simulation of Döppler lidar wind data

Our recommendations for the simulation of Döppler lidar wind data from the OSSE nature run are given below.

- Single component winds should be generated rather than vector winds.
- "Background" observation errors should be in the range 2-3ms^{-1} rms.
- Local effects that will increase the observation errors, i.e. orographic gravity waves, convection, and C.A.T. could also be simulated using the methods and error distributions suggested. However, some experimentation with the model used to generate the nature run would be necessary as a prior step.
- In regions of low backscatter, processing to allow for non-Gaussian errors will be necessary. High density observations with a high proportion of gross errors should be generated, for those wishing to investigate this. A lower density of simulated preprocessed data should be generated for other users. (The possibility of including some gross errors even in preprocessed data should be considered.)

References

Betout,P., Burridge,D. and Werner,Ch. 1989: ALADIN (Atmospheric Laser Doppler Instrument), ESA SP 1112, 1989.

Brewster, Keith A., and Schlatter, Thomas W. 1988: "Recent progress in automated quality control of wind profiler data". Preprints, 8th Conf. on NWP. Amer. Met. Soc.

Brown,P.R.A. 1983: "Aircraft measurements of mountain waves and their associated momentum flux over the British Isles" Quart.J.R.Met.Soc. **109**, 849-865.

Browning,K.A. 1986: "Conceptual models of precipitation systems" Weather and Forecasting **1** 23-41.

Courtier,P., Gauthier,P., Rabier,F., Flamant,P., Dabas,A., Lieutaud,F., and Renault,H. 1992: "Study of preparation for the use of Doppler wind lidar information in meteorological assimilation systems", Final report of ESA study contract 8850/90/HGE-I.

Dutton,M.J.O. 1980: "Probability forecasts of clear-air turbulence based on numerical model output" Meteor. Mag. **109** 293-310.

Eklund,W.L. Gage,K.S. Nastrom,G.D. and Balsley,B. 1986: "A preliminary climatology of the spectrum of vertical velocity observed by clear air doppler radar" J Clim & Appl Met. **25** 885-892.

Endlich,R.M., Singleton,R.C., and Kaufman,J.W. 1969: "Spectral analysis of detailed vertical wind speed profiles" J.A.S. **26** 1030-1041.

Golding,B.W. 1987: "The U.K. Meteorological Office mesoscale model" Boundary Layer Meteorology, **41** 97-107.

Golding,B.W. 1990: "The Meteorological Office mesoscale model" Meteor. Mag. **119** 81-96.

Graham,R.J. 1990: "The impact of north Atlantic TEMPSHIP observations on global model analyses and forecasts during a case of cyclogenesis" S division technical note No.46 UK. Met. Office.

Graham,R.J. 1991: "A case study of the impact of north Atlantic TEMPSHIP observations on a forecast of cyclogenesis" S division technical note No.60, U.K. Met. Office.

Hicks,B.B. 1985: "Behavior of Turbulence statistics in the convective boundary layer" J Clim and Appl Met. **24** 607-614.

Hollingsworth,A. 1986: "Objective analysis for Numerical Weather Prediction" In "Short- and medium- range Numerical Weather Prediction", papers presented at the WMO/IUGG NWP symposium, Tokyo, 1986, p11-59.

Izumi,Y. and Caughey,J.S. 1976: "Minnesota 1973 atmospheric boundary layer experiment data report" Air Force Cambridge Research Laboratory, Environ. Res. Papers 547, AFCRL-TR-0038, 28pp.

Kennedy,P.J and Shapiro, M.A. 1980: "Further encounters with Clear Air Turbulence in Research Aircraft" J.A.S. **37** 986-993.

Kitchen,M. 1989: "Representativeness errors for radiosonde observations" Quart. J Roy. Met. Soc. **115** 673-700.

LeMone,M.A. and Zipser,E.J. 1980: "Cumulonimbus vertical velocity events in GATE. Part I: Diameter, Intensity and Mass Flux" J.A.S., **37**, 2444-2457.

Zipser,E.J. and LeMone,M.A. 1980: "Cumulonimbus vertical velocity events in GATE. Part II: Synthesis and model core structure" J.A.S., **37**, 2458-2469.

Lilley,D.K. and Petersen,E.L. 1983: "Aircraft measurements of atmospheric kinetic energy spectra" Tellus **35A** 379-382.

Lopez,R.E. 1977: "The lognormal distribution and cumulus cloud populations" Mon. Wea. Rev. **93** 865-872.

Lorenc, A.C. 1981: "A global three-dimensional multivariate statistical analysis scheme." Mon. Wea. Rev. **109**, 701-721.

Lorenc, A.C. 1986: "Analysis methods for numerical weather prediction." Quart. J. Roy. Met. Soc. **112**, 1177-1194.

Lorenc,A.C. Bell,R.S. Davies,T. and Shutts,G.J. 1988: "Numerical forecast studies of the October 1987 storm over southern England" Meteor. Mag. **117** 118-130.

Lorenc, A.C. and Hammon, O., 1988: "Objective quality control of observations using Bayesian methods - Theory, and a practical implementation." Quart. J. Roy. Met. Soc. **114**, 515-543.

Lorenc, A.C. 1988: "Optimal nonlinear Objective Analysis." Quart. J. Roy. Met. Soc. **114**, 205-240.

Lorenc,A.C., Bell,R.S., and Macpherson,B. 1991: "The Meteorological Office *Analysis Correction* data assimilation scheme". Quart J Roy Met Soc **117** 59-89.

Mitchell, H.M., Charette, C., Chouinard, C., and Brasnett, B. 1990: "Revised interpolation statistics for the Canadian data assimilation procedure: their derivation and application" Mon. Wea. Rev. **118**, 1591-1597.

Nastrom,G.D. and Gage,K.S. 1985: "A climatology of atmospheric wavenumber spectra of wind and temperature observed by commercial aircraft" J.A.S., **42**, 950-960.

Nicholls,S. 1984: "The dynamics of stratocumulus: aircraft observations and comparisons with a mixed layer model" Quart.J.R.Met.Soc. **110** 783-820.

Purser, R.J. 1984: "A new approach to the optimal assimilation of meteorological data by iterative Bayesian analysis". Preprints, 10th conference on weather forecasting and analysis. Am Met Soc. 102-105.

Roach,W.T. 1967: "On the nature of summit areas of severe storms in Oklahoma" Quart. J. Roy Met Soc **93** 318-337.

Roll,H.V. 1965: "Physics of the marine atmosphere" Academic Press, 426pp.

Shutts,G.J. 1990:"Simulation of gravity wave activity over Wales" Mesoscale Newsletter No.2, U.K. Meteorological Office.

Strauch R., Merrit D., Moran K., Earnshaw K. and Van de Kamp D. 1984: "The Colorado Wind-Profiling Network". J. Atmos. Oceanic. Technol. **1**, 37-49.

Vaughan,J.M., Brown,D.W., Davies,P.H., Foord,R., Forrester,P., Nash,C., Bowdle,D.A. and Rothermel,J. 1988: "Assessment of global backscatter at 10μm, and future measurement programmes" Conference abstracts, 14th International Laser Radar Conference, June 1988.

Vaughan,J.M., Brown,D.W., Davies,P.H., Foord,R., Cannel,J. Nash,C., Woodfield,A.A., Bowdle,D.A. and Rothermel,J. 1987: "Atmospheric backscatter at 10.6μm; a compendium of measurements made outside the United Kingdom by the airborne LATAS coherent laser radar velocimeter" Royal Signals and Radar Establishment Report No.87002.

Vergeiner,I and Lilly, D.K. 1970: "The dynamic structure of lee wave flow as obtained from balloon and airplane observations" Mon.Wea.Rev, **98**, 220-232.

Warner,J. 1972: "The structure and intensity of turbulence in air over sea" Quart. J. Roy. Met. Soc., **98**, 175-186.

Warner,J. 1973: "Spectra of the temperature and humidity fluctuations in the marine boundary layer" Quart. J. Roy. Met. Soc., **99**, 82-88.